On the impact of new, light states in some astrophysical and laboratory systems

Or:

Looking for New Physics in the Lab, the Sky, and the Future

Giacomo Marocco

New College
University of Oxford

A thesis submitted for the degree of

Doctor of Philosophy

Trinity 2022

Abstract

We investigate the observational consequences of adding hypothetical new states to the Standard Model of particle physics. These additional fields are feebly coupled and much lighter than the electroweak scale. They include dark photons, millicharged particles, heavy neutral leptons, as well as light dark matter that couples to electronic spin, among others.

We derive limits on particles that could have been detected by the Big European Bubble Chamber (BEBC) in the 1982 CERN-WA-066 beam dump experiment. Light states coupling to photons, as well as heavy neutral leptons, may have been produced in the copious hadronic decays in the beam dump, and the lack of observed signal events allows us to place world-leading bounds on both these particles in the GeV mass range.

We also reappraise an existing astrophysical limit on ultra-light dark photons derived from Jupiter's magnetosphere. The new bosons may kinematically mix with our photon, leading to modifications of electrodynamics at large distances. Observations of the magnetic field around Jupiter allow us to place the strongest constraints to date on the size of the mixing, once we include measurements of the plasma from the recent Juno spacecraft mission.

Lastly, we study the ability of sub-GeV dark matter coupling electronic spin to excite magnons in magnetically ordered materials. We calculate the expected excitation rate in quasi-2d ferromagnetic materials, and show it exhibits strong anisotropies. These materials then allow for directional detection of such dark matter candidates. The near-term possibility of detecting these small meV energy depositions raises the exciting prospect that this may be a compelling way to discover the particle nature of dark matter.

Acknowledgements

Firstly, I am immensely grateful to my advisors Subir Sarkar and John Wheater. If I now feel anything like a physicist, it is because of them and their guidance.

I am specifically grateful to Subir for being my teacher, and for having his door open to me and my numerous questions and confusions throughout the years, and for the inspiring conversations that would always ensue. I will treasure the knowledge he has given me.

There were numerous times when I was considering leaving this degree, and it is thanks to John's advice and help that I am finishing today. I also thank him for his example as a physicist, which has shown me a path which I will always try to follow.

Thank you as well to all the staff in Theoretical Physics for your tireless work. In particular, I thank Michelle Jose for welcoming me so warmly to the department, for her support throughout my PhD, and for inviting me to cake club even though I eat neither eggs nor butter. Thank you to Russell Jones as well for bailing me out of computer trouble numerous times.

I thank Filippo Revello, for giving me a wonderful reason to come into the office. Thank you Prateek Agrawal for all the professional wisdom you have given me, to Arthur Platschorre for letting me pretend to be a formal physicist, and to all the other students from whom I have learned so much.

Lastly, thank you to Cressida Collins for keeping me afloat over the past years, and for making this time so special.

Statement of Originality

This thesis is the work of the author except where stated. No part of this thesis has been submitted for any other qualification.

Chapter 2 is based on collaborative work published in [1], as detailed at the end of the respective chapter. The Monte Carlo simulations used in Chapter 3 were written by Mr Ryan Barouki, with the overall project guided by Prof. Subir Sarkar. Prof. John Wheater and I worked on Chapter 5 together.

Contents

Chapter 1

Introduction

The Standard Model (SM) is the well-established basis of particle physics, with experimental results almost universally matching the theoretical predictions. Why, then, do we particle phenomenologists spend our lives looking for new states Beyond the Standard Model (BSM)?

Though there are many motivations, my work has been motivated by the following subset: (i) the Strong CP problem; (ii) the probable existence of dark matter (DM); and (iii) the need for a complete theory of gravity and quantum field theory. Explaining any one of these problems likely necessitates the existence of BSM particles. Moreover, it is important to stress that it is because of the fabulous success of the SM and the principles of QFT that one must take each of these puzzles seriously – we should take the theory as seriously as we can, and treat all its shortcomings with care.

In the rest of this chapter, I will discuss each of these problems in turn, and demonstrate how resolving them introduces new states into the theory. We will also see that although the dynamics of these solutions originates at high energies, not all the new states need lie at inaccessibly small scales. In fact, light states (loosely defined here as lighter than the proton, say) may naturally arise as solutions to these three puzzles.

1.1 The Standard Model in 60 seconds 

We begin by recalling the Standard Model, so that we can set notation and also point out its flaws along the way. The SM gauge group G_{SM} is $SU(3)_C \times SU(2)_L \times U(1)_Y$. Its gauge bosons, which sit in the adjoint representation, mediate forces between the scalars and fermions, listed in table 1.1 along with their charges; all the fermions come in three generations. The most general renormalisable, Poincaré$\times G_{SM}$-invariant Lagrangian we can write down is

$$\begin{aligned}\mathcal{L} = &-\frac{1}{4}B_{\mu\nu}B^{\mu\nu} - \frac{1}{4}\mathrm{Tr}\, W_{\mu\nu}W^{\mu\nu} - \frac{1}{4}\mathrm{Tr}\, G_{\mu\nu}G^{\mu\nu} + \theta\frac{\alpha_S}{8\pi}\mathrm{Tr}\, G_{\mu\nu}\tilde{G}^{\mu\nu} \\ &+ \bar{L}_i i\not{D} L_i + \bar{e}_{iR} i\not{D} e_{iR} + \bar{Q}_i i\not{D} Q_i + \bar{d}_{iR} i\not{D} d_{iR} + \bar{u}_{iR} i\not{D} u_{iR} \\ &+ |D_\mu H|^2 + m^2|H|^2 - \lambda|H|^4 \\ &- Y^d_{ij}\bar{Q}^i H d^j_R - Y^u_{ij}\bar{Q}^i \tilde{H} u^j_R - Y^\ell_{ij}\bar{L}_i H e_R + \text{h.c.} \\ &+ \frac{1}{16\pi G_N}\left(R - 2\Lambda\right).\end{aligned} \tag{1.1.1}$$

Let's go through this a line at a time:

1. The first line contains the kinetic terms for the $U(1)_Y$ boson B, the $SU(2)_L$ bosons W, and the $SU(3)_C$ bosons G, and trace Tr denoting a contraction of gauge indices. The term with the dual field strength $\tilde{G}^{\mu\nu} = \epsilon_{\mu\nu\alpha\beta}G^{\alpha\beta}$ is the "theta term" which, as a total derivative, encodes the non-trivial topology of maps from spacetime to the gauge group $\pi_3(SU(3)) = \mathbb{Z}$. Experimentally, θ is almost aligned with the phase of the Yukawa matrices (see 4th line), as we shall discuss in more detail, which is puzzling in the SM – this is a first glimpse of the Stong CP problem. We have not written down a similar term for $SU(2)_L$ since it can be rotated away by the anomalous $U(1)_{B+L}$ symmetry (assuming this is a good symmetry of the SM's UV completion), nor for $U(1)_Y$ because $\pi_3(S^1) = 0$ (assuming the absence of magnetic monopoles, which would feel the Witten effect [2]).

2. Next are the fermion's kinetic terms, which have been diagonalised in flavour space, indexed by i, j. D_μ is the covariant derivative.

3. This describes the Higgs, which has a non-zero minimum due to the shape of its quartic potential. In that vacuum, symmetry breaking occurs: $SU(2)_L \times U(1)_Y \to U(1)_{EM}$. Stabilising m at the electroweak scale against radiative corrections from heavy new physics is generically difficult – this is the electroweak hierarchy problem.

4. The Higgs-fermion couplings follow, with the Higgs' dual $\tilde{H} = i\sigma^2 H^*$ allowing both up- and down-type quark masses, although not neutrino masses. The observation of massive neutrinos implies there must exist at least an additional SM-singlet or higher-order operators. The question of the exact dynamics is another mystery. The quark and leptons masses are parametrised by the Yukawa matrices, which are generic complex 3×3 matrices, and so may only be diagonalised by singular value decomposition, at the cost of introducing flavour mixing in the electroweak currents. After electroweak symmetry breaking, the Yukawas generate masses for the fermions. The true origin of the large hierarchies in the values of these matrices is unknown, although there are many proposals, e.g. Froggatt-Nielsen models, [3], and large [4, 5] or warped [6, 7] extra dimensions..

5. We include Einstein gravity with the addition of the Ricci scalar R (and Newton's constant G_N), although it is not strictly part of the Standard Model. This term is non-renormalisable, and breaks perturbative unitarity at the Planck scale, indicating the need for a UV completion. Further, the small size of Λ with respect to the Plank mass is hard to explain. Astrophysical and cosmological observations motivate some to modify Einstein gravity, others add dark matter.

Field	$L = \begin{pmatrix} \nu_L \\ e_L \end{pmatrix}$	e_R	$Q = \begin{pmatrix} u_L \\ d_L \end{pmatrix}$	u_R	d_R	H
Charge	$(1,2)_{-1/2}$	$(1,1)_{-1}$	$(3,2)_{1/6}$	$(3,1)_{2/3}$	$(3,1)_{-1/3}$	$(1,2)_{1/2}$

Table 1.1: The matter content of the Standard Model. For the charge, the first entry denotes the $SU(3)_C$ representation, then $SU(2)_L$, while the subscript indicates $U(1)_Y$ hypercharge. The electric charge is $Q = T_3 + Y$, where T_3 is the diagonal $SU(2)_L$ generator.

1.2 Effective field theory and renormalisable portals

We have now seen six puzzles of the SM. To better understand them, as well as some of their possible solutions, we introduce the logic of an effective field theory (EFT). EFT provides a useful tool for organising the effects of any new physics on the SM field content. The basic observation is that although a Lagrangian may in principle involve an infinite sum of interactions among the degrees of freedom of the theory, one in fact only needs to deal with a finite subset of these when working in the deep infrared (at least in the perturbative regime of the theory). This will explain why we only wrote down the renormalisable terms in the SM Lagrangian.

Concretely, when working in $D = 4$ spacetime dimensions, only those operators of (engineering) dimension 3 or less are relevant, those of dimension 4 are said to be marginal, while the rest are irrelevant. As a motivational illustration for this, let's consider the following example of a scalar field theory in Euclidean space

$$S_E = \int d^4x \left(\frac{1}{2}\partial\phi \cdot \partial\phi + \frac{1}{2}m^2\phi^2 + \lambda\phi^4 + g\phi^6 \right). \tag{1.2.1}$$

Consider now a rescaling of the length scale $x \to \lambda x$, so that the volume element is rescaled by λ^4, while on dimensional grounds a dimension d operator is rescaled by λ^{-d}. Then the total contribution of this particular operator will be rescaled by a power of $4 - d$. At very long scales, we thus see that the relevant operators (the first two of Eq. (1.2.1)) will dominate the action, while the effect of the irrelevant

one (the last term) approaches zero. For marginal operators (the quartic), one must carry out a more sophisticated quantum analysis in order to make a statement[1]. This explains why we include only quartic interactions of the Higgs for instance, and not higher order interactions, when we write down the SM Lagrangian.

Let us assume that there is some high energy scale at which resides some new physics. When working at human energies much below this scale, one may use the logic of effective field theory to organise the BSM physics. It is a fact that at dimension four, there are only three types of invariant operators, or portals, which couple the new states to the SM. These portals to new physics are

$$\begin{aligned} \text{Kinetic mixing} &: \epsilon F_{\mu\nu} X^{\mu\nu} \\ \text{Neutrino portal} &: U^{i}_{\ 4}\, \bar{L}_i \tilde{H} N \\ \text{Higgs portal} &: |H|^2 \chi^2 \end{aligned} \tag{1.2.2}$$

Here, F and X are the field strengths associated with the photon and some new vector boson, respectively; N is some new SM singlet fermion, and χ is a scalar singlet. In this thesis, I will study the kinetic mixing portal in two guises: first directly, as a modification of electrodynamics, and a second time indirectly, when it may give rise to dark states with a small, non-quantised electric charge. We will also look at the neutrino portal, and see how bounds on such singlets, called heavy neutral leptons, may be obtained.

Having shown the distinction between a relevant and irrelevant operators, it is important to stress that irrelevant operators can still have important effects. In practice, we never work in the far infrared, and so at finite energies irrelevant operators may still have a finite, measurable effect[2]. We will look at the effect

[1] In fact, one must do this careful analysis for all operators when working with a strongly coupled theory: there is no guarantee in such theories that the anomalous dimension is small, and so the engineering dimension of an operator tells us nothing on its own.

[2] Indeed, they may even give the dominant contribution to a particular process if it violates some symmetry that is accidentally satisfied by all lower dimension operators. Some nice examples are proton decay, or the universality of tri-boson couplings in the SM.

of some these operators both at accelerator beam dump experiments, and in dark matter direct detection experiments.

1.3 Is Nature Natural?

In the previous section, we talked about the operators appearing in an action, but were silent about the other objects appearing in the action: the coupling constants. We may write all the coupling constants in terms of some power of the cut-off scale, multiplied by a dimensionless number. This dimensionless quantity is referred to as a "Wilson coefficient". It is these Wilson coefficients that, together with their corresponding operators, determine the dynamics of a theory. A natural question to ask is: what numerical value should these coefficients be?

A reasonable expectation for the size of these Wilson coefficients is that they are generically $\mathcal{O}(1)$, rather than extremely small. Why is this? Suppose in the ultraviolet where the theory is defined, the coefficients are not $\mathcal{O}(1)$, but in fact very small. As we flow to lower energies, the Wilson coefficient g evolves according to the renormalisation group (RG) equation, which can be written perturbatively as

$$\beta(g) \equiv \frac{\mathrm{d}g}{\mathrm{d}\log\mu} = c_0 + c_1 g + \dots \tag{1.3.1}$$

where μ is the scale of measurement, and the c_i are constants. Now if c_0 is some generic constant, we expect the coupling to evolve such that it does not stay small in the infrared.

An exception to the above evolution of g away from its initial value is if there is an additional symmetry of the theory in the limit $g \to 0$. If this is the case, the zeroth-order term c_0 must vanish, or else the symmetry would not be preserved under RG flow in the exactly symmetric limit. This is the so-called 't Hooft (technical) naturalness criterion [8]. It is to be contrasted with the original notion of naturalness, proposed by Dirac [9], who precludes any small (or large) numbers

from a fundamental theory. We shall see later that there are a number of parameters in the SM that fail to meet both naturalness criteria. Such fine-tunings suggest a deeper explanation. The alternative is to claim that we live in a special point in the parameter space of the UV completion of the SM, which might be unsatisfying.

1.4 Strong CP problem and axions

The experimental observation that the size of the neutron's electric dipole moment (EDM) d_n is consistent with zero [10]

$$d_n = (0.0 \pm 1.1 \pm 0.2) \times 10^{-26}\,\mathrm{e\,cm} \tag{1.4.1}$$

indicates that the strong interactions governing the neutron are approximately symmetric under both parity- and time-reversal. What is the expected size of the neutron's EDM? Let us look at the Lagrangian of quantum chromodyanmics (QCD) after electroweak symmetry breaking:

$$\mathcal{L}_{\mathrm{SM}} \supset \bar{q}(i\not{D} - m_q)q - \frac{1}{4}\mathrm{Tr}\, G_{\mu\nu}G^{\mu\nu} + \theta\frac{\alpha_S}{8\pi}\mathrm{Tr}\, G_{\mu\nu}\tilde{G}^{\mu\nu}, \tag{1.4.2}$$

where q are the light quarks, m_q is the (complex) mass matrix arising from the Yukawa matrices. Under a chiral change of basis,

$$U(1)_A : \; q \to e^{i\alpha\gamma^5}q,$$

the theta term shifts as well

$$\theta \to \theta - \alpha$$

due to the chiral anomaly. The invariant combination is

$$\bar{\theta} = -\arg \mathrm{e}^{-\mathrm{i}\theta}\det m_q. \tag{1.4.3}$$

The theta term may readily be seen to be P- (and T-)odd, since the four dimensional Levi-Cevita symbol vanishes unless there are odd number of space (time) indices. Hence, $\bar{\theta}$ must almost vanish for QCD to respect the observed symmetries. Quantitatively, we have [11, 12]

$$d_n = 2.4 \times 10^{-16} \bar{\theta}\, \mathrm{e\,cm}, \tag{1.4.4}$$

and so

$$\bar{\theta} < 2 \times 10^{-11}.$$

Given that the phase in the quark mass matrix is a property of the Yukawa matrices, while θ is a property of the QCD vacuum, the fact that this combination of unrelated constants is almost exactly zero is a puzzle beyond the SM. Sending $\bar{\theta}$ to zero does not enhance a symmetry of the SM: P and T are maximally violated in the electroweak sector, by the $V - A$ coupling and the CKM matrix, respectively.

The simplest solution to the vanishing of $\bar{\theta}$ is that one of the quarks is massless [13], in which case an axial rotation $U(1)_A$ of this quark always allows $\bar{\theta}$ to be rotated away. Unfortunately, comparison of lattice simulations with experimental results from meson spectroscopy indicate that all the quarks are massive [14]. The next simplest idea is that the such an axial symmetry exists in the UV, but is spontaneously broken at the electroweak scale [15, 16]; we will call any such symmetry which allows θ to be rotated away a Peccei-Quinn (PQ) symmetry $U(1)_{\mathrm{PQ}}$. This, too, is experimentally ruled out, as the associated Nambu-Goldstone boson (the *axion*) [17, 18] would have been seen by now. However, one may break this PQ symmetry at some very high scale f_a, in order to evade experimental bounds. The canonical implementations of such an "invisible" axion are the DFSZ [19, 20] and KSVZ [21, 22] axions, and these provide useful benchmarks of the expected size of axion-SM couplings.

Whatever the exact UV implementation, at low energies one effectively adds a

dynamical field a to the $\bar{\theta}$ parameter in the Lagrangian:

$$\mathcal{L} \supset \frac{a}{f_a}\frac{\alpha_s}{8\pi}\mathrm{Tr}\, G_{\mu\nu}\tilde{G}^{\mu\nu} \tag{1.4.5}$$

When QCD confines, it explicitly breaks the PQ symmetry, inducing a small axion mass. This may be seen through the effective potential

$$V = -(m_\pi f_\pi)^2\sqrt{1 - \frac{4m_u m_d}{(m_u+m_d)^2}\sin^2\left(\bar{\theta}+a\right)/2}, \tag{1.4.6}$$

where m_π is the pion mass, f_π the pion decay constant, and $m_{u,d}$ are the light quark masses. Note that this is minimised at $\bar{\theta}+a=0$, which is the CP-conserving phase. The axion remains naturally light even against radiative corrections due to its approximate shift symmetry.

1.4.1 String theory and axions

Another class of axions may arise from the low-energy excitations of string theory [23, 24]. These axions[3] have less constrained properties than the QCD axion, since they need not solve the Strong CP problem. These arrive from the various p-forms that occur in the 10d string theory. For instance, in type II string theory, there is always a Kalb-Ramond 2-form, although there may also be others. The massless modes may be expanded in a harmonic basis of p-forms ω^i

$$B^{(p)} = \frac{1}{2\pi}\sum_i b^i(x)\omega^i(y), \tag{1.4.7}$$

[3]More precisely, these are axion-like particles (ALPs). We refer to these as axions as well, and specify an axion with coupling $G\tilde{G}$ as the QCD axion.

where x are the co-ordinates of our putative 4d spacetime, while y are the compact co-ordinates. Then we may wrap this p-form around the dual p-cycle C^m

$$\int_{C^j} B^{(p)} = b^j(x), \tag{1.4.8}$$

which will play the role of our 0-form pseudoscalar with a shift symmetry, i.e. an axion-like particle.

These ALPs are massless, but will receive instanton corrections which break the shift symmetry. The expectation is that this effect litters axions throughout the mass range, and leads to the picture of the string axiverse. One must fine-tune this somewhat, as the axion comes in the same multiplet as the geometric modulus, and this must be stabilised at some high mass scale in order to make the extra dimensions unobservable. The naive expectation is then that the axion would also sit at this mass scale. However, doing the tuning once to get a light QCD axion and solve the strong CP problem generically tunes the other ALPs to a light mass. Such ALPs are predictions of a string theory that solves the strong CP problem, and are of phenomenological interest [25].

Some of my work has focused on searching for such axions, e.g. [26, 27], but I will not discuss this any further in this thesis.

1.5 Dark photons and millicharged particles

There may exist a light vector boson of mass m, called a dark photon X_μ, that kinetically mixes with our photon A_μ [28]. This mixing may arise, for instance, by integrating out a loop of heavy fermions that are charged under both our photon and this dark photon, leaving behind a renormalisable interaction at low energies. The defining Lagrangian is then written as

$$\begin{aligned}\mathcal{L} \supset & -\frac{1}{4}\left(F_{\mu\nu}F^{\mu\nu} + F'_{\mu\nu}F'^{\mu\nu}\right) + \frac{\sin\alpha}{2}F^{\mu\nu}F'_{\mu\nu} + \frac{1}{2}m^2X^\mu X_\mu \\ & + eJ^\mu_{\mathrm{EM}}A_\mu + e'J^\mu_\chi X_\mu\end{aligned} \tag{1.5.1}$$

where $\sin\alpha$ parametrises the mixing between the standard kinetic terms $F'_{\mu\nu}$ and $F_{\mu\nu}$, and J_χ is a dark current that couple to X with strength e'. To get to a basis with diagonal kinetic terms, we let $A_\mu \to \frac{A_\mu}{\cos\alpha}$ and $X_\mu \to X_\mu + \sin\alpha A_\mu$, so that the Lagrangian reads

$$\begin{aligned}\mathcal{L} \supset & -\frac{1}{4}\left(F_{\mu\nu}F^{\mu\nu} + X_{\mu\nu}X^{\mu\nu}\right) + \frac{m^2}{2}\left(X^\mu X_\mu + 2\chi X^\mu A_\mu + \chi^2 A^\mu A_\mu\right), \\ & + \frac{e}{\cos\alpha}J^\mu_{\mathrm{EM}}A_\mu + e'J^\mu_\chi(X_\mu + \sin\alpha A_\mu)\end{aligned} \tag{1.5.2}$$

where $\chi \equiv \tan\alpha$ and $\tilde{m} \equiv m\cos\alpha$.

Since the mixing is small, this Lagrangian is usually expanded as a perturbation series in χ, and one works in terms of

$$\mathcal{L} \supset -\frac{1}{4}\left(F_{\mu\nu}F^{\mu\nu} + X_{\mu\nu}X^{\mu\nu}\right) + eJ^\mu_{\mathrm{EM}}A_\mu + \frac{m^2}{2}\left(X^\mu X_\mu + 2\chi X^\mu A_\mu\right) + \mathcal{O}(\chi^2). \tag{1.5.3}$$

In this (A_μ, X_μ) basis, the mass matrix may be written as

$$M^2 = \tilde{m}^2\begin{pmatrix}0 & \chi \\ \chi & 1\end{pmatrix} + \mathcal{O}(\chi^2), \tag{1.5.4}$$

which is diagonalised by the rotation

$$\begin{pmatrix}A_\mu \\ X_\mu\end{pmatrix} \to \begin{pmatrix}1 & \chi \\ -\chi & 1\end{pmatrix}\begin{pmatrix}A'_\mu \\ X'_\mu\end{pmatrix}; \tag{1.5.5}$$

in terms of A'_μ and X'_μ, the Lagrangian is

$$\mathcal{L} \supset -\frac{1}{4}\left(F'_{\mu\nu}F'^{\mu\nu} + X'_{\mu\nu}X'^{\mu\nu}\right) + eJ^\mu_{\rm EM}A'_\mu + e\chi J^\mu_{\rm EM}X'^\mu + \frac{1}{2}m^2X'^\mu X'_\mu + \mathcal{O}(\chi^2). \quad (1.5.6)$$

Note that the usual electromagnetic current $J^\mu_{\rm EM}$ now couples also to the dark photon in this purely diagonal basis. If we calculate the potential between two charges, to this order in the mixing parameter we find

$$V(r) = \frac{\alpha}{r}(1 + \chi^2 e^{-mr}), \quad (1.5.7)$$

which is the sum of the contribution from the massless photon and the massive photon, with the latter weighted by an additional χ^2 factor. We will investigate further ramifications of this in Chapter 4.

1.5.1 String theory and dark photons

The complex geometry in string theory can also lead to many additional photons. These generically mix with our photon. However, in order to have an observable signal, they must also have a non-zero mass, or else they just effect a renormalisation of the fine-structure constant. So, one must give these photons a small mass, but once this is done, another possible expectation of string theory is a "string photiverse", lending further motivation to their search.

1.6 Neutrinos and their mass

On 4 December 1930, Pauli suggested that the energy conservation in beta decay implied the existence of an electrically neutral particle, which we now call the electron neutrino ν_e. At the time, Pauli himself considered the proposition of an apparently undetectable particle to be a "desperate remedy", but, as he said: "only the one

who dare (sic) can win".

Decades later, this bold prediction was confirmed by a measurement of inverse beta decay at Los Alamos [29]. We now know from precision measurements of the Z-boson width at LEP that there are $2.9840 \pm 0.0082 \simeq 3$ neutrinos charged under G_{SM} below $m_Z/2$ [30]. Furthermore, Pontecorvo predicted that if there are multiple neutrinos with non-zero mass splitting, then they will oscillate into each other, violating the accidental lepton flavour symmetry of the SM [31]. Subsequent measurements of atmospheric and solar neutrinos provided experimental evidence for this hypothesis, which has now also been measured in long-baseline neutrino beam experiments.

1.6.1 Some implications

The non-zero neutrino mass matrix introduces flavour mixing during oscillations. Diagonalising the neutrino mass matrix by a unitary transformation affects the electroweak interactions, in an analogous way to the CKM matrix. The particular interaction eigenstate $|\nu_\alpha\rangle$ produced in some reaction will then be a linear combination of these mass eigenstates $|\nu_i\rangle$:

$$|\nu_\alpha\rangle = \sum_i U^i{}_\alpha \, |\nu_i\rangle. \tag{1.6.1}$$

It is these mass eigenstates that are the propagating degrees of freedom, which will then constitute some other linear combination of interaction eigenstates upon a subsequent interaction (where, for instance, they are detected).

As mentioned at the start of the chapter, such neutrino masses are evidence of BSM physics. The SM Lagrangian has an accidental yet exact $U(1)_{B-L}$ global symmetry, forbidding the generation of a neutrino mass. Any BSM physics that does not respect this symmetry is expected to generate neutrino masses after being integrated out. Already at dimension five, one can write down the Weinberg operator

[32]

$$-\frac{c_{ij}}{\Lambda}(\bar{L}^i\tilde{H})\,(\tilde{H}L^j)^\dagger, \tag{1.6.2}$$

which generates neutrino masses after symmetry breaking. Such a term built only from left-handed SM neutrinos ν_L is called a Majorana mass:

$$-\,c_{ij}\frac{v^2}{\Lambda}\bar{\nu}_L^i\,\nu_L^{c,j}. \tag{1.6.3}$$

Assuming $\mathcal{O}(1)$ Wilson coefficients, we infer a new physics scale of

$$\Lambda \sim \frac{v^2}{m_\nu} \sim 10^{13}\,\text{GeV}\left(\frac{1\,\text{eV}}{m_\nu}\right), \tag{1.6.4}$$

which is unfortunately too high to be directly observable.

Another option is to augment the SM with at least two right-handed SM-singlet neutrinos N^i (although there need not be multiple new singlets). This allows a Dirac mass term to be written down

$$Y_{ij}\bar{L}^i\tilde{H}N_j, \tag{1.6.5}$$

which can, if N carries a conserved lepton number, still respect the accidental $U(1)_L$ of the SM. If these new leptons N are light enough, one can hope to detect them directly. This is the focus of Chapter 3.

1.7 Dark matter and direct detection

Observations from across a range of cosmological and astrophysical scales indicate that the dominant component of the matter density of the Universe is in the form of non-baryonic matter. Some candidates for this matter may themselves be light, such as the axion, motivating us to look for such fields. Given the amount of work being done looking for particular models of this dark matter, it is worth reviewing

the relevant facts.

1.7.1 "Just modify gravity!"

Firstly, is it possible that the conclusion of invisible gravitating matter is simply due to an incorrect description of the gravitational force. Such proposals, such as modified Newtonian gravity [33], or MOND, are well-motivated on galactic scales. For instance, MOND predicts the Tully-Fisher relation [34], an observed tight correlation between the luminosity and rotation velocity of spiral galaxies, as well as a wide variety of galactic rotation curves. However, on larger scales, MOND faces experimental and theoretical difficulties, which we enumerate here.

In order to describe the cosmological evolution of the Universe, one needs a relativistic theory of modified gravity. In most of these models, such as TeVeS [35], fits to the CMB power spectrum, as well as to the matter power spectrum of large scale structure, obtain poor results in comparison to those with DM. An exception has recently been put forward [36], although this contains an unpalatable wrong-sign kinetic term. These models must also contend with the fact that no precision test of General Relativity on sub-solar systems scales has found a disagreement. A robust observation of a non-gravitational DM interaction, which is currently lacking, is needed to conclusively lay this issue to rest.

1.7.2 Evidence for dark matter

Here, we briefly recall some of the evidence for the existence of dark matter. For a more thorough review, see e.g. [37].

One of the first major pieces of evidence was the lack of the expected fall off in galactic rotation velocity as the radius increases [38, 39]. Comparing the rotation velocities to that expected from the mass distribution inferred from the luminous galactic matter, one is lead to postulate a change in the mass-luminosity ratio. A

simple explanation of this is dark, non-baryonic matter.

Furthermore, the peaks in the CMB require matter that is decoupled from the photon-baryon fluid [40]. Additionally, there is much more structure on large scales than one would expect without dark matter. The growth of baryonic matter perturbations under gravitational collapse only begins once they decouple from the photon bath around recombination. Hence, in order to reconcile the observed fluctuations in the CMB with large scale structure, we are lead to introduce some matter which may begin clumping at earlier redshifts, and so cannot couple strongly to photons.

Lastly, we can consider merging clusters, e.g. the 'Bullet cluster' [41]. In these systems, we observe the bright X-rays emitted by the luminous gas of the galaxies smashing together. The gas clouds interact with each other, feel a drag force, and slow down. We also observe the position of the mass of the galaxy through gravitational lensing. Observations imply that the gas and the matter are well-separated, suggesting that most of the matter in these galaxies cannot interact too strongly, or it would do as the gas does and be slowed. We thus indirectly infer the existence of some non-luminous matter, with a self-interaction cross-section per unit mass bounded by $\sigma \lesssim 1\,\mathrm{cm}^2\,\mathrm{g}^{-1}$ – this is about the hadronic cross-section, and so actually allows for significant self-interaction.

1.7.3 Dark matter velocity distribution

As we will see, the detectability of a DM signal depends strongly on its velocity distribution. What is our expectation for the DM phase space distribution $f(\mathbf{x}, \mathbf{v}, t)$? Answering this question requires us to solve Boltzmann's transport equation

$$\frac{\partial f}{\partial t} + \dot{\mathbf{x}} \cdot \frac{\partial f}{\partial \mathbf{x}} + \dot{\mathbf{v}} \cdot \frac{\partial f}{\partial \mathbf{v}} = C[f], \tag{1.7.1}$$

where a dot indicates partial differentiation with respect to t, and $C[f]$ is the collisional term. The standard ΛCDM paradigm stipulates only cold, interactionless

DM, for which $C[f] = 0$. Within this framework, and further assuming both a stationary distribution $\partial_t f = 0$ and a radial DM density scaling of $\rho_{DM} \sim r^{-2}$, we find a Maxwell-Boltzmann distribution

$$f(\mathbf{v}) = N_0 \exp\Big[-\mathbf{v}^2/v_0^2 \Big] \Theta(v_{\rm esc} - |\mathbf{v}|), \tag{1.7.2}$$

where the normalisation N_0 is

$$N_0 = \pi v_0^2 \left(\pi^{1/2} v_0 \,\mathrm{Erf}(v_{\rm esc}/v_0) - 2 v_{\rm esc} e^{-v_{\rm esc}^2/v_0^2} \right), \tag{1.7.3}$$

and numerically we have $v_0 = 230\,\mathrm{km/s}$, $v_{\rm esc} = 600\,\mathrm{km/s}$. We have further truncated the distribution at the galactic escape velocity $v_{\rm esc}$; this is somewhat violent, as this is no longer a stationary solution, but is nonetheless common practice. Note the large number of strong assumptions that went into this derivation. See Fig. 1.1 for a comparison of this distribution to numerical simulations of cold non-interacting DM.

This distribution is isotropic in the galactic frame. However, the solar system itself is moving through the galactic halo with a characteristic speed $v_e = 240\,\mathrm{km/s}$ in the direction of the constellation Cygnus, as illustrated in Fig. 1.2. Thus a DM detector co-rotating with the Earth will feel a DM wind whose direction changes throughout the day. Furthermore, the Earth is itself orbiting the Sun at around $30\,\mathrm{km/s}$, which induces an annual oscillation in the net velocity with respect to the halo.

1.7.4 Direct detection

The basic idea of traditional dark matter detection is simple: put a big block of well-understood stuff in a dark room, and wait for dark matter to scatter and deposit a measurable amount of energy in this stuff. Let's examine this more carefully.

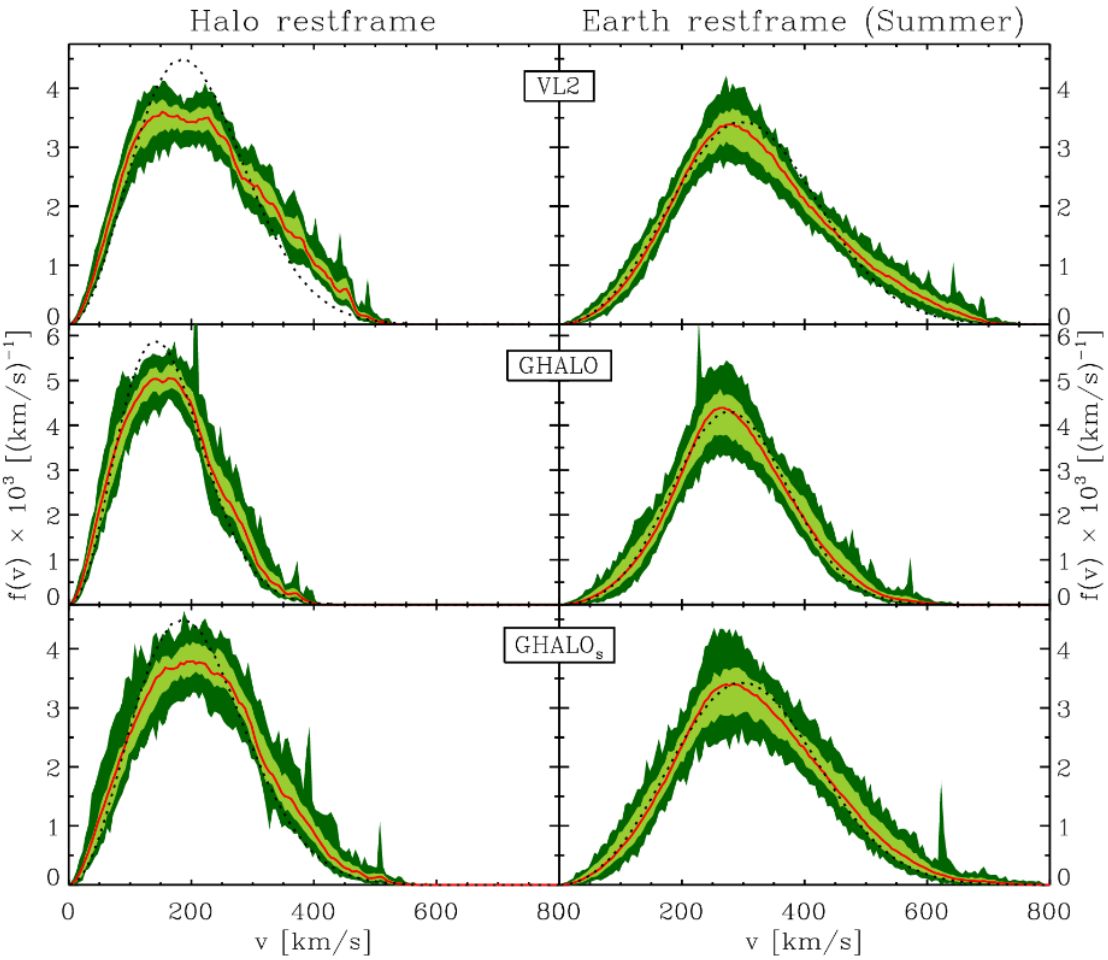

Figure 1.1: The result of N-body galactic simulations for the DM velocity distribution, taken from [42]. The red line shows the best-fit distribution with the one- and two-sigma variations in light and dark green. Compare with the dotted black Maxwell-Boltzmann distribution. The left panels show the result in the galactic frame, while the right panel is in the Earth's frame. Top-to-bottom shows different simulations.

We start with the kinematics of such a scattering process. Consider the case where the DM is heavy enough that a particle picture of two-body scattering is appropriate (as opposed to a wavelike DM scenario). In this case, the minimum velocity $v_{\rm min}$ needed to deposit some energy $E_{\rm dep}$ is dictated by energy-momentum conservation

$$v_{\rm min} = \left(\frac{E_{\rm dep} m_T}{2} \frac{(m_T + m_\chi)^2}{(m_T m_\chi)^2} \right)^{1/2}, \tag{1.7.4}$$

where m_T is the target constituent mass (e.g. the mass of a nucleon, or electron),

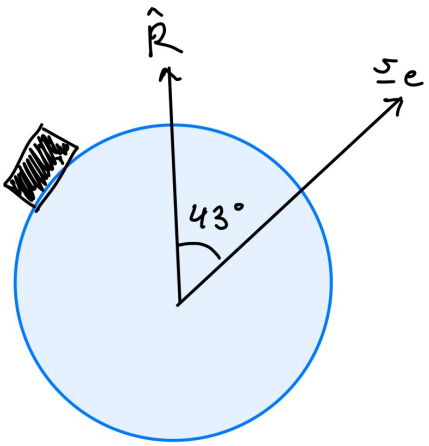

Figure 1.2: A detector (depicted as a black box) sitting on the surface of the Earth will be rotated through the DM wind with a period of a day. The detector's response must itself be anisotropic in order to measure this daily modulation, which can be large due to the large angle between the axis of rotation $\hat{R}$ and the direction of Earth's velocity $\mathbf{v}_e$.

and m_χ is the DM mass. In the limit where $m_\chi \ll m_T$, this simplifies to

$$v_{\text{min}} \simeq \left(\frac{E_{\text{dep}} m_T}{2m_\chi^2}\right)^{1/2}, \tag{1.7.5}$$

and so we see that the minimum velocity grows with the inverse of the DM mass. Once v_{min} is in the tail of Eq. (1.7.2), the probability of depositing a measurable amount of energy then falls exponentially. Thus for m_χ parametrically smaller than m_T, the sensitivity of any DM direct detection experiment falls steeply.

Traditional DM experiments have looked for WIMPs with a mass greater than a GeV. These have leveraged energy deposition on nuclei to obtain very strong constraints on DM of these masses. However, how does one look for lighter DM? An effective strategy is to look for scattering off of lighter particles. These can either be electrons, or, as I will focus on in Chapter **??**, emergent quasiparticles, such as magnons.

Chapter 2

Constraints on dark states coupling to photons from the BEBC WA66 beam dump experiment

Dark matter, although weakly interacting with the Standard Model, may couple directly to photons, e.g. in theories with kinetic mixing of our photon with a paraphoton [28]. If the paraphoton is massless, the model accommodates particles with a millicharge (mQ), allowing an apparent circumvention of charge quantisation. Alternatively, the coupling may be through operators of mass dimension higher than four; the dimension-five operators involving two fermions and a photon are magnetic dipole moments (MDMs) and electric dipole moments (EDMs). From an effective field theory (EFT) point of view, these operators generically constitute the three most relevant couplings of a dark Dirac fermion χ to photons.

The question of the existence of millicharged fermions has received far more attention than that of dark states with EDMs or MDMs (see [43, 44] for recent reviews). A dedicated search for millicharges was carried out at SLAC, placing limits in the mass range $0.1 - 100$ MeV [45]; data from LSND [46] and MiniBooNE [47] has been used to place similar constraints at the upper edge of this mass range [48]. Recently it was proposed [49] to use liquid argon detectors to carry out a search,

which was performed by the ArgoNeuT experiment, yielding bounds extending into the GeV range [50]. The prototype detector of the milliQan experiment at the LHC has placed new exclusions at masses around 1 GeV [51]. OPAL at LEP [52] probed larger masses up to 100 GeV [53], while bounds from CMS at LHC extend all the way up to a TeV [54]. There are also astrophysical bounds: supernovae constrain states with masses $m_\chi \lesssim 100\,\mathrm{MeV}$ [55], while stellar cooling constrains still lighter masses $m_\chi \lesssim 100\,\mathrm{keV}$ [56].

New states with dipole moments have previously been considered mainly in the context of dark matter [57, 58, 59, 60, 61]. More recently, there have been efforts to bound these operators without making any assumptions concerning their relic abundance. Data from L3 at LEP II [62] places strong limits [63], as do high intensity fixed-target experiments [64]. The latter will be the focus of this work.

Past beam dump experiments strongly constrain the photon coupling to any possible new degrees of freedom [64]. In many cases, however, the backgrounds of these experiments are poorly understood, and the corresponding bounds therefore fold in uncertain assumptions. Data from the Big European Bubble Chamber (BEBC) WA66 beam dump experiment [65] was however used some years ago to carry out a *dedicated* search for a MDM of the tau neutrino [66]. Earlier data from the same experiment had been used to set bounds on light gluinos [67] and heavy neutral leptons [68]. Very recently, this data has also been used to bound a model with a heavy dark photon from consideration of a limited number of meson decays [69]. Nevertheless the BEBC WA66 experiment appears to have been largely forgotten in the recent revival of interest concerning the dark sector, even though its sensitivity is still competitive as we will demonstrate below.

In this work we recast the BEBC data in terms of the minimal model of electromagnetic interactions arising from a massless dark photon, and more generally in terms of EDMs and MDMs. In these cases the parameter space is spanned simply by the mass m_χ of the electromagnetically interacting Dirac fermion χ and the

coupling constant $Q_\chi = \epsilon e$, d, or μ for mQs, EDMs or MDMS, respectively. These parameters enter the Lagrangian through

$$\mathcal{L}_{\text{int}} = \epsilon e A_\mu \bar{\chi}\gamma^\mu \chi + \frac{1}{2}\mu F_{\mu\nu}\bar{\chi}\sigma^{\mu\nu}\chi + \frac{i}{2}dF_{\mu\nu}\bar{\chi}\sigma^{\mu\nu}\gamma^5\chi, \tag{2.0.1}$$

where $\sigma^{\mu\nu} \equiv i[\gamma^\mu, \gamma^\nu]/2$; this Lagrangian is written in a basis where the photon-dark photon system is diagonal. We express dipole moments in units of the Bohr magneton $\mu_B = e/2m_e$, use rationalised units such that $\epsilon_0 = 1$, and consider a situation in which couplings are turned on one at a time.

2.1 BEBC

The operating principle of fixed-target proton experiments is simple. A large number of secondaries are created when a beam of protons is directed on a dump. The length of the dump is critical for the type of particles produced. For a thin (beryllium) target, such as that used for CHARM II [70], the dominant production channel of sufficiently light charged particles is charged pion decay. This is also the main source of the conventional background of neutrinos. When however a thick (copper) target is used as for BEBC [65], these charged pions are absorbed before decaying since the mean interaction time is shorter than their lifetime.

The dark states of interest here, coupling only to photons, are mainly produced by scalar mesons that decay into photons, e.g. neutral pions, or heavy vector mesons that usually decay into $\ell^+\ell^-$ pairs. Given the short lifetime of these mesons, such dark states may still be produced in the thick target of BEBC. Any particles produced with a sufficiently weak coupling then traverse some intervening distance, and may then scatter off electrons in a detector downstream of the dump to leave an observable signal.

The BEBC detector was 404 m downstream of a 400 GeV proton beam from the

Experiment	POT/10^{18}	E_b/GeV	D/m	$n_e/10^{23}\,\mathrm{cm}^{-3}$	V/cm^3	Cuts	Observed	η
BEBC [65, 66]	2.72	400	404	2.6	$357 \times 252 \times 185$	$E_e > 1\,\mathrm{GeV}$ $\wedge E_e\theta_e^2 < 2m_e$	1	0.8
CHARM II [70, 71]	25	450	870	4.3	$370 \times 370 \times 3567$	$E_e \in [3, 24]\,\mathrm{GeV}$ $\wedge E_e\theta_e^2 < 2m_e$	5429 ± 120	0.57
SHiP (proposed) [72]	200	400	56.5	19	$187 \times 69 \times 87$	$E_e \in [1, 20]\,\mathrm{GeV}$ $\wedge\theta_e \in [10, 20]\,\mathrm{mrad}$	284 (forecast)	0.5

Table 2.1: The relevant experimental parameters for BEBC and CHARM II, and those projected for SHiP. POT is the total number of protons on target, either actual or predicted. E_b is the energy of proton beam. D is the distance from the end of the target to the beginning of the detector. n_e is the detector's electron density; in the case of CHARM II and SHiP, an effective density is given to account for their active layers. V is the detector volume written as transverse area $\times$ length; the dimensions of BEBC are given approximating the detector as a cuboid. Cuts are placed on the kinetic energy of the electron E_e and on the angle θ_e between the beam axis and recoil electron. The number of observed events is given for BEBC and CHARM II, and the expected background for SHiP. The detection efficiency after cuts is denoted η.

CERN SPS dumped onto a solid copper block [65]. A total of 2.72×10^{18} protons on target were accumulated over the experiment. The detector itself had a fiducial volume of 16.6 m^3 filled with a neon-hydrogen mixture. A dedicated search for elastically scattered final state electrons was carried out, with one candidate event observed [66]. Relevant details of the BEBC WA66 experiment are given in Table 3.1 as well as those of CHARM II, along with the proposed SHiP for comparison.

2.2 Dark state signatures at beam dumps

In this section, we detail the calculation of the number of dark states entering the detector and their subsequent scattering. We focus on the dominant production channels, which are meson decays, with Drell-Yan forming a highly subdominant component. The dark state flux is handled primarily by the MadGraph plugin MadDump [73, 74], which provides the distribution of scattered electrons in the detector differential in both energy and angle. The following procedures were validated by reproducing the total number of electron scatterings due to the Standard Model interactions of the neutrino flux measured by CHARM II.

2.2.1 Meson decays

The number of dark matter particles N_χ produced in neutral meson decays is given by

$$N_\chi = 2N_{\rm POT} \sum_{\mathfrak{m}} N_{\mathfrak{m}/\rm POT} {\rm Br}(\mathfrak{m} \to \chi\bar{\chi} + \text{anything}), \tag{2.2.1}$$

where $N_{\rm POT}$ is the number of protons on target (POT), and $N_{\mathfrak{m}/\rm POT}$ is the number of a particular meson $\mathfrak{m}$ produced per POT. Meson production can be approximated from fixed-target pp collisions simulated in PYTHIA 8.3 [75, 76], ignoring for simplicity the fraction of production in hadronic cascades. We then scale cross sections according to the nucleon number of the target A to some power. In reality, this scaling index depends on the kinematics of the process, since mesons can re-interact within a single large nucleus and produce softer secondary products, but when approximating the target as a dilute gas we stipulate a scaling of $A^{2/3}$. The number of mesons we thus estimate to be produced per pp collision are listed in Table 2.2.

The meson decay into DM is characterised by the branching fraction; parity invariance restricts the decay of the pseudoscalars $\mathfrak{s} = \pi^0, \eta$, while the small value of α implies that

$$\begin{aligned} {\rm Br}(\mathfrak{s} \to \chi\bar{\chi} + \text{anything}) &\simeq {\rm Br}(\mathfrak{s} \to \chi\bar{\chi}\gamma), \\ {\rm Br}(\mathfrak{v} \to \chi\bar{\chi} + \text{anything}) &\simeq {\rm Br}(\mathfrak{v} \to \chi\bar{\chi}), \end{aligned} \tag{2.2.2}$$

where we include vector mesons $\mathfrak{v} = \rho, \phi, J/\psi$. For ω mesons, we find that for light millicharged dark states there is also a significant contribution from the decay into a neutral pion and a dark pair, as detailed in Appendix 2.A. Hence we have

$$\text{mQ}: \quad {\rm Br}(\omega \to \chi\bar{\chi} + \text{anything}) \simeq {\rm Br}(\omega \to \chi\bar{\chi}) + {\rm Br}(\omega \to \chi\bar{\chi}\pi^0), \tag{2.2.3}$$

$$\text{MDM, EDM}: \quad {\rm Br}(\omega \to \chi\bar{\chi} + \text{anything}) \simeq {\rm Br}(\omega \to \chi\bar{\chi}). \tag{2.2.4}$$

The value of the branching ratios can be related to measured Standard Model

E_b/GeV	π^0	η	ω	ρ	ϕ	J/ψ
400	4.0	4.6×10^{-1}	5.3×10^{-1}	5.3×10^{-1}	1.9×10^{-2}	6.4×10^{-6}
450	4.2	4.7×10^{-1}	5.5×10^{-1}	5.6×10^{-1}	2.0×10^{-2}	6.6×10^{-6}

Table 2.2: The number of mesons produced per proton-proton collision at the relevant energies, using SoftQCD.

branching ratios after calculating the respective rates, as outlined in Appendix 2.A.

Although the overall normalisation of the dark state flux depends only on the branching ratios, to determine the kinematic properties requires a more detailed analysis. First, the angular and energy distribution of the meson flux is needed. One possibility is to use experimentally measured distributions. However for neutral pions, this distribution is highly uncertain due to the difficulty of the measurement. Previous works have chosen to invoke isospin invariance to treat the neutral pion distribution as the average of those for charged pions [77, 64]. However, since the charged pions are much longer lived, one expects the neutral pions to be scattered less within the target. The heavier mesons tend to have smaller momenta and thus to be more widely distributed, and so are unlikely to follow the same distribution as pions. We thus choose to specify the distribution instead using the full information obtained from Pythia. The χ distributions differential in angle and energy and shown in Figs 2.1 and 2.2, respectively.

To calculate the dark state spectrum, we use the Monte Carlo techniques implemented by MadDump [74]. This programme takes the meson spectrum as an input and outputs the dark state distribution using an EFT framework for the interactions. In the case of pseudoscalar mesons, the decay proceeds via an off-shell photon involving the interaction vertex dictated by the chiral anomaly

$$\mathcal{L}_\mathfrak{s} \supset \frac{1}{F_\mathfrak{s}} \mathfrak{s} F^{\mu\nu} \tilde{F}_{\mu\nu}; \tag{2.2.5}$$

Note that the value of the decay constants here are irrelevant as we normalise to the observed Standard Model decay: $\mathfrak{s} \to \gamma\gamma$.

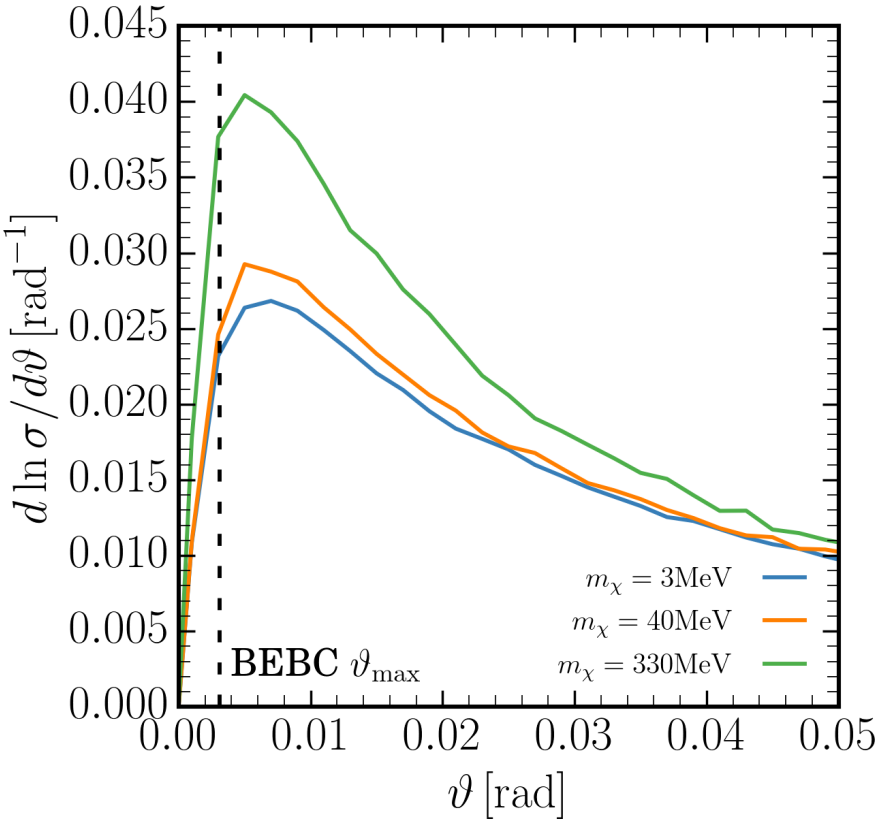

Figure 2.1: The differential angular distribution of dark states emerging from the beam dump.

For dark states produced by vector meson decays, we invoke vector meson dominance, i.e. assume that the dominant interaction between vector mesons and photons occurs through mixing terms, which is in agreement with experimental data [78, 79]. Thus, the decays of vector mesons $\mathfrak{v}$ occur by mixing into an off-shell photon which can then decay into a dark state pair. To implement this into MadDump, we diagonalise the Lagrangian in the $(A^\mu, \mathfrak{v}^\mu)$ space. These two bases can be related by a series of two linear transformations, after which the original photon interactions of Eq.(2.0.1) result in three-point couplings between vector mesons and dark states, for instance

$$\mathcal{L}_\mathfrak{v} \supset c\epsilon e \mathfrak{v}^\mu \bar{\chi}\gamma_\mu\chi \tag{2.2.6}$$

in the case of a millicharged particle; the constant c depends on the couplings

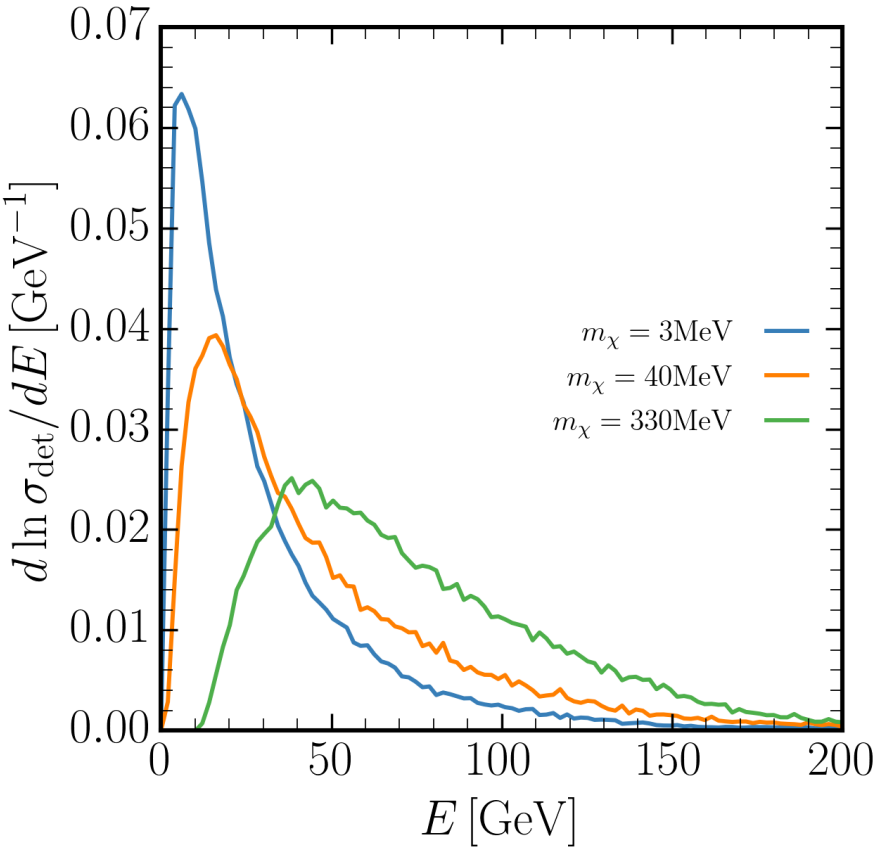

Figure 2.2: The differential energy distribution of dark states entering the BEBC detector.

occurring in the original meson-photon mixing Lagrangian but their precise values are unimportant in practice once we normalise to the process $\mathfrak{v} \to e^+e^-$.

After any dark states are produced, they propagate downstream of the dump through several hundred metres of material.[1] The geometric acceptance $\varepsilon_{\rm geo}$ denotes the fraction of the dark states that then enter the detector. This is a function of both the angular distribution of the states as well as the angular size of the detector. Since the CERN SPS beam used by CHARM II and BEBC operated at high energies, most of the mesons produced in the dump had a large Lorentz boost Γ in the forward direction. Going from the meson rest-frame to the lab-frame thus focusses the emitted dark states into a cone of opening angle $\vartheta \sim 1/\Gamma$. We find

[1]It is theoretically possible that the states may interact strongly enough to be attenuated *en route* to the detector, although this possibility is ruled out in practice by constraints from other experiments.

$\varepsilon_{\text{geo}} \sim 0.01$, which is much larger than the fractional solid angles of the detectors.

2.2.2 Drell-Yan production

The dark states may also be produced by the Drell-Yan process. This is however subdominant to all the meson decays we consider, and so only becomes relevant when all other production processes are kinematically excluded, i.e. for m_χ above half the J/ψ mass. We again model this using MadGraph through MadDump. Although states with masses beyond a few GeV can be produced in this way by the CERN SPS beam, the increase in sensitivity in this mass region is negligible. The scattering detection process we consider is only on electrons in the detector, as we detail in the next section. The GeV electron recoil energy thresholds of BEBC and CHARM II are too high to detect any scattering events of these heavy states, since the dark states do not have high enough Lorentz factors Γ to deposit such large energies, with the maximum energy transfer scaling as $m_e\Gamma^2$. Consideration of deep inelastic scattering events does not change this conclusion.

2.2.3 Dark state-electron scattering

The dark states that enter the detector may either scatter via photon exchange off electrons or undergo deep inelastic scattering with the nucleons, however electron scattering dominates. We may write the total number of scattering events $N_{e\chi}$ as a function of final electron energy E_e as

$$N_{e\chi} = \varepsilon_{\text{geo}} L n_e \int dE_\chi \frac{dN_\chi}{dE_\chi} \sigma_{e\chi}(E_\chi), \tag{2.2.7}$$

where ε_{geo} is the geometric acceptance as defined in the previous section, L is the longitudinal detector length, n_e is the number density of electrons, N_χ is given by Eq.(2.2.1), and $\sigma_e\chi$ is the cross section for electron-chi scattering.

Due to the experimental cuts and their finite resolutions, not all of these events

can be detected. We take this into account by counting the number of events that survive the cuts on the electron angle with respect to the beam θ_e as well as on the electron energy E_e. The ratio of this number to $N_{e\chi}$ is denoted $\varepsilon_{\rm cut}$, so that the total number of detected scattering events N is given by:

$$N = \eta \varepsilon_{\rm cut} N_{e\chi}, \tag{2.2.8}$$

where η is the detector's efficiency. In practice, this scattering is handled by MadDump.

Cuts were applied on the electron energy E and scattering angle θ of $E\theta^2 < 2m_e$ translating into a cut on the t-channel of approximately $t \lesssim -1 \times 10^{-3}$ GeV. This cut corresponds to the maximum expected scattering angle possible for incoming massless particles which are perfectly collimated along the beam axis, as was appropriate for neutrino experiments. This cut may be overzealous, as we find the non-zero spread of the incoming flux has on $\mathcal{O}(1)$ effect on the signal passing the selection cut at BEBC, even in the massless limit. For an electron with the minimum detected energy at BEBC of 1 GeV, the selection criterion $E_e\theta_e^2 < 2m_e$ means the scattering angle must satisfy $\theta_e \lesssim 0.03$ rad. Comparing this with the 9 mrad opening angle of the detector, we see that the detector angle is not negligible compared to the scattering angle cut, even at the low energy end of the tail. This in fact leads to about half of the signal events being thrown away.

2.3 Discussion

We now consider the bounds on the size of the electromagnetic coupling of dark states arising from the BEBC and CHARM II beam dump experiments. As already mentioned, a single elastically scattered electron was observed at BEBC. This event was likely due to neutrino electroweak scattering, which was carefully estimated to

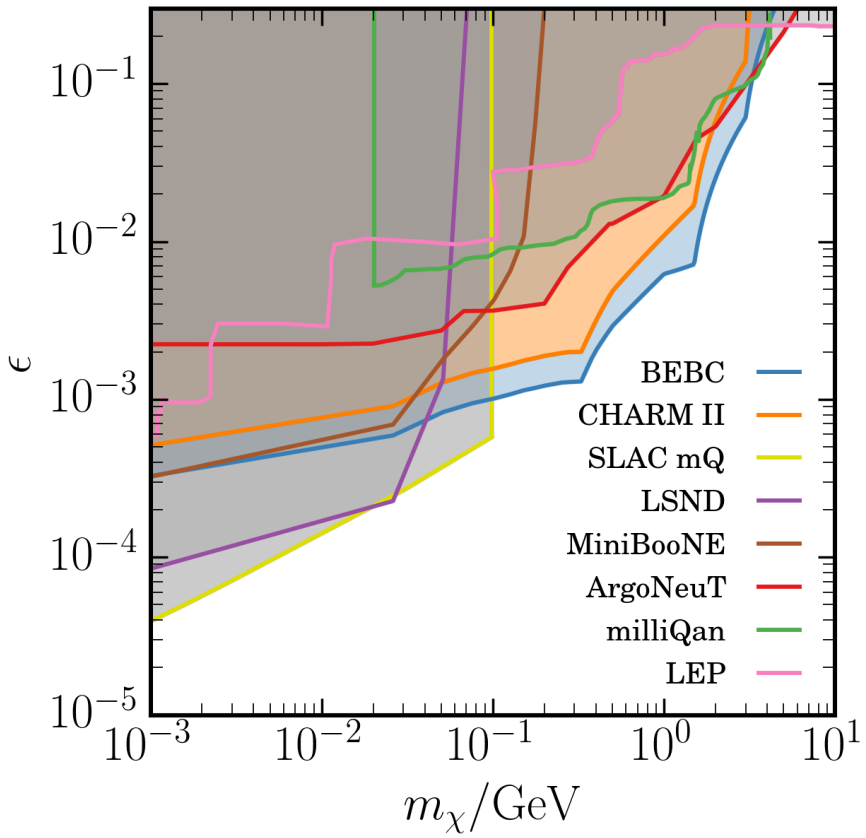

Figure 2.3: The 90% upper limit on the size of the millicharge $\epsilon = Q_\chi/e$ from CHARM II and BEBC. All regions shaded in grey are already excluded at 90% by: SLAC [45]; LSND and MiniBoone [48]; ArgoNeuT [50]; milliQan [51]; and LEP [53].

comprise a background of 0.5 ± 0.1 events [66]. The 90% CL upper limit on signal events is then 3.5.

The bounds from CHARM II are obtained by considering the sum of the observed electron events: 2677 ± 82 in the neutrino beam, and 2752 ± 88 in the anti-neutrino beam, making up 5429 ± 120 events. In the absence of any experimentally calibrated estimate of the background, we take the number of background events to be simply equal to the number of observed events. Assuming a Gaussian distribution, this places a 90% CL upper limit of 154 signal events. It may be that in fact the expected background is larger (smaller) than the number of observed events so the true bounds from CHARM II could be weaker (stronger) than those we find.

The bounds on millicharged particles coming from BEBC and CHARM II are

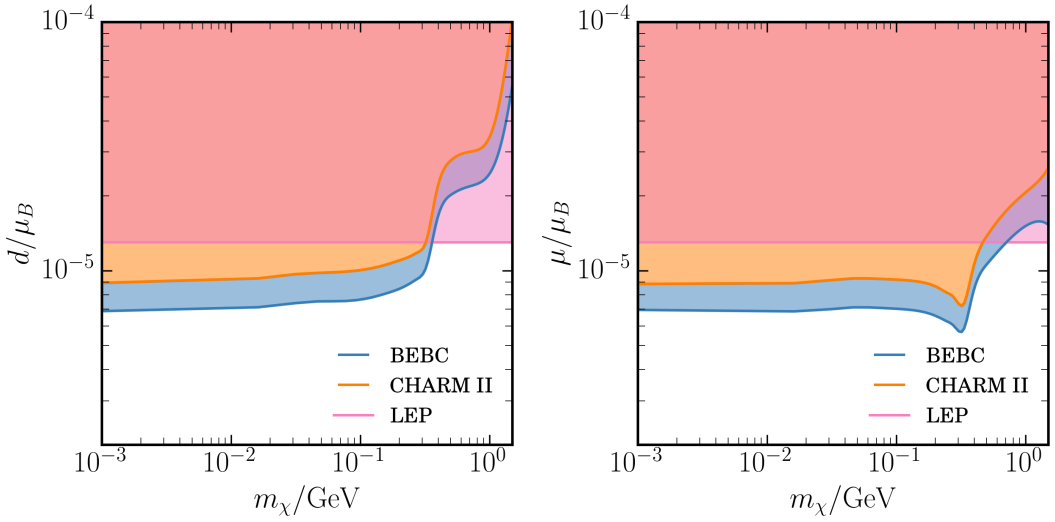

Figure 2.4: The 90% upper limit exclusion regions for electric d (left) and magnetic μ (right) dipole moments, measured in Bohr magnetons μ_B. The bounds from L3 at LEP II [63] are also shown. The CHARM II bounds we derive here agree with those found earlier [64] and are less restrictive than those of BEBC.

shown in Fig. 2.3. The limits are improved on by subsequent experiments for masses below 100 MeV. However for heavier states, the higher energy of the CERN SPS beam becomes significant. The heavier mesons that are produced may decay into dark states of mass up to ~ 1 GeV, thus extending the reach by orders of magnitude. The two beam dumps have comparable sensitivities, although the combination of the lower energy threshold, larger angular size and lower backgrounds of BEBC allows it to probe somewhat deeper than CHARM II, notwithstanding the latter's much larger size.

For EDMs and MDMs, BEBC places the leading experimental bound and asymptotes to $d, \mu < 6.9 \times 10^{-6}\ \mu_B$ as shown in Fig. 2.4. The bounds tend to the same value for both operators, since in the relativistic limit the introduction of the γ^5 matrix in the EDM matrix elements leads only to a relative sign compared to MDM matrix elements, which is irrelevant for the observable here. At higher masses, there are fewer heavy mesons produced, while the high centre-of-mass energy of LEP has a larger role than in the SLAC mQ case. Hence the bounds we derive from BEBC become weaker than those from L3 at LEP II beyond a few hundred MeV.

The bound from CHARM II, which at low masses goes down to $d, \mu < 9.0 \times 10^{-6}\ \mu_B$, is slightly worse that the CHARM II bound of $\sim 8 \times 10^{-6}\ \mu_B$ found in previous work [64]. This may be explained by the combination of a number of factors: we find somewhat fewer dark states enter the detector due to our different method of treating the meson production, as explained in § 2.2.1; the true CHARM II cut we use is somewhat more restrictive than that used in [64]; we use a lower electron detection efficiency; additionally, as mentioned at the end of § 2.2.3, the finite angular size of the dark state flux cone can have $\mathcal{O}(10\%)$ effects.

What do these bounds imply for the scale of new physics Λ, assuming that the the dark dipole moments are induced by loop effects? Due to the necessary chiral flip involved in these operators, we expect that the size of the moments scales as m_χ/Λ^2, and so we expect

$$\Lambda \sim \text{GeV} \left(\frac{10^{-2}\,\text{GeV}}{m_\chi} \right)^{1/2}; \tag{2.3.1}$$

of course, there are no new charged states appearing at a GeV, and so this new physics must be weakly coupled in order to evade experimental bounds. Alternatively, the new physics may not arise from loops, but may for instance arise through compositeness (such as a dark neutron coupling through a kinetically mixed dark photon), and so would circumvent the above logic.

We have shown that the BEBC WA66 beam dump experiment [65] carried out in 1982, which was previously used for a number of novel searches [68, 67, 66], continues to place world-leading bounds on several 'dark currents' coupling to photons. This lends further support to the proposal to reexamine neutrino data in the search for new dark states [80]. We expect that similar improved bounds may be placed using BEBC data on other feebly interacting particles of current interest [44], in particular heavy neutral leptons [81].

Figure 2.5: The Feynman diagrams corresponding to scalar meson decay (left), and vector meson decay (right). The scalar meson must decay into dark states in association with a photon due to angular momentum conservation, while the vector may directly decay to the dark pair.

2.A Details of meson decays

As mentioned in the main body of the text, the normalisation of the number of dark states coming from meson decays is set by the corresponding branching ratio: $\mathrm{Br}(\mathfrak{s} \to \chi\bar{\chi}\gamma)$ for scalar mesons, $\mathrm{Br}(\mathfrak{v} \to \chi\bar{\chi})$ for the vectors, as well as $\mathrm{Br}(\omega \to \pi^0\chi\bar{\chi})$. In this Appendix, we calculate these rates and reproduce for completeness many of the relevant key formulae of Refs.[82, 64], to which we refer the reader for further details. The Feynman diagrams corresponding to the two cases are shown in Fig. **??**

The branching ratio for dark decays of scalar mesons can be related to the known branching ratio of some Standard Model process. In general, the ratio of the branching ratios is given by the ratio of the corresponding rates. The simplest ratio to calculate in this case is dark decay relative to the decay into two photons, i.e.

$$\mathrm{Br}(\mathfrak{s} \to \chi\bar{\chi}\gamma) = \frac{\Gamma(\mathfrak{s} \to \chi\bar{\chi}\gamma)}{\Gamma(\mathfrak{s} \to \gamma\gamma)}\mathrm{Br}(\mathfrak{s} \to \gamma\gamma). \tag{2.A.1}$$

This ratio factorises nicely if the momentum-transfer-dependence of the meson electromagnetic form factors is neglected. Such an approximation is adequate, since the running of the form factor occurs as the photon mixes with the ρ meson, which is a negliglible effect for the light scalars considered here, as numerically confirmed in

[82]. The expressions for the decay rates are [82]

$$\Gamma(\mathfrak{s} \to \chi\bar{\chi}\gamma) = \int_{4m_\chi^2}^{m_\mathfrak{s}^2} ds_{\chi\bar{\chi}}\, \Gamma_{\gamma\gamma^*}(s_{\chi\bar{\chi}}) \frac{f_\chi\left(s_{\chi\bar{\chi}}\right)}{16\pi^2 s_{\chi\bar{\chi}}^2} \sqrt{1 - \frac{4m_\chi^2}{s_{\chi\bar{\chi}}}}, \tag{2.A.2}$$

where $m_\mathfrak{s}$ is the scalar meson mass and

$$\Gamma_{\gamma\gamma^*}(s_{\chi\bar{\chi}}) = \frac{\alpha^2 \left(m_\mathfrak{s}^2 - s_{\chi\bar{\chi}}\right)^3}{32\pi^3 m_\mathfrak{s}^3 F_\mathfrak{s}^2}, \tag{2.A.3}$$

is the decay rate of a scalar meson to two photons, one real and one of virtuality $s_{\chi\bar{\chi}}$; then $\Gamma(\mathfrak{s} \to \gamma\gamma) = \Gamma_{\gamma\gamma^*}(0)$. Note that the final branching ratio is independent of the meson decay constants $F_\mathfrak{s}$ in this approximation. The expressions for $f_\chi(s)$ depend on the particular interaction term being considered, and were calculated in [82] to be

$$\begin{aligned}
\text{mQ} : f_\chi\left(s\right) &= \frac{16\pi\alpha}{3}\epsilon^2 s \left(1 + \frac{2m_\chi^2}{s}\right), \\
\text{MDM} : f_\chi\left(s\right) &= \frac{2}{3}\mu^2 s^2 \left(1 + \frac{8m_\chi^2}{s}\right), \\
\text{EDM} : f_\chi\left(s\right) &= \frac{2}{3}d^2 s^2 \left(1 - \frac{4m_\chi^2}{s}\right).
\end{aligned} \tag{2.A.4}$$

The vector meson branching ratio into pure dark states is obtained similarly, and is most simply given by

$$\text{Br}(\mathfrak{v} \to \chi\bar{\chi}) = \frac{\Gamma(\mathfrak{v} \to \chi\bar{\chi})}{\Gamma(\mathfrak{v} \to e^- e^+)} \text{Br}(\mathfrak{v} \to e^- e^+). \tag{2.A.5}$$

Under the vector meson dominance hypothesis, the mixing terms between the vectors and the photon imply that any terms in the Lagrangian involving the "original" non-diagonalised photon field in fact involve some linear combination of the diagonal fields. Hence Eq. (2.0.1) gives rise to a direct interaction between the diagonalised vector meson and the dark states. Both of the decays in Eq.(2.A.5) have just two-

body final states so the phase spaces contributions factorise, while the meson form factors in both cases enter at the same momentum-transfer $m_{\mathfrak{v}}^2$, leaving

$$\frac{\Gamma(\mathfrak{v} \to \chi\bar{\chi})}{\Gamma(\mathfrak{v} \to e^- e^+)} = \frac{f_\chi(m_{\mathfrak{v}}^2)}{f_e(m_{\mathfrak{v}}^2)} \sqrt{\frac{1 - 4m_\chi^2/m_{\mathfrak{v}}^2}{1 - 4m_e^2/m_{\mathfrak{v}}^2}}, \tag{2.A.6}$$

where $f_e(s)$ is analogous to the millicharge f_χ:

$$f_e(m_{\mathfrak{v}}^2) = \frac{16\pi\alpha}{3} m_{\mathfrak{v}}^2 \left(1 + \frac{2m_e^2}{m_{\mathfrak{v}}^2}\right). \tag{2.A.7}$$

The final branching ratio concerns the decay of a vector meson into a pion and a dark pair, which we normalise to the branching ratio into a pion and photon:

$$\mathrm{Br}(\mathfrak{v} \to \chi\bar{\chi}\pi^0) = \frac{\Gamma(\mathfrak{v} \to \chi\bar{\chi}\pi^0)}{\Gamma(\mathfrak{v} \to \pi^0\gamma)} \mathrm{Br}(\mathfrak{v} \to \pi^0\gamma) \tag{2.A.8}$$

The relevant interactions here come from the original chiral anomaly term coupling the pion to $\mathfrak{s}F\tilde{F}$. Diagonalisation turns this interaction into a sum of two new interactions: a term involving a vector meson and a photon, and a term involving two vector mesons. Assuming the mixing terms are sufficiently weak, we may, to leading order, consider only the interaction involving a photon and vector meson, which we show below to be valid. The decay rate for this process is then:

$$\Gamma(\mathfrak{v} \to \chi\bar{\chi}\pi^0) = \int_{4m_\chi^2}^{(m_{\mathfrak{v}} - m_\pi)^2} ds_{\chi\bar{\chi}}\, \Gamma_{\pi^0\gamma^*}(s_{\chi\bar{\chi}}) \frac{f_\chi\left(s_{\chi\bar{\chi}}\right)}{16\pi^2 s_{\chi\bar{\chi}}^2} \sqrt{1 - \frac{4m_\chi^2}{s_{\chi\bar{\chi}}}}, \tag{2.A.9}$$

where

$$\frac{\Gamma_{\pi^0\gamma^*}(s_{\chi\bar{\chi}})}{\Gamma(\mathfrak{v} \to \pi^0\gamma)} = \frac{m_{\mathfrak{v}}^2 (m_\pi^2 - m_{\mathfrak{v}}^2 - s_{\chi\bar{\chi}})^2}{(m_{\mathfrak{v}}^2 - m_\pi^2)^3} \sqrt{1 - \frac{2(m_\pi^2 + s_{\chi\bar{\chi}})}{m_{\mathfrak{v}}^2} + \frac{(s_{\chi\bar{\chi}} - m_\pi^2)^2}{m_{\mathfrak{v}}^4}}, \tag{2.A.10}$$

is the rate of vector meson decay into a pion and photon of virtuality $s_{\chi\bar{\chi}}$ compared to the corresponding on-shell rate, and $m_{\mathfrak{v}}$ and m_π are the vector meson and pion

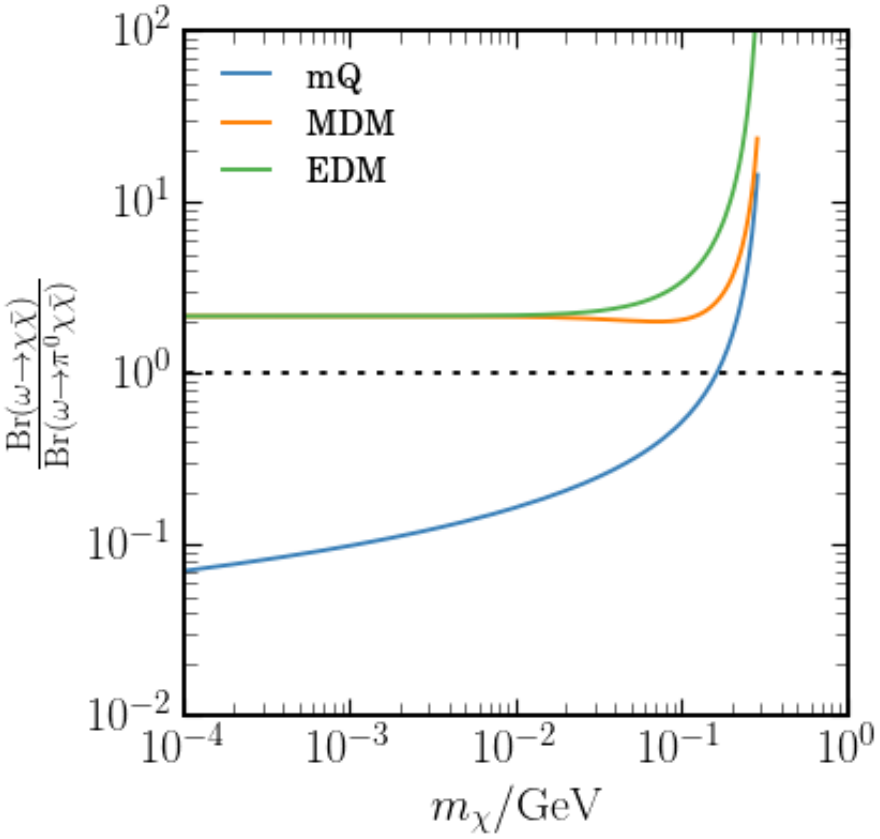

Figure 2.6: The ratio of the two branching ratios for the ω meson's two main decay channels involving a dark pair, as given by equations (2.A.5) and (2.A.8). For the dimension-5 operators, MDM and EDM, the decay involving a pion is always at least marginally subdominant, whereas for mQ there are dark state masses for which the 3-body decay is dominant.

mass, respectively. As a check on the weak-mixing assumption, we use the above expression to find $\mathrm{Br}(\omega \to \pi^0 e^+ e^-) = 8.3 \times 10^{-4}$ and $\mathrm{Br}(\omega \to \pi^0 \mu^+ \mu^-) = 1.3 \times 10^{-4}$, both of which are within 10% of their experimental value.

The relative importance of this decay channel compared to the decay without a pion depends on the particular form of the interaction as well as the value of m_χ (see Fig. 2.6). EDMs and MDMs are higher dimension operators than the standard electromagnetic current, resulting in a stronger energy dependence. The reduced phase space associated with the decay into a dark pair and a pion then has much more of an effect on particles coupling through the former operators, so in such cases we can consider this channel to be negligible.

However for low mass millicharges, the decay channel involving a pion is dominant. At very low mass, pion decay is the dominant production mode, but at higher masse when this channel starts to shut off, the inclusion of $\omega \to \chi\bar{\chi}\pi^0$ can make $\sim 5\%$ difference to the bounds. At even higher mass, this ω decay channel becomes negligible but including $\omega \to \chi\bar{\chi}$ yields $\sim 10\%$ improvement. Hence we include both channels to accurately cover the whole range of masses.

Statement of Authorship for joint/multi-authored papers for PGR thesis

To appear at the end of each thesis chapter submitted as an article/paper

The statement shall describe the candidate's and co-authors' independent research contributions in the thesis publications. For each publication there should exist a complete statement that is to be filled out and signed by the candidate and supervisor **(only required where there isn't already a statement of contribution within the paper itself).**

Title of Paper	**Blast from the past: Constraints on the dark sector from the BEBC WA66 beam dump experiment**
Publication Status	X Published ☐ Accepted for Publication ☐Submitted for Publication ☐Unpublished and unsubmitted work written in a manuscript style
Publication Details	Giacomo Marocco & Subir Sarkar, *SciPost Physics* 10 (2021) 2, 043 [https://doi.org/10.21468/SciPostPhys.10.2.043]

Student Confirmation

Student Name:	Giacomo Marocco		
Contribution to the Paper	Performed the analysis and co-wrote the paper		
Signature 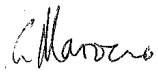		Date	27/07/22

Supervisor Confirmation

By signing the Statement of Authorship, you are certifying that the candidate made a substantial contribution to the publication, and that the description described above is accurate.

Supervisor name and title: Professor Subir Sarkar		
Supervisor comments: Giacomo carried out the analysis under my guidance to extract limits on millicharged dark states, as well as particles with electric or magnetic dipole moments, from the CERN-WA-066 beam dump experiment. He also participated in writing the paper and acted as the corresponding author with the journal.		
Signature 	Date	27 July 2022

This completed form should be included in the thesis, at the end of the relevant chapter.

Chapter 3

Constraints on heavy neutral leptons from the BEBC WA66 beam dump experiment

3.1 Introduction

Neutrinos have small but non-zero masses, the origin of which is unknown. An attractive explanation involves extending the Standard Model (SM) by adding to it right-handed neutrinos, thus generating small masses for the left-handed neutrinos e.g. by the inverse-seesaw mechanism [83]. Such models have open parameter space where the heavy neutral leptons (HNL) mix only with a single flavour of (left-handed) neutrinos [84]; our goal in this work is to bound the currently least constrained possibility of mixing between HNLs and the tau neutrino only.

In this simple model, an HNL N has a Majorana mass m_N and mixes with the ν_τ with a strength given by $U_{\tau N}$. The corresponding addition to the SM Lagrangian is

$$\mathcal{L} \supset i\bar{N}\partial\!\!\!/ N + M_\alpha \bar{\nu}_\alpha N - \frac{1}{2} m_\alpha \bar{N^c} N + \text{h.c}, \tag{3.1.1}$$

where the mass mixing m_α with the flavour eigenstates ν_α arises from one of the few

renormalisable operators — the so-called neutrino portal — that may consistently be added to the Standard Model to couple it to a 'dark sector', so is a promising target in the search for new physics just beyond the electroweak scale. In terms of the Lagrangian parameters, the dimensionless mixing is given by

$$U_{\tau N} = \frac{M_\tau}{m_N}, \tag{3.1.2}$$

having set the other elements of the mass mixing matrix to zero for this particular HNL. The PMNS matrix will induce a further mixing between N and the other SM neutrinos, but this is suppressed by $(m_\nu/E_\nu)^2$, which is small at the high energy beam dumps we consider.

Many constraints exist on the $m_N - U_{\tau N}$ parameter space — see [85] for a thorough review and discussion of projected sensitivities of proposed experiments, especially at the proposed LHC Forward Physics Facility. Below the kaon mass, the ND280 detector at T2K places strong bounds [86], as does the CERN PS191 experiment [87]. For masses extending up to a GeV, the ArgoNeuT experiment set limits [88] but there are better bounds from B factories [89], in particular BABAR [90] and Belle [91]. The strongest constraint comes however from reanalysis [92, 93, 94] of the old bound from the CHARM beam dump experiment [95]. At still higher masses, DELPHI at LEP constrained HNLs that may be produced in Z-decays [96]. Complementing laboratory experiments, arguments based on big bang nucleosynthesis [97] are relevant in regions of parameter space where the HNLs do not decay before the beginning of this epoch [98, 99]. Since the strength of most of the former bounds weakens above the kaon mass, we focus in this work on $m_N \gtrsim 500$ MeV .

Data from the Big European Bubble Chamber (BEBC) CERN-WA66 beam dump experiment [65] was used already to carry out a dedicated search for HNLs [100]. However in that analysis only HNL production (and decay) via mixing with

electron and muon neutrinos was considered. The production of HNLs in τ decays was not considered nor were decays via neutral currents taken into account, as we do in this work. Given that BEBC still places world-leading bounds on a variety of other new physics of interest such as dark photons [69], magnetic moments and milli-charged particles [1], it is worth reassessing its sensitivity to HNLs as well. We also perform a reanalysis of bounds for an HNL mixing with ν_e, in order to include all the relevant decay modes and determine a more precise bound on the mixing parameter, as well as correcting a decay rate in [100] that omitted an interference contribution.

3.2 Heavy neutrino production

The flux of HNLs produced in the beam dump is specified by the absolute number of HNLs produced, $\mathcal{N}_N$, as well as their differential distribution, $\mathrm{d}^3\mathcal{N}_N$ in energy and momentum. We first focus on calculating the latter.

For a production channel labelled by i, once the initial distribution $\mathrm{d}^3\sigma_i$ of the parent and the decay distribution $\mathrm{d}^3\mathcal{N}_i$ of the child are known, the child's distribution in the lab frame is readily obtained. It is necessary to integrate over these distributions on the subspace where the boost brings the cms momentum to the lab-frame momentum in question, i.e,

$$\frac{\mathrm{d}^3\mathcal{N}_N}{\mathrm{d}E_\chi \mathrm{d}\cos\theta_\chi \mathrm{d}\phi_\chi} = \sum_i \int \mathrm{d}E^* \mathrm{d}\phi^* \mathrm{d}\cos\theta^* \int \mathrm{d}E \mathrm{d}\phi \mathrm{d}\cos\theta \frac{\mathrm{d}^3\sigma_i}{\mathrm{d}E \mathrm{d}\phi \mathrm{d}\cos\theta} \cdot \frac{\mathrm{d}^3\mathcal{N}_i}{\mathrm{d}E^* \mathrm{d}\phi^* \mathrm{d}\cos\theta^*} \cdot \delta(E_\chi - E')\delta(\cos\theta_\chi - \cos\theta')\delta(\phi_\chi - \phi'), \tag{3.2.1}$$

where E, ϕ, θ are, respectively, the parent energy, azimuthal angle and polar angle in the lab frame, the starred quantities describe the child in the parent's cms

frame, while the primed quantities are obtained by boosting the starred quantities by the Lorentz transformation associated with the unstarred ones. In practice, this integral cannot be done analytically, so we obtain the distribution by sampling the underlying σ, N distributions and explicitly performing the boosts. Furthermore, since the parent particles are focused predominantly along the beam axis, we have $\phi \simeq \phi'$, hence the ϕ integral is trivial.

Turning now to the absolute number of produced HNLs, this clearly depends on the normalisations of $\mathrm{d}^3\sigma_i$ and $\mathrm{d}^3 N_i$. In order to eliminate systematic errors in the extraction of these quantities, associated for instance with the particular model of proton-nucleon interactions in the beam dump, we instead calibrate this directly using the *measured* flux of active neutrinos. This was measured at BEBC [65], and is consistent with their dominant source being the three-body prompt decays of $D^{\pm}$ and D_0 mesons [100]. Hence the number of HNLs, $\mathcal{N}_\chi$, can be simply related to the number of ($\sim$massless) active neutrinos of species $\mathcal{N}_{\nu_\ell}$ via

$$\frac{\mathcal{N}_N}{\mathcal{N}_{\nu_\ell}} \simeq \frac{\sum_i \sigma(pN \to P_i + X)\mathrm{Br}(P_i \to N + Y)}{\sigma(pN \to D^+D^- + X)\mathrm{Br}(D^\pm \to \ell\nu_\ell + X) + \sigma(pN \to D^0\bar{D}^0 + X)\mathrm{Br}(D^0 \to \ell\nu_\ell + X)}, \tag{3.2.2}$$

where we sum over parent particle P_i that may produce HNLs in their decays. We take $4\sigma(pN \to D^+D^- + X) = 2\sigma(pN \to D^s + X) = \sigma(pN \to D^0\bar{D}^0 + X)$, so that all cross-sections in the denominator above are proportional to each other, in accordance with data from the Fermilab E769 experiment [101]. If all the production cross sections $\sigma(pN \to X)$ appearing in the numerator above are also proportional (to be justified when we precisely describe the P_i that appear in this equation), then the hadronic dependence drops out modulo the proportionality constants, thus simplifying the calculation considerably.

We have now reduced the problem to obtaining initial parent and final decay distributions, as well as branching ratios for certain reactions. These quantities depend on the specific production modes in question, which we will now delineate.

3.2.1 HNL production through decays

The particle decays that generate HNLs depends on which active neutrino it mixes with. For decays mediated by the neutral current, flavour is conserved (up to the $N - \nu_\ell$ mixing), and so the HNL appears in conjunction with an associated lepton. In particular, for mixing with ν_τ, if $m_N > m_\mathrm{P} - m_\tau$, then HNL production from decay of a parent of mass m_P is kinematically forbidden. We can now sort the production channels by those allowed with a non-zero $U_{\tau N}$, before moving on to the $U_{Ne} \neq 0$ case.

Mixing with ν_τ

HNLs above the kaon mass are not produced in the decays of any mesons containing just the lightest four quarks. In principle they may be produced in the decays of B mesons, but these were not produced at the energies of the 1982 CERN beam dump (400 GeV protons from the SPS). Hence the dominant contribution to HNLs above the kaon mass that mix solely with the tau neutrino is from tau lepton decay. The tau leptons are themselves produced in D meson decay, so we may apply Eq.(3.2.1) to determine the τ flux, which in turn determines the HNL flux from the subsequent decay.[1] Note that since the τ ultimately comes from a D meson, its production probability is proportional to the *same* hadronic cross-section, as was anticipated at the beginning of this section.

The D_s meson is the dominant source of τ leptons, which in turn decay to heavy HNLs. We thus need their differential distribution. This is usually parametrised as:

$$\frac{\mathrm{d}^2\sigma}{\mathrm{d}x_\mathrm{F}\mathrm{d}p_\mathrm{T}^2} \propto \mathrm{e}^{-bp_\mathrm{T}^2}(1 - |x_\mathrm{F}|)^n, \tag{3.2.3}$$

where $x_\mathrm{F} = 2p_L^\mathrm{CM}/\sqrt{s}$ is twice the longitudinal momentum in the cms frame (relative to the cms energy), p_T is the transverse momentum and the parameters b and n

[1] We make the simplification of averaging over the τ spin, so that the final decay is isotropic in its rest frame, as it is for the scalar mesons.

must be extracted from data. While b can be considered to be independent of both the cms energy and the quark content of the charmed meson [102], n may in general depend on both of these quantities. Due to lack of specific data, we approximate n for D_s production to be the same as for the other D_0, $D^{\pm}$ mesons. To parametrise the production in the WA66 experiment, we use the results from the WA82 experiment [103], since both experiments used the same target material (copper), as well as similar beam energies (370 GeV for WA82 cf. 400 GeV for WA66). We use $b = 0.93 \pm 0.09$ GeV^{-2} and $n = 6.0 \pm 0.3$ [103]. Somewhat different values for n were quoted by other experiments e.g. [104, 105], and in the review [106], but this is not as important for HNL production as the transverse momentum distribution which is set by b.

The tau meson has two main decay modes which result in an HNL, $\tau^{\pm} \to \pi^{\pm} N$ and $\tau \to \ell \nu_{\ell} N$. The former is a two body decay, whose decay distribution is determined simply by energy-momentum conservation, and has branching ratio [107]:

$$\begin{aligned} \mathrm{Br}(\tau \to \pi N) &= \mathrm{Br}(\tau \to \pi \nu_{\tau}) \cdot \sqrt{\lambda(y_{\pi}, y_N)} g(y_{\pi}, y_N) |U_{\tau N}|^2, \\ \lambda(x, y) &\equiv \frac{(1-x)^2 + (1-y)^2 - 2xy}{(1-x)^2}, \\ g(x, y) &\equiv \frac{(1-y)^2 - x(1+y)}{1-x}, \\ y_{\pi} &\equiv \left(\frac{m_{\pi}}{m_{\tau}}\right)^2, \quad y_N \equiv \left(\frac{m_N}{m_{\tau}}\right)^2; \end{aligned} \tag{3.2.4}$$

We use the values $m_{\pi} = 140\,\mathrm{MeV}$, $m_{\tau} = 1777\,\mathrm{MeV}$, and $\mathrm{Br}(\tau \to \pi \nu_{\tau}) = 0.108$.

By contrast, the distribution in a three-body decay depends on the mediating interaction, which in this case proceeds via the W boson. The angular distribution of the decays is dictated by the orientation of the τ polarisation, which is in turn set by the chiral structure of the weak interactions. However, we may average over this effect once we take into account the equal number of D_s and $\bar{D}_s$ which produce

the ensemble of polarised leptons. The decays are thus fully characterised by their energy distribution in the τ rest frame, which is approximated at low momentum transfer $q^2 \ll M_{\mathrm{W}}^2$ as [108, 109, 110]

$$\frac{d\Gamma}{dx} = \Gamma_0 x^2 \beta \left(3 - 2x + \frac{x}{4}(3x-4)(1-\beta^2)\right), \tag{3.2.5}$$

where $x = 2E_N/m_\tau$ is twice the energy fraction carried by the HNL, $\beta = \sqrt{1-(m_N/E_N)^2}$, and the normalisation Γ_0 is set by the observed active neutrino flux. The mass of the lepton pair has been neglected above but we keep explicit the dependence on the possibly sizeable HNL mass m_N. The energy fraction x may take values between $x_{\min} = 2m_N/m_\tau$ and $x_{\max} = 1 + (m_N/m_\tau)^2$. The normalisation is given by [111]

$$\begin{aligned} \mathrm{Br}(\tau \to \ell\nu_\ell N) &= \mathrm{Br}(\tau \to \ell\nu_\ell\tau) \cdot f(y_N)|U_{\tau N}|^2, \\ f(x) &= 1 - 8x + 8x^3 - x^4 - 12x^2 \log x. \end{aligned} \tag{3.2.6}$$

The above equations fully determine the hypothetical HNL flux in terms of the observed active neutrino flux. As previously stated, the total number of HNLs may be obtained by a simple rescaling of the number of (∼massless) neutrinos observed, while the differential distribution is obtained from a full Monte Carlo. The results of this are shown in Fig.3.1, where we display the angle of HNLs produced with respect to the beam axis against the energy of the HNL. Note that as expected the HNLs are highly focused along the beam axis, due to the large Lorentz factors of their parent particles.

Mixing with ν_e

HNLs that mix with electron (or muon) neutrinos are produced more readily in beam dumps, as the abundant heavy charmed mesons produce them in their decays. We consider only two-body decays, as these are the dominant source of massive HNLs, unlike ∼massless active neutrinos ν_ℓ that are subject to helicity suppression,

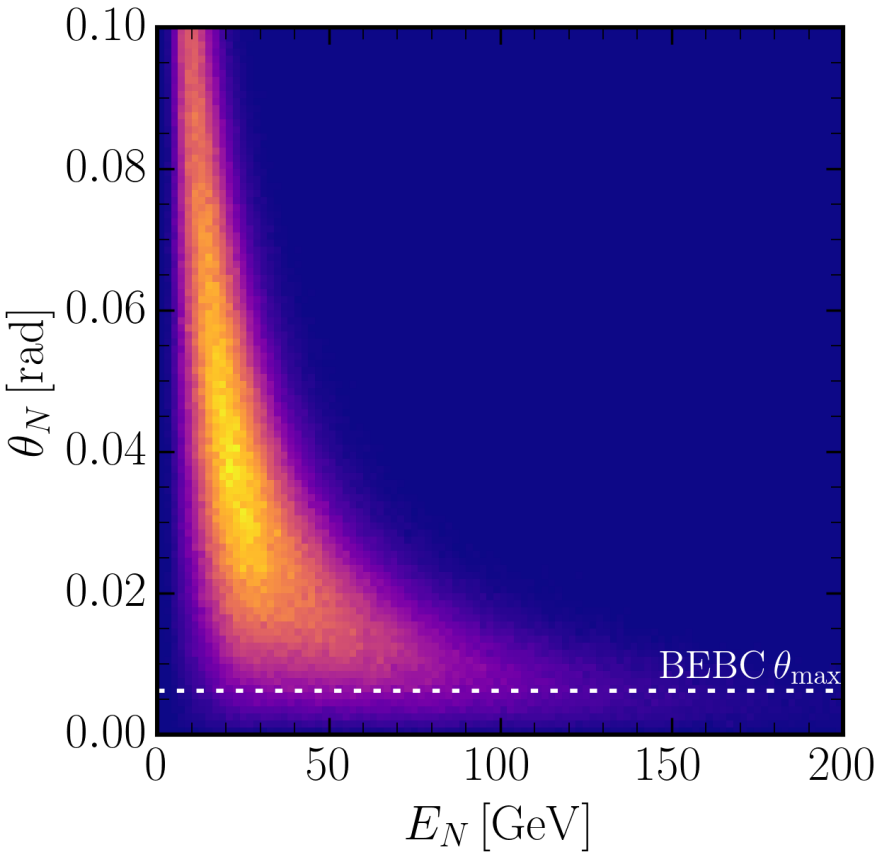

Figure 3.1: A 2D histogram of the distribution of HNL energy against angle with respect to the beam axis, for $m_N = 1$ GeV. We show results for HNLs that mix solely with ν_τs, so are produced solely from τ decays. The dashed horizontal line indicates the opening angle of the BEBC detector as seen from the production point in the beam dump.

e.g. [107, 112, 113]. The branching ratio for these processes is, in ratio to the corresponding SM branching ratio:

$$\begin{aligned} \mathcal{R} = \mathrm{Br}(D^\pm \to \ell N)/\mathrm{BR}(D^\pm \to \ell\nu_\ell) &= \lambda^{1/2}(x_\ell, x_N) h(x_\ell, x_N) |U_{\tau N}|^2, \\ \text{where,} \quad \lambda(x,y) &= \frac{(1-x)^2 + (1-y)^2 - 2xy}{(1-x)^2}, \\ h(x,y) &= \frac{x + y - (x-y)^2}{x(1-x)}, \\ x_\ell = \left(\frac{m_\ell}{m_D}\right)^2, &\quad x_N = \left(\frac{m_N}{m_D}\right)^2. \end{aligned} \tag{3.2.7}$$

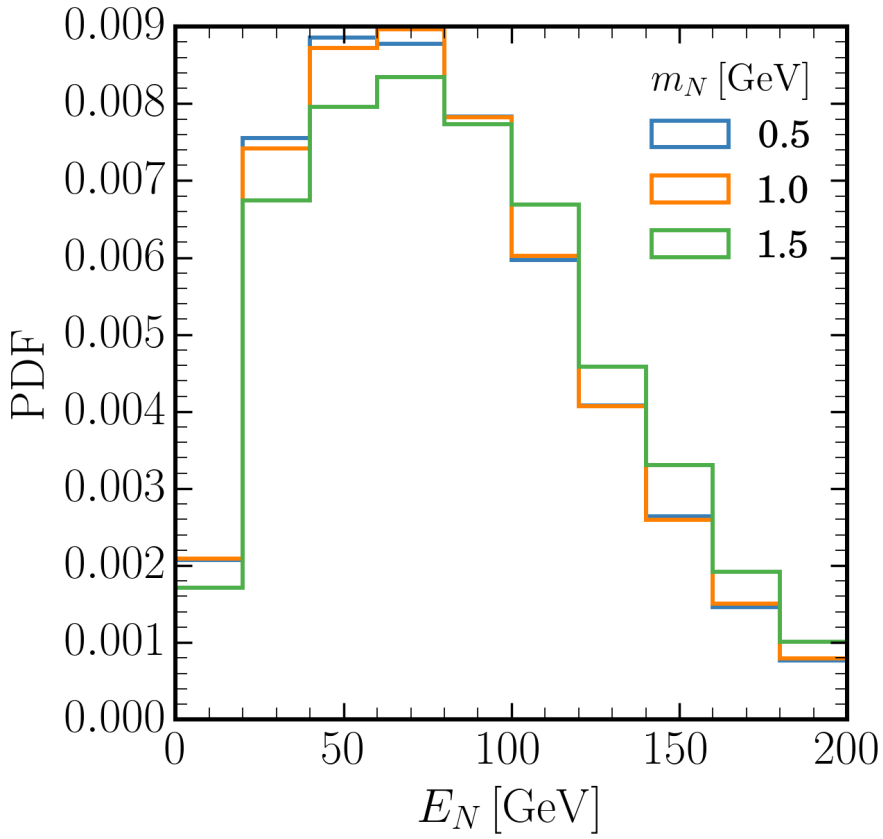

Figure 3.2: A histogram of the HNL energy distribution for those produced within the BEBC opening angle. Results are shown for three values of the HNL mass m_N to illustrate the insensitivity to the mass until it approaches the production threshold of m_τ.

The behaviour of the above ratio is shown in Fig.3.3. Since this is a two-body decay, the differential distributions are fully determined by conservation laws.

3.3 Heavy neutrino decay and detection

In order to be detected, the HNLs produced in the beam dump must reach the detector and then decay within it. The probability for the HNL to reach the detector depends on all the possible detection channels open to it, as well as the mediating interactions. For simplicity, we consider only SM particles in the final state, i.e. HNL decay via the known electroweak bosons. Our analysis is easily generalised to decays via other mediators, see e.g. [114, 81]. The probability P for an HNL to

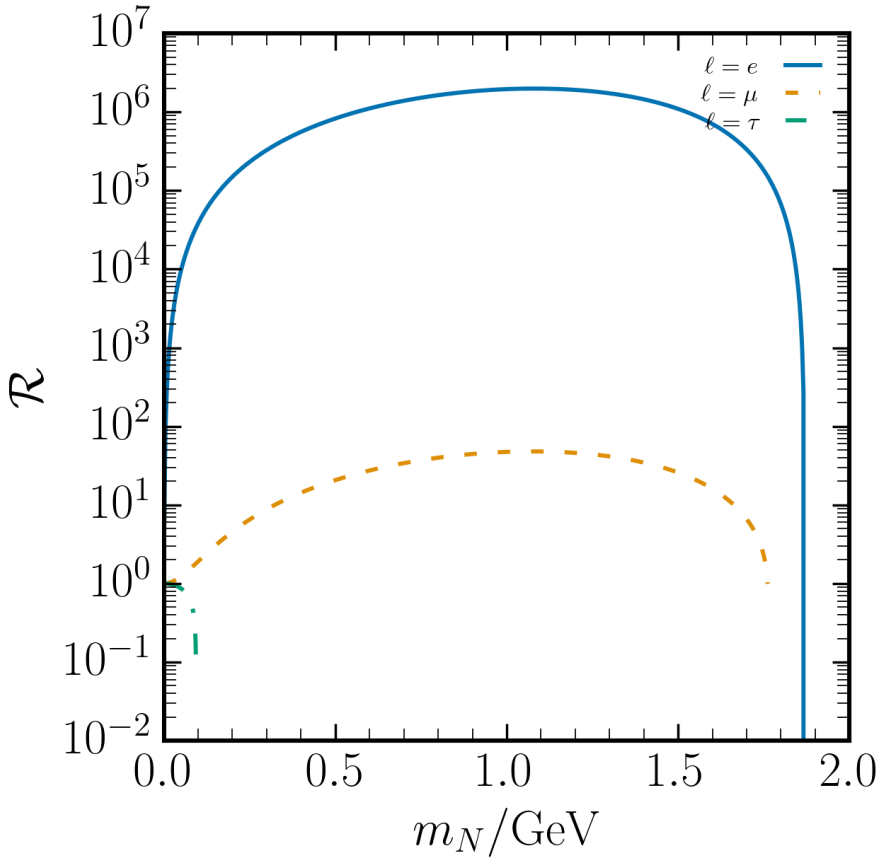

Figure 3.3: The enhancement of HNL production relative to massless neutrinos in two-body D meson decays (3.2.7). For HNLs mixing with the electron or muon neutrino, there is significant enhancement due to relaxation of the helicity suppression as the HNL mass increases. However for HNLs mixing with the τ the enhancement is negligible (and explains why no bound was quoted in the previous BEBC analysis [100]).

reach the detector at a distance L' from the target and then decay within the length $L \ll L'$ of the detector is:

$$P = \exp\left(-\frac{m_N L' \Gamma}{p_N}\right)\left[1 - \exp\left(-\frac{m_N L \Gamma}{p_N}\right)\right], \tag{3.3.1}$$

where p_N is the momentum of an HNL, and Γ is the *total* decay rate. In the small mixing regime, where $L' m_N \Gamma / p_N \ll 1$, we may linearise this to write

$$P \simeq 1.5 \times 10^{-8} \left(\frac{L}{1\,\mathrm{m}}\right) \cdot \left(\frac{100\,\mathrm{GeV}}{p_N}\right) \left(\frac{m_N}{1\,\mathrm{GeV}}\right)^6 \cdot \left(\frac{|U_{\tau N}|^2}{10^{-7}}\right), \tag{3.3.2}$$

to illustrate a benchmark decay rate for a purely leptonic electroweak decay. Note that the mixing angle factorises, simplifying the Monte-Carlo simulations substantially. In this small-mixing regime, we may place an upper bound on the size of the mixing angle; however, for larger mixings, we may only exclude a certain range by demanding that the HNLs decay *before* they can reach the detector.

The detection probability depends solely on the decay channels for which a search was carried out in BEBC, and is associated with an experimental efficiency ϵ. The number of observed events is related to the number of HNLs produced in the beam dump as

$$N = \mathcal{N}_N \Omega \langle P \rangle_\Omega \sum_\alpha \frac{\Gamma_\alpha}{\Gamma} \cdot \epsilon_\alpha, \tag{3.3.3}$$

where $\mathcal{N}_N$ is given by Eq.(3.2.2), Ω indicates the geometric acceptance set by the solid angle of the detector and $\langle \cdot \rangle_\Omega$ indicates that we average over HNLs that lie within this acceptance angle, while the sum is over experiment-specific channels.

The experimental cut efficiency ϵ is a combination of factors, which depends on both the detector response and the HNL decay channel. At BEBC, searches were made for $\ell^-\pi^+/\ell^+\pi^-$ and $\ell^-\ell^+\nu$ where $\ell = e, \mu$ [100]. HNL decay candidates were required to have a oppositely charged particle pair (with momentum > 1 GeV/c for scanning efficiency of 97%) and no associated neutral hadron interactions or neutral strange particle decays. Cuts were placed on the energy and angle with respect to the beam axis of the charged decay products to ensure consistency with the assumed production/decay channel.

On the theory side, one then needs a decay distribution as input to calculate the expected cut efficiency. In the three-body leptonic decays, the energy of the children fully specifies the relative orientation of the 3-momenta, so all that is required is the

differential distribution for the two energies E, E'. In the HNL rest frame, this is

$$\frac{\mathrm{d}^2\Gamma}{\mathrm{d}E\mathrm{d}E'} = \frac{G_F^2 m_N}{2\pi^3}\left[g_-^2 E(m_N - 2E) + g_+^2 E'(m_N - 2E') + 4m^2 g_- g_+\left(1 - \frac{E+E'}{m_N}\right)\right] \tag{3.3.4}$$

where $g_- = \sin^2\theta_\mathrm{W}$ and $g_+ = (\sin^2\theta_\mathrm{W} - \frac{1}{2})^2$, and we keep explicit finite mass corrections. This formula applies to all decays via the neutral current with massive final state particles and agrees with e.g. [115] who compute only the massless $m^2 \to 0$ limit. The hadronic decays, meanwhile, are two-body ($\not{p}_\mathrm{T} \equiv -p_\mathrm{T} = 0$), so the distribution is trivial.

Since the sensitivity to HNLs depends on the experimental cuts that were used to isolate signal events, we must take all of this into account (unlike in [94]) to extract bounds on the HNL mixing angles. In particular, we require that HNL events pass a cut on the invariant transverse mass M_T, defined by

$$M_\mathrm{T} \equiv (p_\mathrm{T}^2 + M_I^2)^{1/2} + p_\mathrm{T} < m_D - m_\mu. \tag{3.3.5}$$

We further adopt a lepton identification efficiency of 96%. This was the detection efficiency of the WA66 experiment for electron tracks of momentum > 0.8 GeV/c, while it was 97% for muons of momentum > 3 GeV/c [100]. (While the cuts used depended on the HNL under consideration, no specific results for mixing with ν_τs were given, hence we conservatively use the same cuts that were placed on HNLs mixing with ν_μs.)

There were no surviving candidates in WA66 for the HNL decay channels $ee\nu$, $e\mu\nu$ or $\mu\mu\nu$, or for $e\pi$, and there was only 1 candidate for $\mu^+\pi^-$ (with invariant mass ~ 1 GeV). The background was calculated using data from the WA59 experiment [116] in which BEBC, filled with a Ne/H_2 mix similar to WA66, was exposed to a conventional 'wide band' beam in which the fraction of HNLs would have been $< 1\%$ of that in the beam dump beam. The background was estimated to be 0.6 ± 0.2

Experiment	POT/10^{18}	$E_{\rm b}$/GeV	D/m	V/cm^3	Cuts	Observed events (Background)	η
BEBC [65, 100]	2.72	400	404	$357 \times 252 \times 185$	$E_{\rm T} > 1\,{\rm GeV}$ $\wedge M_{\rm T} < m_D - m_\mu$	1 (0.6±0.2)	0.96

Table 3.1: The relevant experimental parameters for the CERN-WA66 experiment. POT is the total number of protons on target,$E_{\rm b}$ is the energy of proton beam, D is the distance from the end of the target to the beginning of the detector and V is the detector volume written as transverse area $\times$ length; the dimensions of BEBC are given approximating the detector as a cuboid. Cuts are placed on the total energy of the charged pair $E_{\rm T}$ and on the transverse mass, as defined in Eq.(3.3.5). The number of observed events is given, as well as the expected background. The detection efficiency after cuts is denoted as η.

events [100] corresponding to an upper limit of 3.5 @ 90% CL on signal events.

3.3.1 Decay rates

We now evaluate the partial and total decay widths Γ_α and Γ which feature in Eq.(3.3.3). The HNL is taken to be a Majorana fermion. As with HNL production, the phenomenology depends strongly on the HNL mass and the mixing parameters. (For the mixing with ν_τ the total width is calculated below. For the mixing with ν_e there are additional contributions which we take from [111].

The total width is dominated by hadronic decays, once these are kinematically allowed as detailed in [111]. Below the QCD scale, the width is dominated by the decay to a neutral pion at a rate

$$\Gamma(N \to \nu_\alpha \pi^0) = \frac{G_F^2 f_\pi^2 m_N^3}{32\pi} |U_{\alpha N}|^2 \left(1 - x_{\pi N}\right)^2 , \tag{3.3.6}$$

with $x_{\pi N} \equiv (m_\pi/m_N)^2$. Above $\Lambda_{\rm QCD}$, there are significant contributions from multi-hadron final states, which we approximate by the decay width to quarks,

$$\Gamma(N \to \nu_\alpha f \bar{f}) = \frac{G_F^2 m_N^5}{192\pi^3} |U_N|^2 c_f, \tag{3.3.7}$$

where the constants are $c_u = 3(1 - \frac{8}{3}\sin^2\theta_{\rm W} + \frac{32}{9}\sin^4\theta_{\rm W})/4$ and $c_d = 3(1 - \frac{4}{3}\sin^2\theta_{\rm W} + \frac{8}{9}\sin^4\theta_{\rm W})/4$. We augment this with a QCD loop factor, which we take to be the

same as in the corresponding tau lepton decay [117].

The decay to a lepton pair is also described by Eq.(3.3.7) in the limit that the lepton pair is much lighter than the HNL. In this case, the coefficient c_f depends on whether there is a charged current contribution to the rate in addition to the neutral current contribution. In the case where there is only a neutral current contribution, $c_\ell = (1-4\sin^2\theta_{\rm W}+8\sin^4\theta_{\rm W})/4 \simeq 0.13$, while $c_\ell = (1+4\sin^2\theta_{\rm W}+8\sin^4\theta_{\rm W})/4 \simeq 0.57$ if both currents contribute [94]. The bounds quoted in [100] use $c_\ell = 1$, which corresponds to a charged current-only interaction.

3.4 Results and conclusions

The bound we extract on $U_{\tau N}$ is shown in Fig. 3.4. Remarkably BEBC WA66 still outperforms all other experiments, including the much bigger CHARM detector. However once the HNL mass exceeds m_τ, there are no limits from the old beam dump experiments where B mesons could not be produced. This will happen however at the proposed Forward Physics Facility at the high-luminosity LHC [85] which will be sensitive to heavier HNLs with mass up to 5–6 GeV.

For completeness, we also show results for U_{eN}, the mixing with the electron neutrino, in Fig. 3.5. These results may be considered as an update of the previous BEBC WA66 results [100], using a corrected formula for the HNL decay probabilities, an increased number of production channels, as well as more current parameters in the phenomenological fit of the D meson distribution which implies a more collimated meson beam. This results in a twofold improvement compared to the bounds previously obtained. We have verified that the above effects account for the shift by reproducing exactly the previous BEBC results.

We have demonstrated the continued capability of the BEBC detector to place world-leading bounds on hypothetical particles of interest. This reanalysis has taken into account production and decay channels of HNLs with non-zero ν_τ mixings

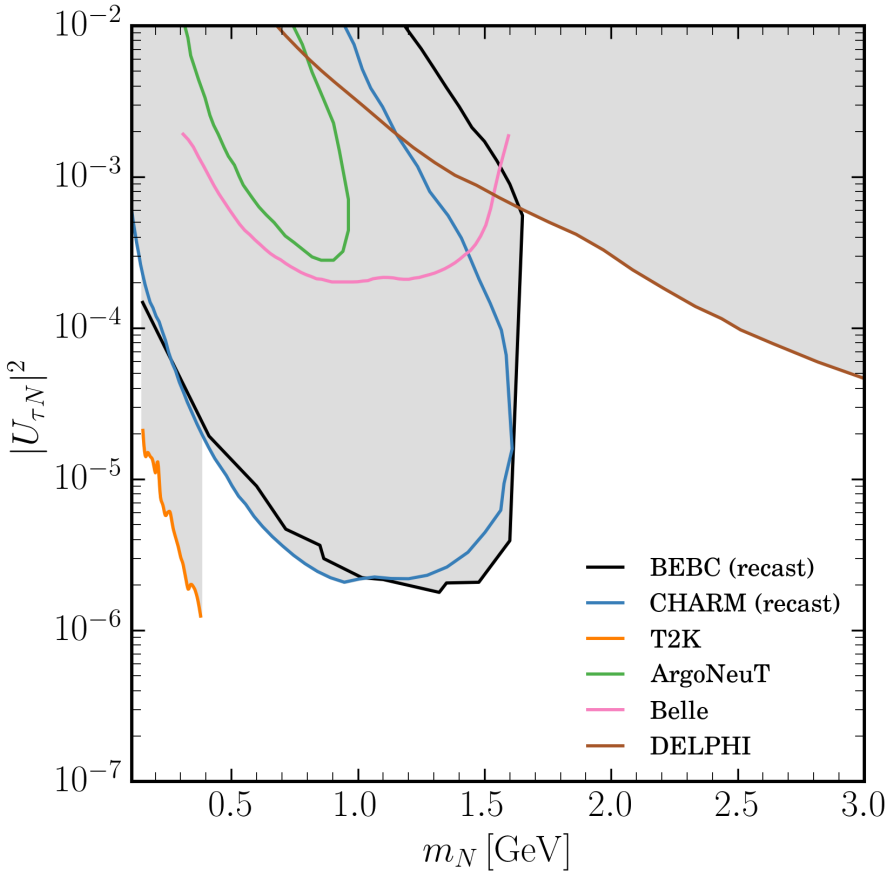

Figure 3.4: The 90% exclusion region in the HNL mass versus its mixing with ν_τ set by this reanalysis of BEBC WA66, compared to the recasting [94] of the CHARM bound. Also shown are bounds from T2K [86], ArgoNeuT [88], a recast of Belle [89, 91] and DELPHI [96].

that have not been much considered earlier, thus providing an up-to-date set of exclusions. It would be interesting to explore the sensitivity of BEBC to other models of HNLs, for instance those involving other mediators [114, 81], as we expect similar improvements may be had.

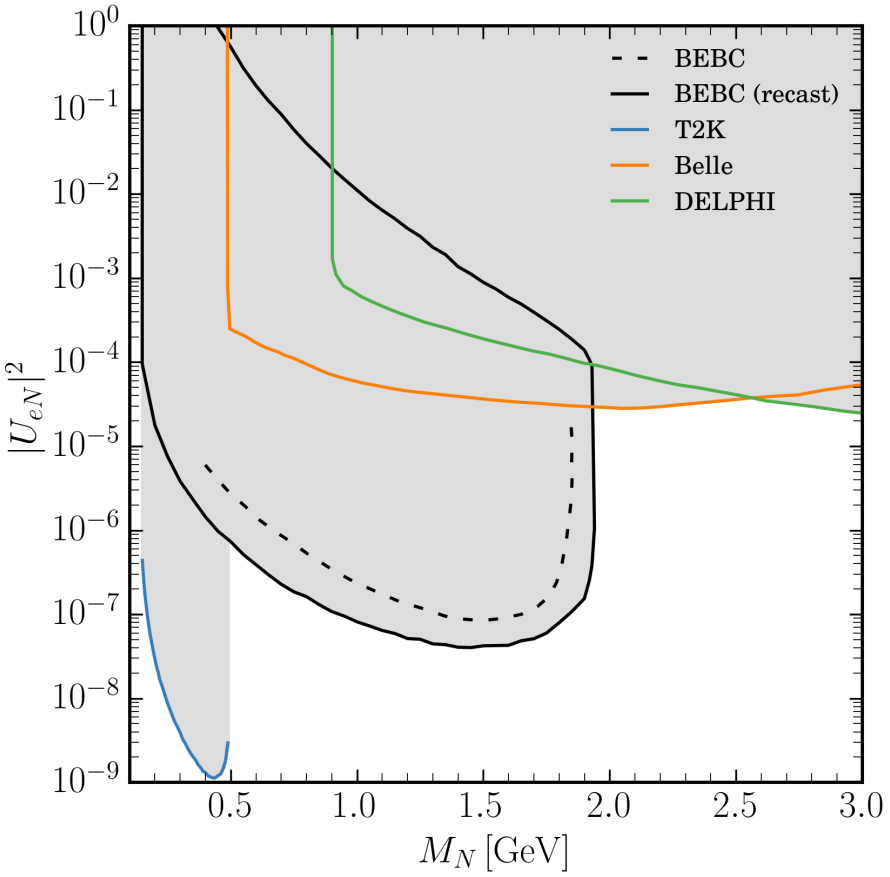

Figure 3.5: The 90% exclusion region in the HNL mass versus its mixing with ν_e set by this reanalysis of BEBC WA66, compared to the previously set bound [100]. Also shown are bounds from T2K [86], a recast of Belle [89, 91] and DELPHI [96].

Chapter 4

Dark photons, magnetic fields, and astrophysical plasmas

4.1 Introduction

There may exist a light gauge boson called the dark photon (DP) X_μ that kinetically mixes with our photon A_μ [118]. The Standard Moded field content is uncharged under the corresponding gauge group, making such a boson difficult to detect as it mediates no long-range force in the massless limit.

The defining Lagrangian of the DP may be written as

$$\begin{aligned}\mathcal{L} \supset & -\frac{1}{4}\left(F_{\mu\nu}F^{\mu\nu} + F'_{\mu\nu}F'^{\mu\nu}\right) \\ & + \tilde{e}J^\mu_{\mathrm{EM}}A_\mu + \frac{m^2}{2}\left(X^\mu X_\mu + 2\chi X^\mu A_\mu + \chi^2 A^\mu A_\mu\right),\end{aligned} \tag{4.1.1}$$

where $\chi \equiv \tan\alpha$ and $\tilde{e} \equiv e(1+\chi^2)^{1/2}$. The Lagrangian still possesses the $U(1)$ gauge invariance of electromagnetism, despite appearances, in contrast to the Proca Lagrangian. The mass matrix is singular, containing a zero eigenvalue as dictated by gauge invariance; the other eigenvalue, the mass of the DP, is $m_X^2 = (1+\chi^2)m^2$. The model parameter space is then simply spanned by $\{m_X, \epsilon\}$.

There exist many constraints on the DP parameter space, see, e.g., [119, 43]

for a review of these. For ultralight DPs (below around $10^{-10}\,\mathrm{eV}$), there are very strong constraints if the DP constitutes dark matter. If this is not the case, the bounds are weaker. A constraint comes from a Cavendish-type experiment [120] exploring deviations from Coulomb's law [121]. The lack of spectral distortions measured by COBE [122] in the CMB places cosmological constraints [123, 124]. Dark photons may also trigger a superradiant instability around spinning black holes [125, 126], although this may be quenched for sufficiently large kinetic mixing [127]. Observations of the magnetic fields around the Earth [128] also place limits [121, 129, 130]. Finally, Kloor et al. [130] claim that measurements of Jupiter's magnetosphere, as reported in [131], may bound dark photons at still lower masses.

We critically examine Kloor et al.'s recasting of the photon mass bound coming from Jupiter's magnetic field in terms of the DP model. We highlight the distinction between bounds that come from the observation of the forces on the plasma in a magnetosphere, and those that come from the the measured magnitude of the magnetic field ascribed to a dipole source. The former, in the particular case of Jupiter, has been used to place a robust bound on the mass of the photon [132], but does not constrain DPs, as we will show. Furthermore, the latter is not enough to place constraints without including the external (non-intrinsic) contributions to the Jovian magnetic field, which formerly were not taken into account.

The secure bound on the photon mass is derived from the non-observation of the effect of a massive photon on the plasma in the Jovian magnetosphere. As any photon mass increases, the size of the Lorentz force exerted by the magnetic field on a plasma increases, and at some point is in conflict with the observed flow. We derive the DP-altered magnetohydrodynamic (MHD) equations and show that no such effect occurs and hence no recasting of the photon mass bound is possible. We thus turn to measurements from the *Juno* mission [133] to obtain the size of any anomalous magnetic field that cannot be ascribed to the Jovian magnetosphere. This allows a reliable bound to be placed on very low mass DPs.

Incidentaly, we demonstrate that the most stringent bounds on the photon mass [134] from observations of the approximate equilibrium of the solar wind around Pluto [135, 136] do not constrain DPs either.

The layout of the paper is as follows. In section 4.2, we present the modified form of Maxwell's equations, as well as the MHD equations in the quasistatic limit. In section 4.3, we present the bounds coming from careful observation of the Earth's magnetic field. In section 4.4, we review the knowledge of Jupiter's magnetosphere that allows us to obtain an upper limit on the size of external magnetic fields around Jupiter, and thus to set a DP limit. In section 4.5, we solve the relevant MHD equations to show that the forces on plasmas in the magnetosphere are largely unaffected by any DP, and hence their behaviour cannot be used to constrain DPs. We show in section 4.6 that the same conclusions are reached regarding the observation of currents in the far heliosphere around Pluto. Finally, we conlude in section 4.7. Appendix 4.A contains a derivation of the magnetic field created by a point-like MDM when Maxwell's equations are modified by the inclusion of a DP.

4.2 DP-modifed Maxwell and MHD equations

In this section, we derive the equations governing the magnetic fields and currents within magnetospheres. In order to make contact with the common form of Maxwell's equations, we will work in non-relativistic notation. We write the regular electric and magnetic fields as $\mathbf{E}$ and $\mathbf{B}$, respectively, which may be written in terms of the scalar potential ϕ and vector potential $\mathbf{A}$ as

$$\mathbf{E} = -\nabla\phi - \partial_t \mathbf{A}, \tag{4.2.1a}$$

$$\mathbf{B} = \nabla \times \mathbf{A}. \tag{4.2.1b}$$

Similarly, we write the *dark* electric and magnetic fields as $\boldsymbol{\eta}$ and $\boldsymbol{\beta}$, respectively. These are given in terms of their potentials as

$$\boldsymbol{\eta} = -\nabla\psi - \partial_t \mathbf{X}, \tag{4.2.2a}$$

$$\boldsymbol{\beta} = \nabla \times \mathbf{X}. \tag{4.2.2b}$$

From the Lagrangian (4.1.1), we may derive the dark photon-modified Maxwell's equations

$$\nabla \cdot \mathbf{E} + \chi^2 m^2 \phi = \tilde{e}\rho + \chi m^2 \psi, \tag{4.2.3a}$$

$$\nabla \times \mathbf{B} + \chi^2 m^2 \mathbf{A} = \tilde{e}\mathbf{J} + \partial_t \mathbf{E} + \chi m^2 \mathbf{X}, \tag{4.2.3b}$$

$$\nabla \times \mathbf{E} = -\partial_t \mathbf{B}, \tag{4.2.3c}$$

$$\nabla \cdot \mathbf{B} = 0. \tag{4.2.3d}$$

Here, ρ is the charge density and $\mathbf{J}$ is the charge current, both in units of $\tilde{e}$. Note that the homogeneous equations remain unchanged compared to the case with no dark photon. The dark photon also satisfies its set of Dark Maxwell's equations

$$\nabla \cdot \boldsymbol{\eta} + m^2 \psi = \chi m^2 \phi \tag{4.2.4a}$$

$$\nabla \times \boldsymbol{\beta} + m^2 \mathbf{X} = \partial_t \boldsymbol{\eta} + \chi m^2 \mathbf{A} \tag{4.2.4b}$$

$$\nabla \times \boldsymbol{\eta} = -\partial_t \boldsymbol{\beta} \tag{4.2.4c}$$

$$\nabla \cdot \boldsymbol{\beta} = 0. \tag{4.2.4d}$$

Additionally, the Lorentz force law is modified by a renormalisation of the electric charge [128] along with additions due to the dark fields, so we may write

$$\mathbf{F} = \tilde{e}\left(\mathbf{E} + \chi\boldsymbol{\eta} + \mathbf{v} \times (\mathbf{B} + \chi\boldsymbol{\beta})\right), \tag{4.2.5}$$

where $\mathbf{v}$ is the velocity of a charged particle.

To obtain a closed set of equations, we must further obtain the equations of motion for the plasma. The modification of the Lorentz force law leads to the same equations of kinetic plasma theory, with $e \to \tilde{e}$, $\mathbf{E} \to \mathbf{E} + \chi\boldsymbol{\eta}$ and $\mathbf{B} \to \mathbf{B} + \chi\boldsymbol{\beta}$. Thus, Ohm's law is

$$\frac{\tilde{e}}{\sigma}\mathbf{J} = \mathbf{E} + \chi\boldsymbol{\eta} + \mathbf{v} \times (\mathbf{B} + \chi\boldsymbol{\beta}), \tag{4.2.6}$$

where σ is the plasma conductivity. For plasmas in the solar system, we may take the large σ limit; we further take the quasistatic limit to find the set of MHD equations that we will use:

$$(-\nabla^2 + \chi^2 m^2)\mathbf{B} = \tilde{e}\nabla \times \mathbf{J} + \chi m^2 \boldsymbol{\beta}, \tag{4.2.7a}$$

$$\nabla \times \mathbf{E} = -\partial_t \mathbf{B}, \tag{4.2.7b}$$

$$\mathbf{E} + \chi\boldsymbol{\eta} + \mathbf{v} \times (\mathbf{B} + \chi\boldsymbol{\beta}) = 0, \tag{4.2.7c}$$

$$(-\nabla^2 + m^2)\boldsymbol{\beta} = \chi m^2 \mathbf{B}, \tag{4.2.7d}$$

$$\nabla \times \boldsymbol{\eta} = -\partial_t \boldsymbol{\beta}, \tag{4.2.7e}$$

$$\partial_t \rho + \nabla \cdot (\rho \mathbf{v}) = 0, \tag{4.2.7f}$$

$$\rho \frac{d\mathbf{v}}{t} = -\nabla P + \tilde{e}\mathbf{J} \times \mathbf{B}. \tag{4.2.7g}$$

Here P is the fluid pressure, $\mathbf{v}$ the fluid velocity, $\mathbf{J}$ is still the current density in units of $\tilde{e}$, but we have *switched notation* and ρ is now the fluid density as the charge density does not appear any longer.

4.3 Earth's magnetic field

The sources of magnetic fields around the Earth are well enough known that bounds have been set on the photon's mass from measurements of the magnetic field caused by the magnetic dipole moment of the Earth [137, 129]. These bounds are based on

the technique of Schrödinger [138]. As the process for bounding dark photons will be similar, let us briefly recapitulate the logic of the massive photon case.

If the photon has a mass μ, the magnetic field caused by a dipole $\mathbf{D} = D\hat{z}$ is

$$\mathbf{B}(\mathbf{x}) = \frac{De^{-\mu r}}{4\pi r^3}\Big[\left(1+\mu r+\frac{1}{3}(\mu r)^2\right)\left(3(\hat{\mathbf{z}}\cdot\hat{\mathbf{x}})\hat{\mathbf{x}}-\hat{\mathbf{z}}\right)-\frac{2}{3}(\mu r)^2\hat{\mathbf{z}}\Big]. \tag{4.3.1}$$

At a constant radius, the terms in the first bracket of this equation simply effect a rescaling of the magnetic field compared to the massless case. The last term is a new effect though, and from the point of view of massless magnetostatics it appears like an external field antiparallel to the dipole direction. The ratio S_μ of the external field caused by the mass of the photon to the equatorial field strength is

$$S_\mu = \frac{2}{3}\frac{(\mu R)^2}{1+\mu R+(\mu R)^2/3}, \tag{4.3.2}$$

where the measurement is taken at a radius R.

There are a number of true external fields B_{ext} from currents in the magnetosphere, such as those caused by the deflection of the solar wind off Earth's magnetic field, which are known due to satellite measurements. Having measured the currents in the magnetosphere, the magnetic field at the Earth's surface is extrapolated; this is done assuming no modifications to Maxwell theory, giving $B^{(0)}_{\text{ext}}$, which is consistent since the ratio of the external fields to the dipolar field B_{dip} is small. This is then subtracted from the measured non-dipolar magnetic field B_{meas}. Explicitly, we must satisfy the inequality

$$\begin{aligned} S_\mu &\lesssim \epsilon\frac{B_{\text{meas}}-B_{\text{ext}}}{B_{\text{dip}}} \\ &\simeq \epsilon\frac{B_{\text{meas}}-B^{(0)}_{\text{ext}}-\epsilon\chi^2 B^{(2)}_{\text{ext}}}{B_{\text{dip}}} \\ &\simeq \epsilon\frac{B_{\text{meas}}-B^{(0)}_{\text{ext}}}{B_{\text{dip}}}, \end{aligned} \tag{4.3.3}$$

where we have introduced a formal counting parameter ϵ to indicate the small ratio, and the correction to the calculation of the external fields $\chi^2 B_{\rm ext}^{(2)}$ contains an extra factor ϵ since S_μ is itself $\mathcal{O}(\chi^2)$.

Subtracting off these contributions leaves a bound on S_μ, which translates into a bound on the photon mass $\mu \lesssim 8 \times 10^{-16}\,\text{eV}$ [129]. It is worth emphasising that the true external fields must be known to obtain a bound from this method. This is true of the Earth; it was not true of Jupiter at the time of early analyses that have been used in the literature, as stated in [132].

The case of a dark photon follows in the same way, as analysed in [121, 129] (see Appendix 4.A for an alternate derivation of the field to all orders in χ). The resulting ratio S of the new external field to the field strength at the equator is

$$S = \frac{2}{3}\frac{(\chi m_X R)^2 e^{-m_X R}(1+\chi^2)}{1+\chi^2 e^{-m_X R}\left(1+m_X R+\frac{1}{3}(m_X R)^2\right)}. \tag{4.3.4}$$

The above ratio is bounded by $S \leq 3.9 \times 10^{-4}$ at a distance $R = 6.38 \times 10^6\,\text{m} = 3.24 \times 10^{13}\,\text{eV}^{-1}$ [129]. The bounds that result are an order of magnitude more constraining than any other terrestrial experiment, and extend lower in mass than even those from COBE.

The limit that we reviewed here relies on the knowledge of the magnetic fields that arise from sources external to the Earth's magnetic dipole. Without this, it is impossible to ascribe any anomalous magnetic field to the presence of a dark photon, or equivalently a photon mass, rather than an unaccounted Standard Model process.

4.4 Jupiter's magnetic field

A number of missions have measured the magnetic field of Jupiter. *Pioneer 10* took data in 1973 [140], and a year later the *Pioneer 11* magnetometer [141] obtained the most accurate measurement of the intrinsic, "internal" Jovian dipole [142] until

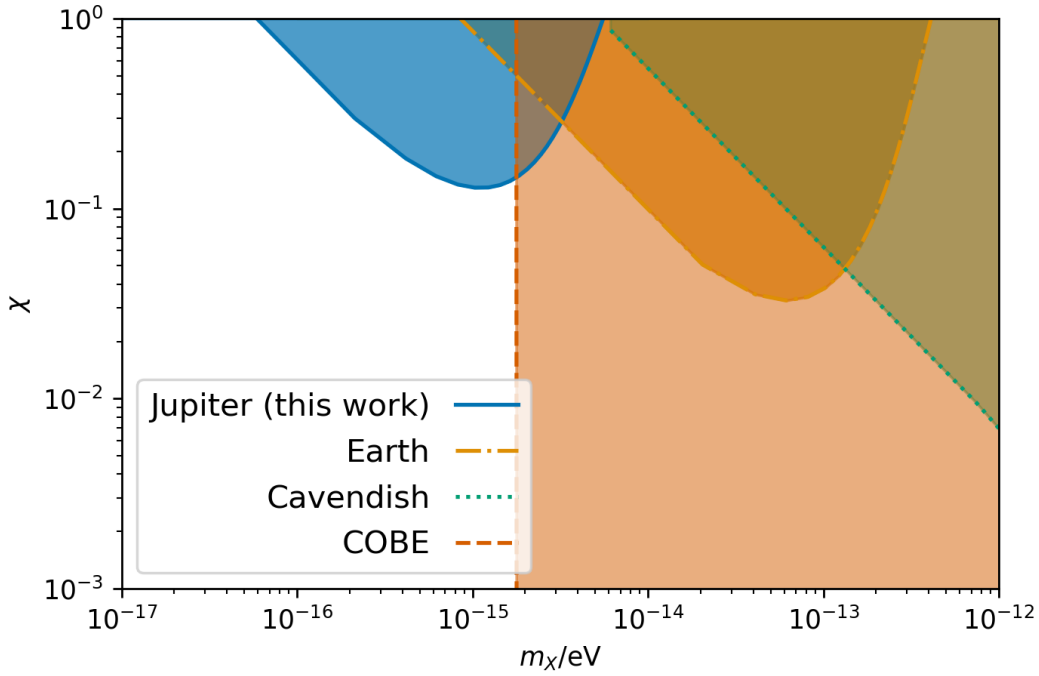

Figure 4.1: Constraints on the dark photon parameter space. The existing constraints shown are: Earth, from the lack of anomalous external magnetic fields [129]; Cavendish, coming from the accuracy of Coulomb's law[121]; COBE, from a lack of spectral distortions in the CMB [123, 124]. The constraints we place from the size of any unaccounted external magnetic fields on Jupiter [139] are labelled as Jupiter (this work).

the *Juno* mission [143]. The value obtained by the latter for the size of the dipole moment is $4.170\,R_J\,\mathrm{G}$, where $R_J = 71\,492\,\mathrm{km}$ is the radius of Jupiter. The currents in the Jovian magnetosphere cause "external" magnetic fields of order 100 nT, and so at distances of order 10 R_J the internal and external magnetic fields become comparable. Hence, in order to see any deviation from the predicted form of a MDM-sourced magnetic field at such radii, detailed knowledge of the external fields is required.

Voyager 1 measured not only the magnetic field around Jupiter [144], but critically also the currents and particles in its magnetosphere [145, 146, 147]. *Voyager 2* obtained similar results for the field strength [148] and the magnetosphere's contents [149, 150, 151]. By fitting an empirical model [152] to the magnetic field observed

by *Juno*, the Jovian magnetosphere was shown to contain a large current sheet near the equatorial plane extending out from around 8 R_J [139]. Using only *Pioneer 10* data taken at radii of around 10 R_J, as done in [130], it is impossible to set a reliable bound, as one must account for the external distortion of the magnetic field produced by the internal Jovian dynamo.

Data from the *Juno* magnetometer [153] was analysed by Connerney et al. [139] to find the impact of the Jovian magnetodisc on the magnetic field. The resulting upper bound on the size of any unaccounted for external field, projected along the direction of the dipole and at a distance $R = 5R_J = 1.8 \times 10^{15}\,\mathrm{eV}^{-1}$, is 10 nT. In the absence of error bars in Connerney et al.'s analysis, we choose to double the size of this field to obtain a more conservative bound. The size of the intrinsic dipole at this radius is also needed, for which we use the analysis of [143] to obtain a value of 3×10^3 nT. We thus bound the ratio (4.3.4) as $S \lesssim 6 \times 10^{-3}$, as compared to 10^{-1} used in [130]. The resulting limits are shown in Fig. 4.1.

One may worry that an empirical fit of the external magnetic field is not sufficient to extract a bound. To understand why, let us review how this analysis works. Such a fit proceeds in two stages. First, the coefficients of the multipole moments of the internal field are measured by fitting the magnetic field close to Jupiter's surface, where external fields are highly subdominant[1]. Then, using this internal model, the field at larger distances is fit to a particular magnetodisc model. In doing this fit, the effect of a DP may erroneously be included into the magnetodisc parameters if there is a degeneracy. If the time-variation of the magnetic field at fixed locations were available (as is the case on Earth, for example), then one could hope to isolate the time-independent effect of a DP from the external sources. However, since this is not the case, the external magnetic field ought to be determined from direct measurements of the plasma environment surrounding Jupiter. Models

[1]This analysis in fact shows that Jupiter is not well described as a dipole source, and the effect of higher order moments is significant, which also must be subtracted off.

of the magnetosphere's charged particle distribution derived from the above fit in fact show consistency with the data measured by *Voyager* 1 & 2 to within a factor of two [154], lending support to the conservative bound we have placed. A *Juno* era consistency check would further support such a conclusion.

4.5 MHD around Jupiter

The magnetic fields around Jupiter were analysed to obtain a bound on the photon mass $\mu \leq 6 \times 10^{-16}\,\text{eV}$ [132], even without detailed knowledge of the surrounding currents. The procedure used to get this bound is different to that of the previous section, as emphasised in [155]. Let us briefly review how this was done.

For a massive photon, Ampère's law is modified so that a dipolar magnetic field rescales the azimuthal current by a factor $1 + (\mu r)^2$ compared to the case of a massless photon [134]. Hence the force $\mathbf{F} = \mathbf{J} \times \mathbf{B}$ exerted on the plasma also increases by the same factor. Thus if the photon mass is too large, there can be no other balancing forces to achieve the observed equilibrium, and so such a scenario may be ruled out. This modified relation between currents and the magnetic field is the source of the above limit. Note that the obtained bound on the photon mass is much lower than the plasma frequency $\omega_p \simeq 5 \times 10^{-11}\,\text{eV}$, since it plays no role here[2].

How does a dark photon modify the currents in Jupiter's magnetic field? We follow Ryutov [134] and use a purely kinematic model for the standard electromagnetic interactions. We consider a situation in which the magnetic field on some surface of radius r_0 is known to be a dipole, so that we may write

$$\mathbf{B} = B_0 \cos\theta \hat{r}. \tag{4.5.1}$$

[2]The plasma frequency is obtained as the long-wavelength cut-off for high frequency electromagnetic modes $\omega \gg k v_{\text{th}}$, where v_{th} is the thermal velocity of the ions in the plasma, and is thus an irrelevant quantity for the system with negligible displacement currents considered here (as they are, for instance, when considering Alfvén waves in a magnetised plasma, which are *gapless*.)

on this surface. Then, as we move away, the vanishing divergence of $\mathbf{B}$ implies

$$\mathbf{B} = B_0 r_0^2 \frac{\cos\theta}{\mathbf{r}^2}\hat{r}. \tag{4.5.2}$$

We now would like to solve equation (4.2.7d) to find the dark magnetic field in the presence of such a source. The particular solution to this equation may be written in Cartesian co-ordinates as

$$\boldsymbol{\beta}(\mathbf{x}) = \frac{\chi m^2}{4\pi}\int d^3\tilde{\mathbf{x}}\frac{e^{-m|\tilde{\mathbf{x}}|}}{|\tilde{\mathbf{x}}|}\mathbf{B}(\mathbf{x}+\tilde{\mathbf{x}}). \tag{4.5.3}$$

We will solve the integral perturbatively in two different limits. As in the case of a massive photon, we ignore the homogeneous solution as unlike in regular magnetostatics there is no spatially homogeneous solution, and we are just left with unphysical exponential solutions.

4.5.1 Large mass limit

We first proceed in the limit $|\mathbf{x}|m \gg 1$. The strategy is to now expand $\mathbf{B}(\mathbf{x}+\tilde{\mathbf{x}})$ around the point $\mathbf{x}$ and then evaluate the integral (4.5.3). The exponential damping factor will tame the divergent pieces in the Taylor series of $\mathbf{B}$ as long as we are in the specified limit. The result is

$$\boldsymbol{\beta}(\mathbf{x}) = \chi B_0 r_0^2\left(\boldsymbol{\beta}(\mathbf{x})^{(0)} + \frac{\boldsymbol{\beta}(\mathbf{x})^{(2)}}{(mr)^2} + \frac{\boldsymbol{\beta}(\mathbf{x})^{(4)}}{(mr)^4} + \dots\right), \tag{4.5.4}$$

where

$$\begin{aligned}
\boldsymbol{\beta}(\mathbf{x})^{(0)} &= \frac{\cos\theta}{r^2}\hat{r},\\
\boldsymbol{\beta}(\mathbf{x})^{(2)} &= -2\left(\frac{\cos\theta}{r^2}\hat{r} + \frac{\sin\theta}{r^2}\hat{\theta}\right),\\
\boldsymbol{\beta}(\mathbf{x})^{(4)} &= -8\left(\frac{\cos\theta}{r^2}\hat{r} + 2\frac{\sin\theta}{r^2}\hat{\theta}\right).
\end{aligned} \tag{4.5.5}$$

In order to find how this dark magnetic field affects the charge current, we plug the result (4.5.4) into (4.2.7a). Note that the zeroth order piece in (4.5.4) cancels what looks like a photon mass term in (4.2.7a). This means that the only effect of a dark magnetic field is higher order in mr than one would expect from a naive comparison between the Proca Lagrangian and the Lagrangian we consider. This may be seen explicitly in the solution for $\mathbf{J}$ which is

$$\mathbf{J} = B_0 r_0^2 \frac{\sin\theta}{r^2}\left(1 + \chi^2 + \frac{4\chi^2}{(mr)^2} + \dots\right). \tag{4.5.6}$$

If the change in the current, and thus the force $\mathbf{F} = \mathbf{J} \times (\mathbf{B} + \chi\boldsymbol{\beta})$, induced by the dark magnetic field were to have a noticeable effect, we must have at least $\chi > 1$, since this result only holds if $mr \gg 1$. However, $\chi > 1$ is outside of the realm of applicability of the tree-level model of dark photon electromagnetism that we consider, and so no consistent constraints can be obtained.

4.5.2 Small mass limit

Let us now work in the other limit where the characteristic scale of observation R is much less than the Compton wavelength of the dark photon $mR \ll 1$. The solution to (4.2.7d) may then be approximated as

$$\boldsymbol{\beta} \simeq \chi(mR)^2\mathbf{B}, \tag{4.5.7}$$

and so to leading order in mR (4.2.7a) is just

$$(-\nabla^2 + \chi^2 m^2)\mathbf{B} = \tilde{e}\nabla \times \mathbf{J} + \dots, \tag{4.5.8}$$

which is of the same form as that arising from the Proca Lagrangian with a photon mass $\mu = \chi m$. We may thus recycle the known results to show that the force exerted

on the plasma by the current is

$$\tilde{e}\mathbf{J}\times\mathbf{B}=\frac{B_0^2r_0^2\sin\theta\cos\theta}{4\pi r^5}\left(1+(\chi mR)^2+\ldots\right). \tag{4.5.9}$$

This would be incompatible with observations if the extra term in brackets were somewhat larger than one; in the limit $mR\ll 1$, this requires a χ larger than one, which is again outside of the scope of classical physics. No bound can be placed on dark photons from current forces around Jupiter in this limit of the dark photon mass.

If instead $mR\sim 1$, we are in neither of the previous limits. However, there is then no large parameter that may appear that could cause large deviations in the currents, precluding such a limit. Thus, have now shown that the observation of a steady state in the neighbourhood of Jupiter places no consistent constraint on the dark photon coupling, in contrast to the case of a massive photon.

4.6 MHD in the far heliosphere

The strongest reliable constraint on the photon mass $\mu\lesssim 10\times 10^{-18}\,\mathrm{eV}$ comes from consideration of the solar wind in the far heliosphere [134]. Can one derive a constraint on dark photons in a similar manner?

The starting point is the model of solar winds first put forward by Parker [156]. The components of the magnetic field when we no longer neglect the azimuthal component of the magnetic field that comes from the Sun's rotation, as is necessary at large distances $r\gg r_0$, are given by

$$\begin{aligned}B_r&=B_0r_0^2\frac{\cos\theta}{r^2},\\ B_\theta&=0,\\ B_\phi&=B_0r_0^2\frac{\omega}{v_m}(r-r_0)\frac{\sin\theta}{r^2},\end{aligned} \tag{4.6.1}$$

where ω is the angular velocity of the sun and v_m is the outward velocity of the solar wind. In the far heliosphere, the magnetic field is almost purely azimuthal. We now follow the same procedure as section 4.5 to see what effect there is on the current.

4.6.1 Large mass limit

Carrying out the same expansion as in section 4.5.1, we write

$$\boldsymbol{\beta}(\mathbf{x}) = \boldsymbol{\beta}(\mathbf{x})^{(0)} + \frac{\boldsymbol{\beta}(\mathbf{x})^{(2)}}{(mr)^2} + \dots, \tag{4.6.2}$$

and solve (4.2.7d) perturbatively to find

$$\begin{aligned} \boldsymbol{\beta}(\mathbf{x})^{(0)} &= \chi\mathbf{B}, \\ \boldsymbol{\beta}(\mathbf{x})^{(2)} &= -2\chi\mathbf{B}. \end{aligned} \tag{4.6.3}$$

Thus (4.2.7a) gives

$$\tilde{e}\nabla \times \mathbf{J} = \frac{2\mathbf{B}}{r^2}(1 + \chi^2 + \dots), \tag{4.6.4}$$

which implies that $\mathbf{J}$ has r- and θ-components of rough size

$$J \sim \frac{B_\phi}{r}(1+\chi^2)^{1/2}, \tag{4.6.5}$$

with an associated force causing equatorial compression and radial deceleration of magnitude

$$F \sim \frac{B_\phi^2}{r}(1+\chi^2)^{1/2}. \tag{4.6.6}$$

If this force were bigger than the force $\rho v^2/r$, then the velocity would not be radial and constant, as is observed. We thus need $F < \sigma\rho v^2/r$ where σ is some fudge factor to account for our crudeness; this is the same limit used by [134] to derive a limit on the photon mass. Translating this into dark photon parameters, we find

the constraint

$$1 + \chi^2 \lesssim 10^{3/2}; \tag{4.6.7}$$

the bound is trivially satisfied for any perturbative coupling.

4.6.2 Small mass limit

As in section 4.5.2, to leading order in the small mass limit, we again have

$$(-\nabla^2 + \chi^2 m^2)\mathbf{B} = \tilde{e}\nabla \times \mathbf{J} + \dots. \tag{4.6.8}$$

This is solved by

$$\tilde{e}\mathbf{J} = 2\frac{B_\phi}{r}\left(1 + (\chi m r)^2\right)\hat{r}, \tag{4.6.9}$$

and again we see the dark photon correction is always negligible.

4.7 Conclusions

The magnetic field produced by a MDM receives noticeable corrections when the photon has kinetic mixing with a massive DP. Using this fact and knowledge about the true external fields, we placed constraints on dark photons whose Compton wavelength is of the order of the size of the Jupiter. These bounds extend further down in DP mass than any other (apart from those that make assumptions about the nature of dark matter). Specifically, we have $\chi \lesssim 10^{-1}$ for $m_X \sim 10^{-15}\,\text{eV}$. This made use of a fit of the magnetic field to an empirical model of the Jovian magnetodisc. This bound could be made more compelling by checking for good consistency between this model and the direct measurements of the surrounding plasma with forthcoming *Juno* data. A full comparison of the functional form of the magnetic field around Jupiter with that predicted by Maxwell theory – taking into account the effect of the surrounding plasma – would likely give stronger bounds,

but is beyond the scope of this work.

We have shown that bounds on the photon mass coming from the observation of current flow patterns in astrophysical magnetospheres do not constrain DPs, in contrast to massive photons. For large DP masses, where one might hope to have some effect, the leading order terms cancel once one consistently solves the relevant MHD equations. DPs with small masses fare no better, causing no significant alteration of the force felt by the plasma.

4.A The magnetic field from a magnetic dipole moment

We would like to calculate the magnetic field arising from a point magnetic dipole moment, in analogy with (4.3.1). The relevant equations we need to solve are

$$(-\nabla^2 + \chi^2 m^2)\mathbf{A} = \tilde{e}\mathbf{J} + \chi m^2 \mathbf{X}, \tag{4.A.1a}$$

$$(-\nabla^2 + m^2)\mathbf{X} = \chi m^2 \mathbf{A}, \tag{4.A.1b}$$

where we work here in Coulomb gauge $\nabla\cdot\mathbf{A} = 0$ and note that in the quasistatic limit this also implies $\nabla \cdot \mathbf{X} = 0$. Upon Fourier transforming (4.A.1), these differential equations become algebraic and we may solve for the vector potential to find

$$\mathbf{A}(x) = \tilde{e} \int \frac{d^3\mathbf{k}}{(2\pi)^3} \frac{\tilde{\mathbf{J}}(\mathbf{k}) e^{i\mathbf{k}\cdot\mathbf{x}}}{k^2 + \chi^2 m^2 \frac{k^2}{k^2+m^2}}, \tag{4.A.2}$$

where $\tilde{\mathbf{J}}(\mathbf{k})$ is the Fourier transform of $\tilde{e}\mathbf{J}(\mathbf{x})$. Approximating the magnetic dipole as coming form a point-like source at the origin, we have $\mathbf{J}(\mathbf{x}) = -\mathbf{D}\times\nabla\delta(\mathbf{x})$, where $\mathbf{D} = D\hat{z}$ is the magnetic dipole moment. We then have $\tilde{\mathbf{J}} = -i\mathbf{D}\times\mathbf{k}$.

We now need to evaluate integrals of the form

$$\mathbf{I} = \int \frac{d^3\mathbf{k}}{(2\pi)^3} \frac{\mathbf{k} e^{i\mathbf{k}\cdot\mathbf{x}}}{k^2 + \chi^2 m^2 \frac{k^2}{k^2+m^2}}, \tag{4.A.3}$$

which is most readily done in spherical co-ordinates. If we rotate our axes so that the polar axis of the momentum integral aligns with $\hat{\mathbf{x}}$, we see that the $x-$ and y-components have vanishing azimuthal angle ϕ integrals. The polar integral needed is found to be

$$\int_0^\pi d\theta\, e^{ikr\cos\theta} \cos\theta \sin\theta = 2i \frac{-kr\cos(kr) + \sin(kr)}{(kr)^2}. \tag{4.A.4a}$$

After integrating ϕ from 0 to 2π, we may extend the remaining even integral over the whole real axis and evaluate it by the Residue Theorem as

$$\frac{i}{r^2} \int_{-\infty}^{\infty} \frac{dk}{(2\pi)^2}\, k \frac{-kr\cos(kr) + \sin(kr)}{k^2 + \chi^2 m^2 \frac{k^2}{k^2+m^2}} = \frac{i}{4\pi r^2} \left(\frac{1 + \chi^2 e^{-mr\sqrt{1+\chi^2}}}{1+\chi^2} + \frac{mr\chi^2 e^{-mr\sqrt{1+\chi^2}}}{\sqrt{1+\chi^2}} \right). \tag{4.A.5}$$

If we now rotate back to the original co-ordinate system, we find that $\mathbf{I}$ points in the same direction as $\mathbf{x}$. Recalling (4.A.2), which was $\mathbf{A} = -i\mathbf{D} \times \mathbf{I}$, we find

$$\mathbf{A}(\mathbf{x}) = \frac{D}{4\pi r^2} \left(\frac{1 + \chi^2 e^{-mr\sqrt{1+\chi^2}}}{1+\chi^2} + \frac{mr\chi^2 e^{-mr\sqrt{1+\chi^2}}}{\sqrt{1+\chi^2}} \right) \hat{\phi}, \tag{4.A.6}$$

for $\mathbf{D}$ in the z-direction. Taking the curl of this equation gives us the magnetic field sourced by a magnetic dipole moment when a dark photon coupling is present:

$$\begin{aligned} \mathbf{B}(\mathbf{x}) =& \frac{D}{4\pi r^3 (1+\chi^2)^2} \\ & \cdot \Big\{ \Big[1 + \chi^2 e^{-m_X r} \left(1 + m_X r + \frac{1}{3}(m_X r)^2 \right) \Big] \Big(3\hat{\mathbf{x}} \cdot \hat{z}\hat{\mathbf{x}} - \hat{z} \Big) \\ & - \frac{2}{3} (\chi m_X r)^2 e^{-m_X r} (1+\chi^2) \hat{z} \Big\}. \end{aligned} \tag{4.A.7}$$

Chapter 5

Probing spin-dependent dark matter couplings with magnets

5.1 Introduction

As explained in the introduction, the search for keV to MeV mass DM requires new experimental techniques since the scattering of these particles deposits little energy on nuclei. In the absence of this experimental light, what can we say about the couplings of such states to the SM? Generically, the DM may couple to any of the SM particles, but here we will restrict ourselves to a study of the coupling to the electron, as one expects, on kinematic grounds, a greater sensitivity to these couplings. We will further restrict ourselves to DM-target scattering processes (as opposed to absorption processes), which are expected to be the dominant source of energy transfer if the DM is fermionic.

It is important to remember that the target with which the DM interacts is a many-body system. The many electrons in the system may be strongly coupled, and so on the face of it, an analytic treatment of the scattering may seem intractable. However, one may instead work with *collective modes* of the system, which interact only weakly with each other [157]. When is such a description of the system appro-

priate? This is in general a non-trivial question, but we may adopt the following rule-of-thumb. Let us assume that the excitations have some notion of energy $\tilde{\omega}_{\mathbf{p}}$, which may be decomposed in terms of a real part $\omega_{\mathbf{p}}$ and an imaginary part $\gamma_{\mathbf{p}}$[1]. Then the excitation is a useful concept if it is long-lived, i.e. we have

$$\gamma_{\mathbf{p}} \ll \omega_{\mathbf{p}}. \tag{5.1.1}$$

This condition is satisfied in solids if we are at low enough temperatures so that scattering between excitations does not induce decays, and if spontaneous decay is suppressed. The latter condition usually requires us to be at long wavelengths, so that there is some sort of phase space suppression.

We will see that the light DM kinematics of interest to us imply that we are in a regime where such a collective description of the modes is appropriate. We thus require a way of matching the UV interaction with electrons to an IR collective-mode interaction. The precise mode in question will depend on how the DM couples to the electron.

In particular, we will be interested in scenarios with a new force that couples to both the electron and the DM. If the electrons in the target material are non-relativistic, all DM-electron interactions are expressible in terms of only three operators that act on the electron's Hilbert space [158, 159]: the electron's number $\hat{N}_e$, spin $\hat{S}_e$, or orbital angular momentum $\hat{L}_e$. All three of these operators may excite phonons in the target, while the latter two may also excite magnons. We choose to focus here on interactions which couple only to the electron's spin $\hat{S}_e$, and so expect to find the largest coherent excitation rates for materials that exhibit strong spin correlations. In these materials, the magnon excitation rate is expected to dominate the phonon rate, since the latter is suppressed by the ratio of the momentum transfer to the scattering ion's mass q/m_i. For this reason, we restrict our attention

[1]The index $\mathbf{p}$ labels the (crystal) momentum, and so we also assume that there is some (discrete) translation symmetry.

to the possible sensitivity of magnon excitations to dark matter.

This topic has been previously studied [160], although only in isotropic materials and at sufficiently long wavelengths so as not to probe the electronic structure of the magnetic ions[2]. We will do away with both these requirements.

As we shall see in later sections, the expected excitation rate Γ of a target that is weakly perturbed by some incoming dark matter particle may be written schematically as

$$\Gamma = \langle \int d^3\mathbf{q}\, V_{ij} \cdot S^{ij} \rangle_{\mathbf{v}_\chi}, \tag{5.1.2}$$

where $\mathbf{q}$ is the momentum transfer of the scattering, V is a matrix with spatial indices i, j, which we shall call the "DM potential", that encodes the physics of the DM candidate in question, while S^{ij} is called the "spin structure factor", and encodes the material properties of the target; $\langle\cdot\rangle_{\mathbf{v}_\chi}$ denotes an average over the incoming DM velocity. For perturbative DM couplings, the V_{ij} are simple to calculate, and common results are tabulated in [160]. Thus all we must do is calculate S_{ij} for a candidate target material, and it is this calculation that we focus on from here on. We build on the general procedure outlined in [160] to calculate the structure function: we first match to the lattice degrees of freedom, and then calculate the relevant correlation functions in terms of this effective theory.

The particular materials we study are ferromagnets (FMs) for which the magnetic field arises purely from the electron's spins. Such systems may result when the contribution from orbital angular momentum is quenched, as is found in many magnets where the magnetic ion is a 3d transition metal. We analyse the suitability of K_2CuF_4 as a candidate FM, which is well described by a simple lattice theory of a single effective spin degree-of-freedom.

We also investigate the possibility of directional detection. Given the solar system's motion through the (assumed) isotropic DM halo, targets with an anisotropic

[2]By ion, we follow the literature and mean any object (atom *or* ion) which contains an unpaired electron that leads to magnetism.

response may exhibit a daily modulation in any signal due to the target orientation changing with the Earth's rotation. Further anisotropies may be induced by velocity-dependent DM-electron couplings, which lend additional power to the discrimination of signal and background. A simple way to obtain an anisotropic response is to use materials with 2d structure. The idea of using 2D structures, such as graphene, for directional detection is not new [161]. Here, however, we propose the use of quasi-2d magnets, which have approximately isotropic crystal structure at long wavelengths, yet exhibit planar magnetic couplings. This use of anisotropic magnetic materials is then expected to exhibit a daily modulation only for excitations arising from spin-dependent interactions, allowing for excellent background mitigation. We demonstrate that when the possible momentum transfer associated with a particular DM mass is close to the detectable threshold, a significant $\mathcal{O}(1)$ modulation is predicted.

An additional source of target anisotropy arises when the momentum transfer is large enough to probe the electron(s) around the magnetic ion. This effect is significant for $m_\chi \gtrsim$ MeV, although it is associated with a damping of the signal at large momentum transfer. We extend previous results by including the influence of magnetic form factors, and show that the anisotropy of the ionic wavefunctions induces an $\mathcal{O}(10\%)$ daily modulation in the signal for large DM masses.

Lastly, although we will calculate the structure factor that arises from a particular Hamiltonian, we will demonstrate that robust predictions, independent of a model, may be obtained for these excitation rates. These are obtained from neutron scattering data, which allow a handle on the target dynamics even if the collective excitations are strongly coupled. This is similar in spirit to recent papers [162, 163] that provide an analogous formalism for interactions that couple to the number density n_e, which is in turn based on a well-known result in the condensed matter literature [164].

A quick note on convention: throughout, latin indices i, j will correspond to

spatial indices, a, b will label individual electrons, α, β lattice sites, and Einstein summation convention is used for repeating latin indices, unless explicitly stated otherwise.

5.2 Factorising the problem

Let us begin by giving the exact form of the excitation rate given by Eq. (5.1.2). As stated, we are interested in coupling solely to the electron's spin. Concretely, we focus on an interaction Hamiltonian

$$H_{\text{int}} = \sum_a \mathbf{V}(\hat{\mathbf{r}}_\chi - \hat{\mathbf{r}}_a) \cdot \hat{\mathbf{S}}_a, \tag{5.2.1}$$

where the sum is over electrons indexed by a and the potential $\mathbf{V}$ depends only on the difference between the DM position $\mathbf{r}_\chi$ and the electron position $\mathbf{r}_a$. Within the Born approximation, the excitation rate is simple to derive. The detector excitation rate from its ground state $|0\rangle$ to some final state $|f\rangle$ reads

$$\Gamma(\mathbf{v}_\chi) = \int \frac{d^3\mathbf{q}}{(2\pi)^3 V_T} \sum_{ij} V_i(\mathbf{q}) V_j^\dagger(\mathbf{q}) \cdot \sum_f \langle f|\hat{S}_i(\mathbf{q})|0\rangle\langle 0|\hat{S}_j^\dagger(\mathbf{q})|f\rangle \cdot 2\pi\delta(\omega_f - \omega_{\mathbf{q}}), \tag{5.2.2}$$

where $(\omega_{\mathbf{q}} = \mathbf{q} \cdot \mathbf{v}_\chi - q^2/2m_\chi, \mathbf{q})$ is the 4-momentum transferred by the DM interaction, V_T is the target volume, $V_i(\mathbf{q})$ is the Fourier transform of $\mathbf{V}$, and we have

$$\hat{\mathbf{S}}(\mathbf{q}) = \sum_a e^{i\mathbf{q}\cdot\mathbf{x}_a} \hat{\mathbf{S}}_a. \tag{5.2.3}$$

As previously noted, the detector-specific many-body physics conveniently factorises and sits inside the spin-spin correlation function. This is a consequence of the fact that we assumed factorised initial and final states, and we work only to leading order. If we were to proceed to higher order, we must of course calculate the corrections that the DM perturbation introduces to the spin-correlations themselves.

Throughout this chapter, we just consider an interaction mediated by a vector boson V_μ of mass m_V, which couples to the axial vector current $J^\mu_{A,\psi} = \bar{\psi}\gamma^\mu\gamma^5\psi$ of the electron e and some spin-1/2 DM χ. In the non-relativistic limit, this gives a spin-spin interaction between the electron and DM upon integrating out the mediator

$$\begin{aligned}\mathcal{L} &\supset V_\mu \left(g_e J^\mu_{A,e} + g_\chi J^\mu_{A,\chi}\right) \\ &\xrightarrow{\text{NR}} \frac{4g_\chi g_e}{\mathbf{q}^2 + m_V^2}\mathbf{S}_\chi \cdot \mathbf{S}_e.\end{aligned} \tag{5.2.4}$$

This results in the benchmark DM potential that we use

$$\mathbf{V}(q) = \frac{4g_\chi g_e}{\mathbf{q}^2 + m_V^2}\mathbf{S}_\chi, \tag{5.2.5}$$

which, when averaged as for unpolarised scattering, leads to

$$\frac{1}{2}\sum_{S_\chi, S'_\chi} V_i(q)V_j^\dagger(q) = \left(\frac{4g_\chi g_e}{\mathbf{q}^2 + m_V^2}\right)^2 \delta_{ij}. \tag{5.2.6}$$

5.3 Matching to the lattice

We have seen from Eq. (5.2.2) that the basic object of interest is $\langle f|\hat{\mathbf{S}}(\mathbf{q})|0\rangle$. We wish to match this to a lattice theory in which the basic degrees of freedom are some effective lattice spins

$$\hat{\mathbf{S}}_\alpha = \sum_{a\in\alpha}\hat{\mathbf{S}}_a, \tag{5.3.1}$$

where α labels the lattice site and the sum is over all the electron spins at a site. For a crystal target, let us first then begin by calculating the matrix element for a single ion to go from some initial state $|\lambda_i\rangle = |\beta, S, S_z\rangle$ to some final state $|\lambda_f\rangle = |\beta', S', S'_z\rangle$

$$\sum_{a\in\alpha}\langle\lambda_i|e^{i\mathbf{q}\cdot\hat{\mathbf{x}}_a}\hat{\mathbf{S}}_a|\lambda_f\rangle, \tag{5.3.2}$$

where S labels the total spin, S_z its component along the z-direction, and β denotes the other quantum numbers of the site, including the electronic spatial wavefunctions (we have suppressed the lattice indices on all these quantities to avoid clutter).

The evaluation of such matrix elements follows a standard procedure [165]. Assume first that the lattice site has some definite position $\mathbf{X}_\alpha$ that changes adiabatically upon scattering, and write the electron's position in terms of its relative position with respect to this $\mathbf{x}_a = \mathbf{X}_\alpha + \mathbf{u}_a$. Then, we require knowledge of

$$e^{i\mathbf{q}\cdot\hat{\mathbf{X}}_\alpha}\langle\lambda_i|\sum_a e^{i\mathbf{q}\cdot\hat{\mathbf{u}}_a}\hat{\mathbf{S}}_a|\lambda_f\rangle. \tag{5.3.3}$$

If the total spin at the site is unchanged, $S = S'$, then we may make use of the Wigner-Eckart projection theorem, which states that for any SO(3)-vector operator $\hat{\mathbf{W}}$, its matrix elements obey

$$\langle\beta, S, S_z|\hat{\mathbf{W}}|\beta, S, S_z'\rangle = \frac{\langle\beta, S|\hat{\mathbf{W}}\cdot\hat{\mathbf{S}}|\beta, S\rangle}{S(S+1)}\cdot\langle\beta, S, S_z|\hat{\mathbf{S}}|\beta, S, S_z'\rangle. \tag{5.3.4}$$

Applying this to our expression with $\hat{\mathbf{W}} = \sum_a e^{i\mathbf{q}\cdot\hat{\mathbf{u}}_a}\hat{\mathbf{S}}_a$, we find

$$\langle\lambda_i|\sum_{a\in\alpha} e^{i\mathbf{q}\cdot\hat{\mathbf{u}}_a}\hat{\mathbf{S}}_a|\lambda_f\rangle = f_\alpha(\mathbf{q})\langle\lambda_i|\hat{\mathbf{S}}_\alpha|\lambda_f\rangle, \tag{5.3.5}$$

where $f_\alpha(\mathbf{q})$ is the "magnetic form factor" and the remain expectation value is of the total spin at the site as in Eq. (5.3.2).

The form factor, for the spin-only scattering considered here, is proportional to the electron charge density and is in general anisotropic, which will have important consequences for the daily modulation of the signal, as we will demonstrate. Its evaluation requires the electron wavefunctions, which have fortunately been calculated for ions of interest in the neutron scattering literature. For the Cu^{2+} magnetic ions of interest here, there is a single unpaired electron in a $3d_{x^2-y^2}$ orbital [166],

and so the form factor is [167]

$$f(\mathbf{q}) = \langle j_0 \rangle + \frac{5}{7}\left(3\cos^2\theta - 1\right)\langle j_2 \rangle + \frac{3}{56}\left(-30\cos^2\theta + 35\cos^4\theta + 35\sin^2\theta\cos 4\phi\right)\langle j_4 \rangle \tag{5.3.6}$$

where θ and ϕ are the polar and azimuthal angles, respectively, with the $x-y$ plane of the orbital taken along the equator; the functions $\langle j_n \rangle(q)$ are the weighting of the nth Bessel function over the radial wavefunction of the electron arising from an expansion in qR, with R the ionic radius. This form factor is illustrated in Fig. 5.1. A convenient phenomenological parametrisation is given by

$$\langle j_n \rangle(4\pi q) = q_n^2 \left(\sum_{i=1}^{4} A_{n,i} e^{-a_{n,i} q^2} \right), \tag{5.3.7}$$

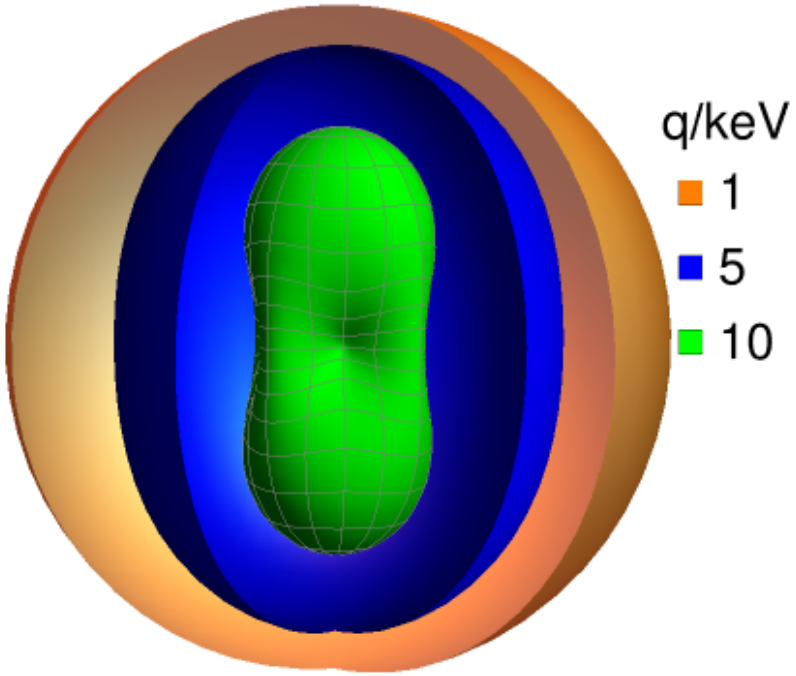

Figure 5.1: The magnetic form factor $f(q, \hat{n})$ plotted over the sphere for three choices of $q = |\mathbf{q}|$; the radial coordinate of the surface denotes the size of f. Note the pronounced anisotropy as q increases, as well as the fact that magnetic scattering is damped at large q.

where the prefactor is $q_0^2 = 1$ or $q_m^2 = q^2, n = 2, 4, 6$; the constants $A_{n,i}, a_{n,i}$ are taken from The Cambridge Crystallographic Subroutine Library.

It is important to recognise that this matching procedure was target specific, as we required knowledge of the magnetic ion and its electron's wavefunction. This is in contrast to claims in the (high energy) literature, that the matching to the lattice is universal [159]. This universality is only strictly true in the long wavelength limit

$$e^{i\mathbf{q}\cdot\hat{\mathbf{u}}_a} \simeq 1, \tag{5.3.8}$$

when the matching to $\hat{\mathbf{S}}_\alpha$ indeed becomes trivial. This approximation is accurate to within $\mathcal{O}(10\%)$ only for $q \lesssim 10\,\mathrm{nm}^{-1}$, which is the characteristic momentum for $m_\chi \lesssim 2\,\mathrm{MeV}$. The above multipolar expansion of the form factor, however, extends well into the ionic radius.

To recap, we have shown that the dynamics of individual electrons may be matched to the dynamics of an effective lattice spin at wavelengths that are long with respect to the ionic size by introducing a magnetic form factor f_α. The total matrix element is then a sum over lattice sites of this matched matrix element. Restricting ourselves to systems where all the ions are equivalent, $f_\alpha = f$, the relevant matrix element may be written

$$\langle \hat{\mathbf{S}}(\mathbf{q}) \rangle = f(\mathbf{q}) \langle 0 | \sum_\alpha e^{i\mathbf{q}\cdot\hat{\mathbf{X}}_\alpha} \hat{\mathbf{S}}_\alpha | f \rangle, \tag{5.3.9}$$

where the relevant states are now projected down to the level of the effective lattice theory.

5.4 Spin-spin correlations and magnons

With a lattice spin correlation function in hand, we now turn to its evaluation. We will make use of some standard results in the theory of magnetic excitations (for a

brief review of magnets and magnons, see appendix A).

Consider the Heisenberg magnet, described by the Hamiltonian

$$\mathcal{H} = \sum_{\langle\alpha\beta\rangle} J_{\alpha\beta}\mathbf{S}_\alpha \cdot \mathbf{S}_\beta, \tag{5.4.1}$$

where the sum is over nearest-neighbour sites $\langle\alpha\beta\rangle$ that are coupled with a strength $J_{\alpha\beta}$. The behaviour of the system depends strongly on the sign of $J_{\alpha\beta}$: if negative, the system is a FM, otherwise it is an AFM. We will discuss on the FM case.

5.4.1 Ferromagnetic magnons

The low-lying excitations above the FM ground state are the single-magnon states, indexed by a crystal momentum $|\mathbf{q}\rangle$. The dynamics of single magnons are described in Appendix A. At low energies, these modes dominate the system's dynamics, and the spin-spin correlation function may be approximated within the framework of linear spin-wave theory as

$$\begin{aligned}\tilde{S}_{ij}(\omega, \mathbf{q}) &\equiv \frac{1}{V_T}\sum_f \langle f|\hat{S}_i(q)|0\rangle\langle 0|\hat{S}_j^\dagger(\mathbf{q})|f\rangle\delta(\omega_f(\mathbf{q}) - \omega) \\ &= n_S\,\delta(\omega - \Omega(\mathbf{q})),\end{aligned} \tag{5.4.2}$$

where ω_f is the energy of the final state, which is equal to the magnon's energy Ω in this regime and n_S is the spin density of the system. At higher energies, there are more terms appearing in the sum over final states, but we may take this to be a lower bound on the size of the correlator. In ignoring higher-order corrections to the linearised theory, the magnons contribute as δ-spikes in frequency space, since decays, and thus a widening of the Lorentzian line-shape, are forbidden at this order. This justifies the collective treatment we carry out here since the condition Eq. (5.1.1) is trivially fulfilled, although we of course expect our approximations to break down as the amplitude of the fluctuations grows.

The candidate FM we consider is K_2CuF_4, a quasi-2d FM [168, 169, 170]. It has a square-lattice crystal structure (in the $x-y$ plane, say), where neighbouring sites within the square plane are coupled with strength $J_{\alpha\beta} = -J$, while the spins along the orthogonal plane are uncoupled. The spin can nonetheless point in any direction, not just in the magnetised plane, in contrast to so-called "easy-plane" magnets. The resulting dispersion relation for this system is

$$\Omega(\mathbf{q}) = 4Js\left(\sin^2\frac{q_x a}{2} + \sin^2\frac{q_y a}{2}\right); \tag{5.4.3}$$

the relevant parameters are $a = 4.125\,\text{Å} \simeq 8.70\,\text{keV}^{-1}$, $Js = 1.0\,\text{meV}$, and the perpendicular direction repeats with size $c = 12.669\,\text{Å}$, as shown in Fig. 5.2. Note that the dispersion relation is flat along the z-direction. This has important implications for DM direct detection, since at times of the day where the DM velocity is predominantly aligned with the flat direction, there will be less energy deposited in the target. This will cause a significant daily modulation, as we shall see.

5.5 Phase space integrals

We now have all the ingredients necessary to calculate the DM-scattering rate as a function of DM velocity. To obtain a total expected rate, we must average over the dark matter velocity distribution $f_\chi(\mathbf{v})$. We take the standard form of a Maxwell-Boltzmann distribution truncated at the sphere of radius v_{esc} in the galactic frame, i.e. in the laboratory frame we have

$$f_\chi(\mathbf{v}) = N_0 \exp\Big[-(\mathbf{v}+\mathbf{v_e})^2/v_0^2\Big]\Theta(v_{\text{esc}} - |\mathbf{v}+\mathbf{v_e}|), \tag{5.5.1}$$

where the normalisation N_0 is

$$N_0 = \pi v_0^2\left(\pi^{1/2} v_0\,\text{Erf}(v_{\text{esc}}/v_0) - 2v_{\text{esc}}e^{-v_{\text{esc}}^2/v_0^2}\right). \tag{5.5.2}$$

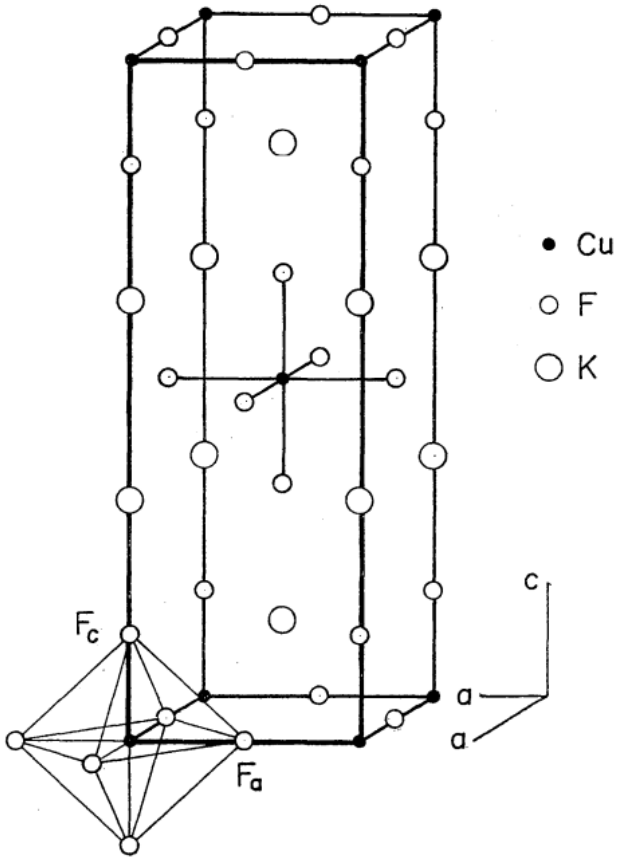

Figure 5.2: The crystal structure of K_2CuF_4, taken from [169]. The unpaired spin of the Cu^{2+} magnetic ion couples to the other magnetic spins in the square plane labelled by $a - a$; the magnetisation direction may point in any direction. Spins along the c direction are uncoupled. The squashed octahedral structure of the F ions around the magnetic ion, shown in the bottom left, leads to the anisotropy in the form factor at large momentum transfer.

The numerical values we use are $v_0 = 230\,\mathrm{km/s}$, $v_{\mathrm{esc}} = 600\,\mathrm{km/s}$, and $v_e = 240\,\mathrm{km/s}$.

The average rate is in general given by

$$\bar{\Gamma} = \int d^3\mathbf{v}\, f_\chi(\mathbf{v})\Gamma(\mathbf{v}), \tag{5.5.3}$$

which involves six integrals. This is related to the average rate per target mass by

$$R = \rho_T^{-1} \frac{\rho_\chi}{m_\chi} \bar{\Gamma}, \tag{5.5.4}$$

and we take $\rho_\chi = 0.4\,\mathrm{GeV/cm^3}$, and $\rho_T = 3.18\,\mathrm{g/cm^3}$. In order to evaluate this expression, it is simplest to work in the galactic frame, where the DM distribution is isotropic in galactic velocity $\mathbf{v}' = \mathbf{v} + \mathbf{v}_e$. Beginning with the velocity integral, we may use this isotropy to align the azimuthal axis of the $\mathbf{v}'$ integral with $\mathbf{q}$, and use the delta function to evaluate the integral over $\cos\theta_{v'q}$, the angle between $\mathbf{q}$ and $\mathbf{v}'$:

$$\bar{\Gamma} = \frac{32 g_\chi^2 g_e^2}{m_V^4} N_0 \int_{\mathbf{q}} \int dv' \, \frac{v'}{q} e^{-v'^2/v_0^2} \, |f(\mathbf{q})|^2 \tilde{S}^i{}_i(\omega_\mathbf{q}, \mathbf{q}) \, \Theta(v_{\mathrm{esc}} - v') \, \Theta\left(v' - v'_{\mathrm{min}}(\mathbf{q})\right), \tag{5.5.5}$$

which is only non-vanishing for $v'_{\mathrm{min}} < v_{\mathrm{esc}}$ with

$$v'_{\mathrm{min}}(\mathbf{q}) = \frac{q}{2m_\chi} + \frac{\Omega_\mathbf{q}}{q} + \mathbf{v_e} \cdot \mathbf{q}; \tag{5.5.6}$$

recall $f(\mathbf{q})$ is the magnetic form factor of Eqn. (5.3.9), while $\tilde{S}^i{}_j$ was the spin correlator of Eqn. (5.4.2). The last integral over v' is a simple exponential,

$$\bar{\Gamma} = \frac{16 g_\chi^2 g_e^2 v_0^2}{m_V^4} N_0 \int d^3\mathbf{q} \, q^{-1} |f(\mathbf{q})|^2 \tilde{S}^i{}_i(\omega_\mathbf{q}, \mathbf{q}) \left(e^{-v'^2_{\mathrm{min}}(\mathbf{q})/v_0^2} - e^{-v_{\mathrm{esc}}^2/v_0^2} \right) \Theta\left(v_{\mathrm{esc}} - v'_{\mathrm{min}}(\mathbf{q})\right), \tag{5.5.7}$$

while the analytic feasibility of the last integrals over momentum transfer depends on the particular dispersion relation and spin-spin response function. In practice, the systems we consider have no residual spatial symmetry, and so we carry out the integrals numerically.

5.6 Daily modulation of signal

The anisotropy of the target is sensitive to the rotation of the Earth through the DM wind. Recall that we work in a co-ordinate system in which the crystal magnetisation plane is the $x-y$-plane. Then, aligning the x-axis with the Earth's velocity direction

at $t = 0$, the Earth's velocity may be written [171]

$$\mathbf{v}_e(t) = \hat{R}_x(\beta) \cdot \begin{pmatrix} \cos^2\Theta + \sin^2\Theta\cos\phi(t) \\ \sin\Theta\sin\phi(t) \\ \sin\Theta\cos\Theta(\cos\phi(t) - 1), \end{pmatrix} \tag{5.6.1}$$

where $\hat{R}_x(\beta)$ is a rotation around the x-axis through an angle β, $\Theta = 43^\circ$ is the angle between the Earth's axis of rotation and the velocity of the solar system in the galactic frame, and $\phi(t) = 2\pi t/T$ is the phase of the Earth's rotation, with $T = 24$ hours. We choose $\beta = 90^\circ$ so that the component of the velocity in the magnetisation plane oscillates with a period of half a day.

How does this oscillating velocity affect the energy of the excited magnon modes? Just to get a feel for the problem, approximate the the momentum transfer as $\mathbf{q} \simeq m_\chi v_0 (1 + \mathbf{v}_e(t)/v_0)$, so that $\Omega(\mathbf{q}(t))$ oscillates around its average value as shown in Fig. 5.3. We see that for small masses, the emergent $O(2)$ symmetry of the dispersion relation at long wavelengths causes the energy to oscillate in phase with the component of the Earth's velocity in the magnetic plane. However, at larger momenta, this is no longer true, and the period and phase of the oscillations changes.

In Fig. 5.4, we plot the expected signal rate over the course of a day, for a selection of DM masses. The absolute magnitude of the oscillation may be large – as big as 10%. The phase of the oscillations is also mass dependent, due to its effect on the dispersion relation.

5.7 Statistical measures

In this section, we outline two possible measures of detecting the DM signal. The first makes no use of the daily modulation, and is simply a measure of the total number of scattering events. The second measures the asymmetry in 6 hour bins

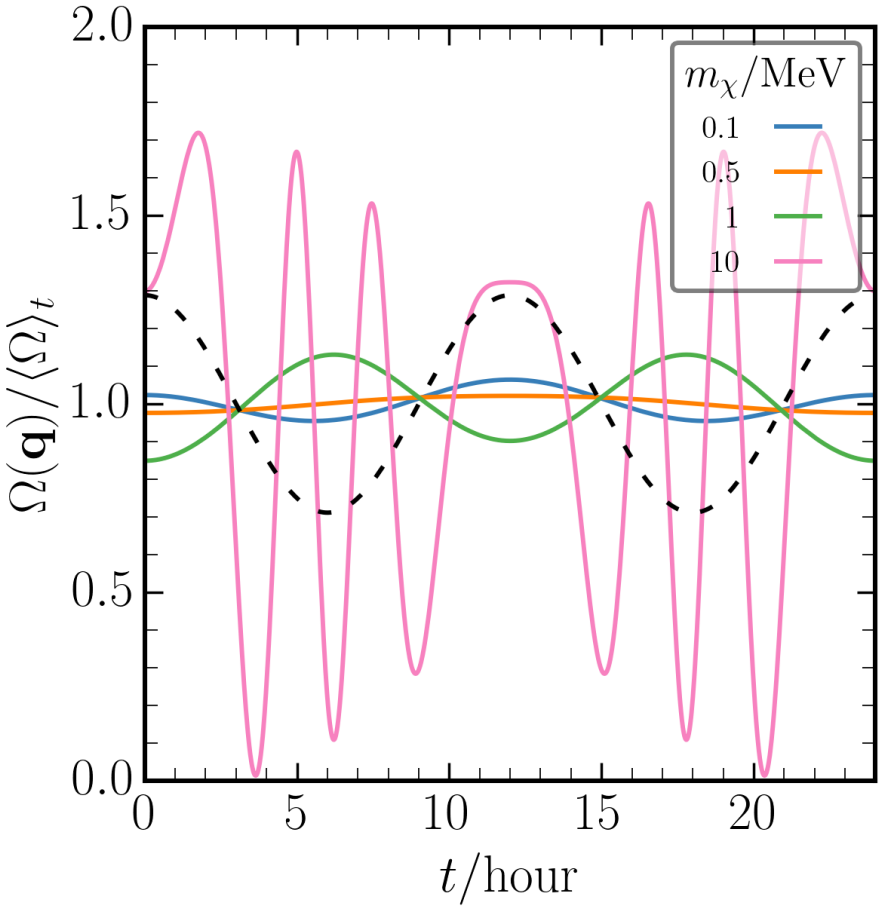

Figure 5.3: The expected energy of a magnon excitation, assuming, for illustrative purposes, that the momentum transfer is given by $\mathbf{q} = m_\chi v_0(1 + \mathbf{v}_e(t)/v_0)$; the y-axis is normalised to the average over a 24 hour period. The dashed black line shows the expectation in the long-wavelength limit when $\Omega(\mathbf{q})$ exactly tracks the component of the velocity in the magnetisation plane.

across the day, and is indicative of a non-constant signal.

The expected rate per target unit mass may be expressed parametrically by

$$R = \bar{g}^4 \frac{\rho_\chi}{\rho_T} \frac{m_V^4}{m_\chi^5 (g_\chi\, g_e)^2} \bar{\Gamma}, \tag{5.7.1}$$

where we define an effective dimensionless coupling by

$$\bar{g}^2 \equiv \frac{g_\chi g_e m_\chi^2}{m_V^2}. \tag{5.7.2}$$

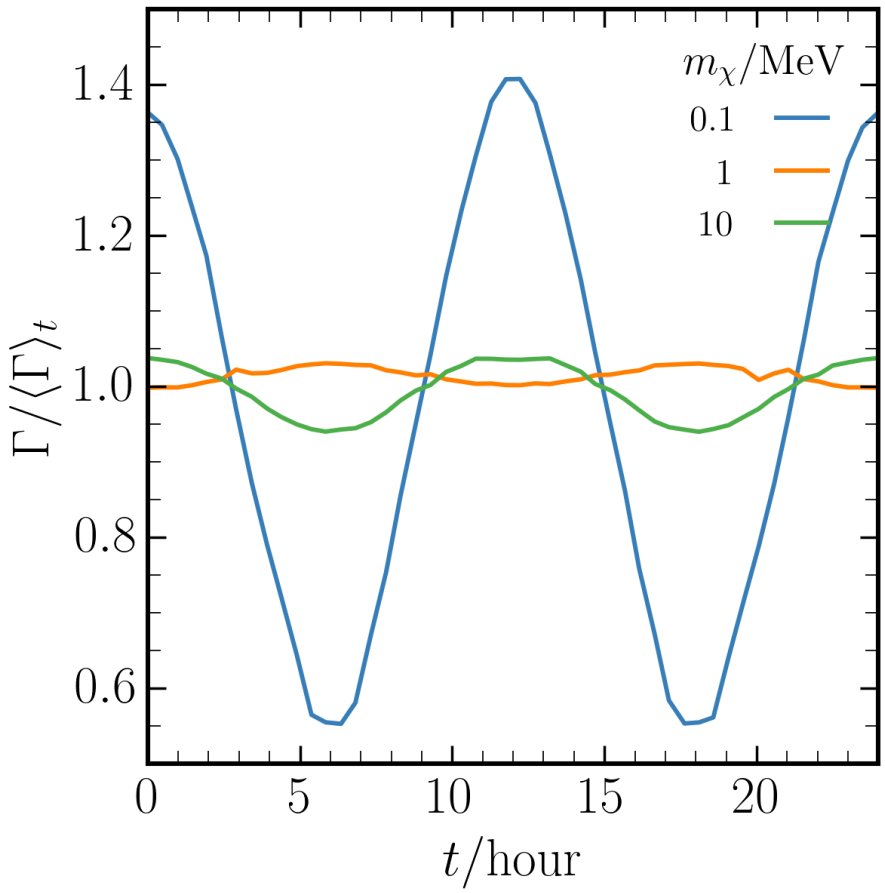

Figure 5.4: The expected signal rate over a day, normalised to its mean. Note the phase change at intermediate masses, where the oscillation due to the (maximally) anisotropic dispersion relation shifts, as seen in Fig. 5.3. The large oscillations in the expected energy of the magnon at large masses has little effect on the expect excitation rate, since these are all above threshold throughout the day – energy discrimination would be needed to observe this effect.

For the sake of comparison with the literature, we first assume a threshold minimum energy of $\omega_{\text{min}} = 1\,\text{meV}$, and a background-free 1 kg year experiment. One may then obtain a 95% confidence limit exclusion limit that corresponds to observing 3 signal events by directly averaging the rate over a 24 hour period.

The result of the averaging procedure is given in Fig. 5.5. Although formally such a method is expected to give the strongest bounds, it is important to remember that this is assuming complete background mitigation. In reality, this is impossible – it is unclear whether such a projection holds any useful meaning.

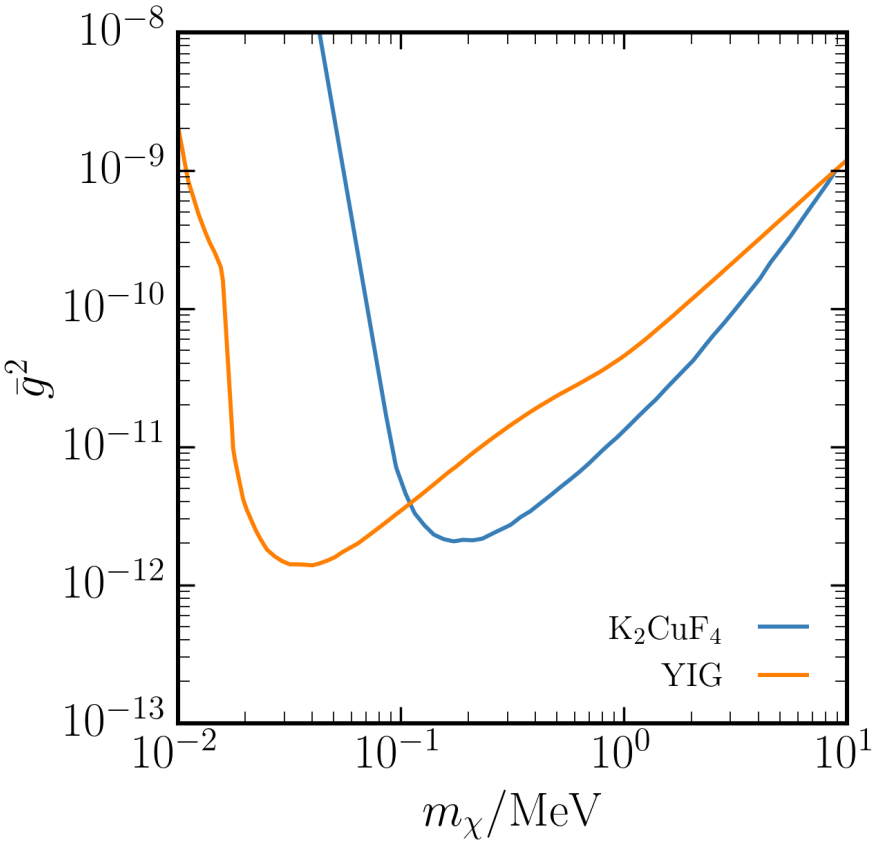

Figure 5.5: Contour corresponding to 3 events per kg year exposure for K_2CuF_4 (blue), compared with those obtained in [159] for a material known as YIG (orange). It is easier for very low mass DM to excite a magnon in YIG since it has a lattice spacing approximately three times that of K_2CuF_4. Note the difference in slope above an MeV, due to our inclusion of the magnetic form factor.

Due to the anisotropic nature of the target, there can be significant daily modulation of the signal. Exploiting this effect allows us to get a much more robust sense of the possible sensitivity of a 2d ferromagnet. Assuming that most of the signal power is in the lowest harmonic, which oscillates with a period of a 12 hours (not 24, due to an approximate parity symmetry), the appropriate measure of this effect is given by the difference of the average rate between 6 hour bins

$$f_2(t_0) = \frac{1}{T\langle R\rangle_T}\left(\int_{t_0}^{t_0+6\,\mathrm{hr}} R(t)\,dt - \int_{t_0-6\,\mathrm{hr}}^{t_0} R(t)dt\right), \tag{5.7.3}$$

as introduced in [172]. In this expression, $T = 24\,\mathrm{hr}$, $\langle R\rangle_T$ is the time-averaged

rate, while t_0 sets the phase of the oscillations. Since the phase of the DM signal depends on the DM mass, choosing a fixed t_0 in Eq. (5.7.3) is not a good measure of the day-night asymmetry for all DM masses, motivating us to instead choose $f_2 \equiv \max_{t_0} f_2(t_0)$. In terms of this measure, the statistical significance of an oscillating signal is given by

$$n_\sigma = \frac{f_2 T_{\rm exp} \langle R \rangle_T}{N_{\rm tot}^{1/2}}, \tag{5.7.4}$$

where $T_{\rm exp}$ is the total exposure time, and $N_{\rm tot}$ is the total number of events measured at the experiment. Assuming a constant background rate R_b that scales linearly in both the exposure time and the target mass, the discovery potential increases with exposure time, even without background mitigation.

5.8 Sensitivity to dark matter

We now finally turn to the projected sensitivity to an oscillating DM signal. In the absence of a detailed background calculation, we take a benchmark constant background rate of $R_b = 1/60\,\mathrm{Hz\,kg^{-1}}$ for our projections. Of course, this must be calculated precisely to obtain a robust projection, but the overall effect of a modified background rate on the projected sensitivity is a simple rescaling. We again assume a 1 meV threshold. In Fig. 5.6, we plot the contours in the mass-coupling plane at which the modulation of the signal becomes statistically significant at 3σ for two target masses, assuming a 1 year exposure time. We also show the line at which the signal is as large as the background, indicating the importance of discriminating between these two classes of events.

To the best of my knowledge, there has not been a study of the bounds on spin-dependent DM couplings to electrons. It is likely that many of the usual bounds on DM would still hold. Therefore, even though there are no other bounds on our plots, this should not be taken to mean that all the parameter space is unconstrained.

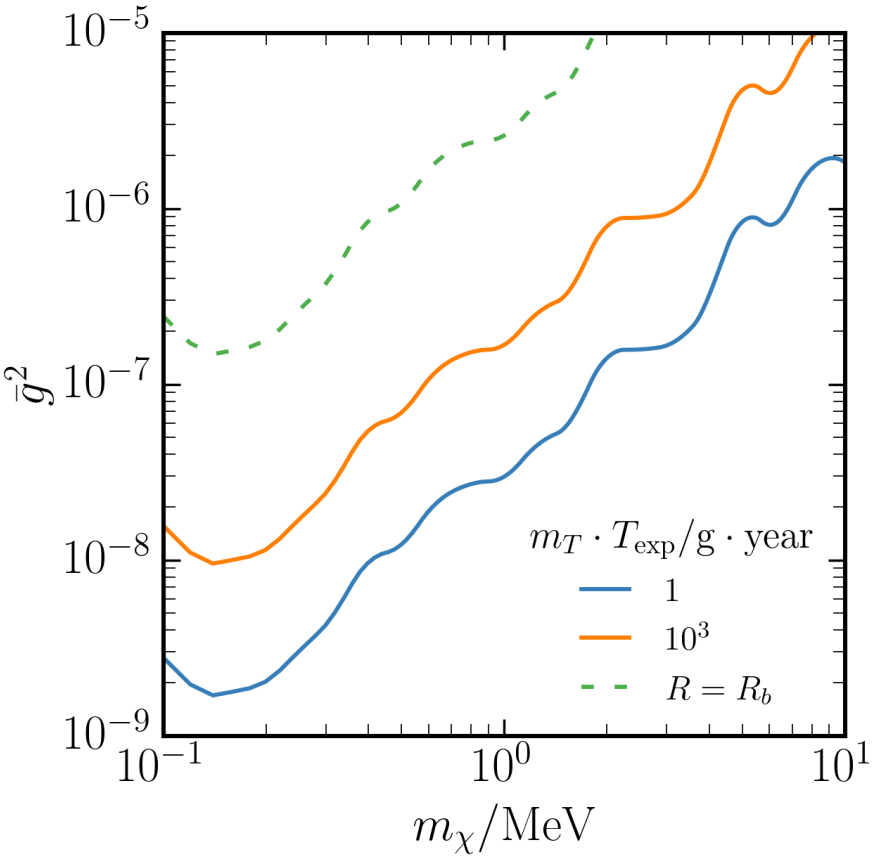

Figure 5.6: Contours corresponding to 3 sigma detection – using Eqn. (5.7.4) – of a modulating signal over a constant background at a rate per unit mass of $R_b = 1\,\mathrm{min}^{-1}\,\mathrm{kg}^{-1}$. We plot the values both for a g year exposure (orange), and for kg year exposure (blue). In dashed green, we indicate when the signal rate equals the background rate.

5.9 Towards an exact result

The results so far have strictly applied only to one-magnon excitations within the framework of linear spin-wave theory. In this section, we show how to calibrate more directly to experimental data and do away with these assumptions. Our method is analogous to the proposal of [162, 163], where it was pointed out that one can directly measure the part of the correlation function relevant for DM scattering.

We begin with the observation that the cross section for magnetic neutron scat-

tering from some initial momentum k_i to a final momentum k_f is

$$\frac{d^3\sigma}{d\Omega dE_f} = \frac{k_f}{k_i}\left(\frac{\gamma r_0}{2\mu_B}\right)^2 |f(\mathbf{q})|^2(\delta_{ij} - \hat{q}_i\hat{q}_j)\tilde{S}_{ij}(\omega, \mathbf{q}). \tag{5.9.1}$$

Since neutron scattering proceeds via a magnetic dipole interaction, only the piece of the spin-spin correlation orthogonal to the direction of momentum transfer contributes. This projection onto the orthogonal subspace naively precludes a direct comparison between neutron- and DM-scattering.

The way forward is to note that we may in fact rotate away the $\hat{q}$-dependence in the projector if the crystal is made up of many domains, with the direction of a particular domain's magnetisation being isotropically distributed [173]. This is indeed the case in many crystals of interest, in particular the ones studied here.

5.9.1 Domains

Since we are interested in the physics of multi-domain systems, let us rewrite the spin correlator in a way that brings out the structure of the domains. The relevant function is

$$\tilde{S}_{ij}(\omega, \mathbf{q}) = \int dt e^{-i\omega t} \sum_{\alpha\beta} e^{i\mathbf{q}\cdot(\mathbf{X}_\alpha - \mathbf{X}_\beta)} \langle S_{\alpha,i}(t) S_{\beta,j}(0)\rangle, \tag{5.9.2}$$

where we place a tilde to emphasise that the matrix elements are at the level of the lattice, and so omit form factors, etc; recall that the sum over α, β indicates a sum over all sites on the lattice. Note that only the symmetric (in i, j) part of this contributes to scattering processes. We may split this sum into a sum over domains D and a further sum over sites within this domain, which we denote

$$\sum_\alpha = \sum_D \sum_{\alpha\in D}. \tag{5.9.3}$$

We now assume that spins in different domains are uncorrelated. Physically, this means that the magnons cannot propagate between domains – they are scattered

by the domain walls and the coherent wave is destroyed. Thus, the correlator is diagonal in D-space.

To evaluate the spin-correlation function, we have implicitly been assuming a fiducial co-ordinate system in which we quantise the spins along a preferred z-axis. In a multi-domain system, it is convenient to have a local co-ordinate system where the magnetisation direction is aligned with the z-direction. We will denote quantities evaluated in this system with a prime $'$, and we introduce a domain-dependent rotation matrix that takes us from the local co-ordinate system to the global one:

$$\langle S_\alpha(t) S_\beta(0)\rangle = R \cdot \langle S'_\alpha(t) S'_\beta(0)\rangle \cdot R^T. \tag{5.9.4}$$

In terms of the local system, the projection of $\tilde{S}$ is

$$\Delta_{ij}(\hat{q})\tilde{S}_{ij}(\omega,\mathbf{q}) = \sum_D (\delta_{ij} - \hat{q}_i^D \hat{q}_j^D) \int dt e^{-i\omega t} \sum_{\alpha,\beta\in D} e^{i\mathbf{q}\cdot(\mathbf{X}_\alpha - \mathbf{X}_\beta)} \langle S'_{\alpha,i}(t) S'_{\beta,j}(0)\rangle, \tag{5.9.5}$$

where $\hat{q}^D$ is the rotated momentum unit vector: $\hat{q}^D = R^D \cdot \hat{q}$. To evaluate this sum, a final assumption must now be made: let all the domains be approximately equal, with the magnetisation direction being on average isotropic, i.e. $[\mathcal{H}, \sum_\alpha S^i_\alpha] = 0$.. This means we can translate a sum over the domain-specific rotations into an isotropic integral over rotation matrices. Explicitly, we parametrise the rotations R^D in terms of a rotation axis $\hat{n}$, specified by polar co-ordinates (θ,ϕ) and an angle γ, for which the normalised, isotropic Haar measure is [174] $d\Omega = \frac{1}{2\pi^2}\sin^2\frac{\gamma}{2} d\gamma\, d\cos\theta\, d\phi$ and we have $\hat{q}_i^D = (\cos\gamma\delta_{ij} + \sin\gamma\,\epsilon_{ikj}\hat{n}_k + (1-\cos\gamma)\hat{n}_i\hat{n}_j)\,\hat{q}_j$. As is evident from Eq. (5.9.5), to evaluate the projected correlator we only require knowledge of

$$\int d\Omega\, (R(\Omega)\cdot\hat{q})_i\, (R(\Omega)\cdot\hat{q})_j = \frac{1}{3}\delta_{ij}, \tag{5.9.6}$$

making use of $\int d\Omega\, (\hat{q}\cdot R\cdot\hat{q})^2 = 1/3$ and $\int d\Omega\, |R\cdot\hat{q}|^2 = 1$. This demonstrates that the isotropic distribution of domains simply effects a calculable rescaling of the

scattering potential, allowing one to determine $\tilde{S}_{ii}$ directly from neutron scattering data. Similar observations exist in the neutron scattering literature, e.g. [175, 173].

Finally, note that even though the magnetisation directions are isotropically distributed, there can still be a daily modulation of a DM signal. The couplings of the underlying lattice nonetheless break the isotropy. One may think of the spin isotropy as being an internal symmetry of the system, meaning that the anisotropy of the dispersion relation and form factors in real space still contribute.

5.10 Conclusions

We have shown that quasi-2d ferromagnets allow for directional detection of light dark matter that couples only to spin. This is the first time such a proposal has been made in the literature. As we demonstrated, the daily modulation of the signal induced by the target anisotropy gives a vital handle on background discrimination. We have also shown the importance of including magnetic form factors in evaluating the sensitivity to larger DM masses.

This work has assumed that single magnon excitations are measurable. Currently, this is not possible, but this case study may lend further motivation to the ongoing development of such technologies [176, 177].

The multi-magnon regime, on the other hand, is currently within experimental reach, and is being used to search for axion dark matter in the QUAX experiment [178]. This uses a resonant cavity to read out multi-magnon excitations at a particular frequency. It would be interesting to apply the non-perturbative techniques we have pointed out in section 5.9 to see what the possible reach of QUAX is to the DM candidate we have considered.

Another open question is what the theoretical maximum sensitivity of a magnon DM detector might be. This would arise from sum rules bounding the spin-spin correlation function, since it, as a causal two-point function, satisfies the usual

dispersion relations. Indeed a similar idea was investigated in [179], where dispersion relations were applied to the dielectric tensor. This exercise would set a target for phenomenologists to aim at, but we leave this for now. A perhaps promising target is to use anti-ferromagnets, which have linear dispersion relations at long wavelengths, suggesting that the density of states relevant for long-wavelength scattering would be higher.

Appendix A

Magnets and magnons

We give a concise introduction to the relevant properties of magnetic excitations. We focus on simple square-lattice ferromagnets and the linear spin-wave treatment of magnons. For a more information, see [167].

Throughout this section, we work with the Heisenberg magnet

$$\mathcal{H} = \sum_{\langle\alpha\beta\rangle} J_{\alpha\beta} \mathbf{S}_\alpha \cdot \mathbf{S}_\beta, \tag{A.0.1}$$

with a spin operator $\mathbf{S}_\alpha$ acting on each site. A basis of states at a site is given by the eigenstates $|m\rangle_\alpha$ of S^z_α:

$$S^z_\alpha |m\rangle_\alpha = m|m\rangle_\alpha \tag{A.0.2}$$

for $m = -s, \ldots s$. We will also find it useful to define the spin raising and lowering operators

$$S^\pm_\alpha = S^x_\alpha \pm i S^y_\alpha, \tag{A.0.3}$$

in terms of which the above Hamiltonian is

$$\mathcal{H} = \sum_{\langle\alpha\beta\rangle} J_{\alpha\beta} \Big[S^z_\alpha S^z_\beta + \frac{1}{2} \left(S^+_\alpha S^-_\beta + S^-_\alpha S^+_\beta \right) \Big]. \tag{A.0.4}$$

A.1 Ferromagnets

A.1.1 Finding the magnon hamiltonian

The sign of $J_{\alpha\beta}$ in Eq. (A.0.1) is crucial in determining the ground state and the excitations above it. For $J_{\alpha\beta} = -|J_{\alpha\beta}|$, we have an exact ferromagnetic ground state, in which all the spins are aligned in the z-direction, say,

$$|0\rangle_{FM} = \prod_{\alpha} |s\rangle_{\alpha}. \tag{A.1.1}$$

Excitations around the ferromagnetic ground state may be studied by means of a Holstein-Primakoff transformation [180]. Defining the operators a_α by

$$\begin{aligned} S^z_\alpha &= s - a^\dagger_\alpha a_\alpha, \\ S^+_\alpha &= \sqrt{2s\left(1 - \frac{a^\dagger_\alpha a_\alpha}{2s}\right)}\, a_\alpha, \end{aligned} \tag{A.1.2}$$

we observe that the $\mathfrak{so}(3)$ commutation relations of S^i_α imply that the creation and annihilation operators obey the cannonical commutation relations for *bosons*. The space of states spanned by the operators S, a is in general different (by Fermi's exclusion principle), so one must impose the constraint that there are no more than $2s$ bosons at a site.

For small fluctuations around the ground state, we take the eigenvalues $n = s - m$ of the number operator

$$a^\dagger_\alpha a_\alpha |n\rangle = (s - m)|n\rangle \tag{A.1.3}$$

to be small with respect to s. We may then express the Hamiltonian (A.0.1) in terms of our new variables (A.1.2), and linearise in n/S, restricting ourselves to work only with the low-lying states, thus forgetting about the constraint. The

resulting Hamiltonian, to leading order, is

$$\mathcal{H}_0 = \sum_{\mathbf{q}} \Omega(\mathbf{q}) a^\dagger_{\mathbf{q}} a_{\mathbf{q}}, \tag{A.1.4}$$

where we have gone to momentum space

$$a_\alpha = N^{-1/2} \sum_{\mathbf{q}} e^{i\mathbf{q}\cdot\mathbf{x}_\alpha} a_{\mathbf{q}}, \tag{A.1.5}$$

subtracted the zero-point energy, and expressed the energy of each mode as $\Omega(\mathbf{q})$. Note that to this order in the expansion, the bosonic ladder operators are linearly related to the $S^\pm$:

$$S^+_\alpha \simeq \sqrt{2s} a_\alpha. \tag{A.1.6}$$

For a quasi-2d square lattice ferromagnet with lattice spacing a, in which all nearest-neighbours within a plane are coupled with the same strength $-J$, we have

$$\Omega(\mathbf{q}) = 4Js \left(\sin^2 \frac{q_x a}{2} + \sin^2 \frac{q_y a}{2} \right), \tag{A.1.7}$$

where the sites are taken to be coupled in the $x-y$ plane. The excitations which carry this energy are called spin-waves, or magnons. Calculating the xx and xy correlations of the spin operator, we see that they are $\pi/2$ out-of-phase, indicating that the spins are precessing coherently around the magnetisation direction.

A.1.2 One-magnon correlations

At low energies, the DM-target scattering will predominantly excite a single magnon. We thus take the excited state $|f\rangle$ to be a single magnon state, labelled by a momentum $|\mathbf{q}\rangle$. We now wish to calculate the matrix element of the spin operator in momentum space $\hat{\mathbf{S}}(\mathbf{q})$ between the ground state $|0\rangle$ and this final state $|\mathbf{q}\rangle$ appear-

ing in

$$S_{ij}(\omega, \mathbf{q}) \equiv \frac{1}{V}\langle \mathbf{q}|\hat{S}_i(q)|0\rangle\langle 0|\hat{S}_j^\dagger(0)|\mathbf{q}\rangle \cdot \delta(\Omega(\mathbf{q}) - \omega). \tag{A.1.8}$$

Observe that the linearised Hamiltonian in (A.1.4) commutes with S_α^z, and that, by Eq. (A.1.6), the one-magnon state has S^z eigenvalue $s-1$. Hence $S_{zi} = S_{xy} = 0$ and $S_{xx} = S_{yy} \equiv S$ (after symmetrising the spatial indices). A straightforward calculation gives the only non-zero component of the matrix:

$$S = n_S \delta(\omega - \Omega(\mathbf{q})), \tag{A.1.9}$$

where n_S is the effective spin density per volume of the ferromagnet.

Appendix B

Final thoughts and future directions

In Chapters 2 and 3, we demonstrated that the BEBC experiment is still capable of placing competitive bounds on a variety of BSM particles in the GeV mass range. More broadly, this work fits into the current program of searching for new physics at forward physics facilities, for instance at the LHC [85]. Given the large investments that must be made into the development and running of these new experiments, it is important to extract as much information as possible out of existing data in order to weigh the relative merit of any projected bounds. Having done so, at least for limited classes of particles, it might be interesting to explore whether these soon-to-be facilities may be used to search for BSM physics in novel ways. In particular, one might look to the rich neutrino physics program of the FASERν experiment [181, 182].

As an illustrative example, the ability to measure, for the first time, TeV tau neutrinos may gives us new information about BSM physics that affects the production, propagation and subsequent detection of the ν_τ. FASERν is expected to see 10 tau neutrinos during Run 3 of the LHC (to be compared with the 9 that have been seen between DONUT [183] and OPERA [184], which operated at beam energies of 800 and 400 GeV, respectively). This may be a relevant direction to take this line of research. Other possible avenues surely exist to allow phenomenologists

to take advantage of this heroic experimental effort, making this an exciting time for forward physics.

In Chapter 4, we investigated the dark photon limits that may be set from considering the magnetospheres of celestial bodies. As explained, the size of the magnetosphere sets the Compton wavelength of the dark photon that may be probed. Hence, in order to look for even lighter dark photons, one must go to larger bodies. The next obvious candidate after Earth and Jupiter is of course the Sun. Indeed, there has been a recent space mission with the express aim of measuring properties of the solar environment: the Parker Solar Probe [185]. Given that it has measured both the magnetic field around the Sun [186], as well as its plasma components [187], this might be a promising way to go. However, it must of course be said that the solar magnetosphere is a complex place, with dynamics occurring on short time scales, which might complicate the extraction of robust bounds on dark photons.

Chapter **??** dealt with the possibility of looking for dark matter coupling through spin-dependent interactions. We have shown that our proposal is at least as competitive as others in the literature, and perhaps more so due to the possibility of directional detections. The most pressing question to answer, in my opinion, is to see what other cosmological and astrophysical constraints exist on these models. It is only in this context that one can reliably assess the relevance of these proposals.

Bibliography

[1] G. Marocco and S. Sarkar, SciPost Phys. **10**, 043 (2021), 2011.08153.

[2] E. Witten, Phys. Lett. B **86**, 283 (1979).

[3] C. D. Froggatt and H. B. Nielsen, Nucl. Phys. B **147**, 277 (1979).

[4] N. Arkani-Hamed and S. Dimopoulos, Phys. Rev. D **65**, 052003 (2002), hep-ph/9811353.

[5] K. R. Dienes, E. Dudas, and T. Gherghetta, Nucl. Phys. B **537**, 47 (1999), hep-ph/9806292.

[6] T. Gherghetta and A. Pomarol, Nucl. Phys. B **586**, 141 (2000), hep-ph/0003129.

[7] Y. Grossman and M. Neubert, Phys. Lett. B **474**, 361 (2000), hep-ph/9912408.

[8] G. 't Hooft, NATO Sci. Ser. B **59**, 135 (1980).

[9] P. A. M. Dirac, Nature **139**, 323 (1937).

[10] C. Abel *et al.*, Phys. Rev. Lett. **124**, 081803 (2020), 2001.11966.

[11] R. J. Crewther, P. Di Vecchia, G. Veneziano, and E. Witten, Phys. Lett. B **88**, 123 (1979), [Erratum: Phys.Lett.B 91, 487 (1980)].

[12] M. Pospelov and A. Ritz, Nucl. Phys. B **573**, 177 (2000), hep-ph/9908508.

[13] G. 't Hooft, Phys. Rev. Lett. **37**, 8 (1976).

[14] S. Aoki *et al.*, Eur. Phys. J. C **77**, 112 (2017), 1607.00299.

[15] R. D. Peccei and H. R. Quinn, Phys. Rev. Lett. **38**, 1440 (1977).

[16] R. D. Peccei and H. R. Quinn, Phys. Rev. D **16**, 1791 (1977).

[17] S. Weinberg, Phys. Rev. Lett. **40**, 223 (1978).

[18] F. Wilczek, Phys. Rev. Lett. **40**, 279 (1978).

[19] M. Dine, W. Fischler, and M. Srednicki, Phys. Lett. B **104**, 199 (1981).

[20] A. R. Zhitnitsky, Sov. J. Nucl. Phys. **31**, 260 (1980).

[21] J. E. Kim, Phys. Rev. Lett. **43**, 103 (1979).

[22] M. A. Shifman, A. I. Vainshtein, and V. I. Zakharov, Nucl. Phys. B **166**, 493 (1980).

[23] A. Arvanitaki, S. Dimopoulos, S. Dubovsky, N. Kaloper, and J. March-Russell, arXiv:0905.4720 [astro-ph, physics:gr-qc, physics:hep-ph, physics:hep-th] (2009), 0905.4720.

[24] P. Svrcek and E. Witten, JHEP **06**, 051 (2006), hep-th/0605206.

[25] V. M. Mehta *et al.*, JCAP **07**, 033 (2021), 2103.06812.

[26] K. A. Beyer, G. Marocco, R. Bingham, and G. Gregori, Phys. Rev. D **105**, 035031 (2022), 2109.14663.

[27] K. A. Beyer, G. Marocco, C. Danson, R. Bingham, and G. Gregori, (2021), 2108.01489.

[28] B. Holdom, Phys. Lett. B **166**, 196 (1986).

[29] F. Reines and C. L. Cowan, Phys. Rev. **92**, 830 (1953).

[30] ALEPH, DELPHI, L3, OPAL, SLD, LEP Electroweak Working Group, SLD Electroweak Group, SLD Heavy Flavour Group, S. Schael *et al.*, Phys. Rept. **427**, 257 (2006), hep-ex/0509008.

[31] B. Pontecorvo, Zh. Eksp. Teor. Fiz. **53**, 1717 (1967).

[32] S. Weinberg, Physical Review Letters **43**, 1566 (1979).

[33] M. Milgrom, ApJ**270**, 365 (1983).

[34] R. H. Sanders and M. A. W. Verheijen, Astrophys. J. **503**, 97 (1998), astro-ph/9802240.

[35] J. D. Bekenstein, Phys. Rev. D **70**, 083509 (2004), astro-ph/0403694, [Erratum: Phys.Rev.D 71, 069901 (2005)].

[36] C. Skordis and T. Zlosnik, Phys. Rev. Lett. **127**, 161302 (2021), 2007.00082.

[37] G. Bertone, D. Hooper, and J. Silk, Phys. Rept. **405**, 279 (2005), hep-ph/0404175.

[38] V. C. Rubin and J. Ford, W. Kent, ApJ**159**, 379 (1970).

[39] T. S. van Albada, J. N. Bahcall, K. Begeman, and R. Sancisi, ApJ**295**, 305 (1985).

[40] Planck, N. Aghanim *et al.*, Astron. Astrophys. **641**, A6 (2020), 1807.06209, [Erratum: Astron.Astrophys. 652, C4 (2021)].

[41] D. Clowe *et al.*, Astrophys. J. Lett. **648**, L109 (2006), astro-ph/0608407.

[42] M. Kuhlen *et al.*, JCAP **02**, 030 (2010), 0912.2358.

[43] M. Fabbrichesi, E. Gabrielli, and G. Lanfranchi, (2020), 2005.01515.

[44] G. Lanfranchi, M. Pospelov, and P. Schuster, (2020), 2011.02157.

[45] A. Prinz *et al.*, Phys. Rev. Lett. **81**, 1175 (1998), hep-ex/9804008.

[46] LSND, L. Auerbach *et al.*, Phys. Rev. D **63**, 112001 (2001), hep-ex/0101039.

[47] MiniBooNE, A. Aguilar-Arevalo *et al.*, Phys. Rev. Lett. **121**, 221801 (2018), 1805.12028.

[48] G. Magill, R. Plestid, M. Pospelov, and Y.-D. Tsai, Physical Review Letters **122**, 071801 (2019).

[49] R. Harnik, Z. Liu, and O. Palamara, JHEP **07**, 170 (2019), 1902.03246.

[50] ArgoNeuT, R. Acciarri *et al.*, Phys. Rev. Lett. **124**, 131801 (2020), 1911.07996.

[51] A. Ball *et al.*, Phys. Rev. D **102**, 032002 (2020), 2005.06518.

[52] OPAL, R. Akers *et al.*, Z. Phys. C **67**, 203 (1995).

[53] S. Davidson, S. Hannestad, and G. Raffelt, JHEP **05**, 003 (2000), hep-ph/0001179.

[54] CMS, S. Chatrchyan *et al.*, Phys. Rev. D **87**, 092008 (2013), 1210.2311.

[55] J. H. Chang, R. Essig, and S. D. McDermott, JHEP **09**, 051 (2018), 1803.00993.

[56] H. Vogel and J. Redondo, JCAP **02**, 029 (2014), 1311.2600.

[57] M. Pospelov and T. ter Veldhuis, Phys. Lett. B **480**, 181 (2000), hep-ph/0003010.

[58] K. Sigurdson, M. Doran, A. Kurylov, R. R. Caldwell, and M. Kamionkowski, Phys. Rev. D **70**, 083501 (2004), astro-ph/0406355, [Erratum: Phys.Rev.D 73, 089903 (2006)].

[59] J. Kopp, L. Michaels, and J. Smirnov, JCAP **04**, 022 (2014), 1401.6457.

[60] A. Ibarra and S. Wild, JCAP **05**, 047 (2015), 1503.03382.

[61] B. J. Kavanagh, P. Panci, and R. Ziegler, JHEP **04**, 089 (2019), 1810.00033.

[62] L3, M. Acciarri *et al.*, Phys. Lett. B **470**, 268 (1999), hep-ex/9910009.

[63] J.-F. Fortin and T. M. Tait, Phys. Rev. D **85**, 063506 (2012), 1103.3289.

[64] X. Chu, J.-L. Kuo, and J. Pradler, Phys. Rev. D **101**, 075035 (2020), 2001.06042.

[65] BEBC WA66, H. Grassler *et al.*, Nucl. Phys. B **273**, 253 (1986).

[66] A. M. Cooper-Sarkar *et al.*, Phys. Lett. B **280**, 153 (1992).

[67] WA66, A. M. Cooper-Sarkar *et al.*, Phys. Lett. B **160**, 212 (1985).

[68] WA66, A. M. Cooper-Sarkar *et al.*, Phys. Lett. B **160**, 207 (1985).

[69] L. Buonocore, C. Frugiuele, and P. deNiverville, Phys. Rev. D **102**, 035006 (2020), 1912.09346.

[70] CHARM-II, K. De Winter *et al.*, Nucl. Instrum. Meth. A **278**, 670 (1989).

[71] CHARM-II, P. Vilain *et al.*, Phys. Lett. B **335**, 246 (1994).

[72] S. Alekhin *et al.*, Rept. Prog. Phys. **79**, 124201 (2016), 1504.04855.

[73] J. Alwall *et al.*, JHEP **07**, 079 (2014), 1405.0301.

[74] L. Buonocore, C. Frugiuele, F. Maltoni, O. Mattelaer, and F. Tramontano, JHEP **05**, 028 (2019), 1812.06771.

[75] T. Sjostrand, S. Mrenna, and P. Z. Skands, JHEP **05**, 026 (2006), hep-ph/0603175.

[76] T. Sjostrand, S. Mrenna, and P. Z. Skands, Comput. Phys. Commun. **178**, 852 (2008), 0710.3820.

[77] P. deNiverville, C.-Y. Chen, M. Pospelov, and A. Ritz, Phys. Rev. D **95**, 035006 (2017), 1609.01770.

[78] T. Fujiwara, T. Kugo, H. Terao, S. Uehara, and K. Yamawaki, Prog. Theor. Phys. **73**, 926 (1985).

[79] H. B. O'Connell, B. Pearce, A. W. Thomas, and A. G. Williams, Prog. Part. Nucl. Phys. **39**, 201 (1997), hep-ph/9501251.

[80] B. Batell, M. Pospelov, and A. Ritz, Phys. Rev. D **80**, 095024 (2009), 0906.5614.

[81] Y. Jho, J. Kim, P. Ko, and S. C. Park, (2020), 2008.12598.

[82] X. Chu, J. Pradler, and L. Semmelrock, Phys. Rev. D **99**, 015040 (2019), 1811.04095.

[83] R. N. Mohapatra and J. W. F. Valle, Phys. Rev. D **34**, 1642 (1986).

[84] I. Cordero-Carrión, M. Hirsch, and A. Vicente, Phys. Rev. D **101**, 075032 (2020), 1912.08858.

[85] J. L. Feng *et al.*, (2022), 2203.05090.

[86] T2K, K. Abe *et al.*, Phys. Rev. D **100**, 052006 (2019), 1902.07598.

[87] G. Bernardi *et al.*, Phys. Lett. B **203**, 332 (1988).

[88] ArgoNeuT, R. Acciarri *et al.*, Phys. Rev. Lett. **127**, 121801 (2021), 2106.13684.

[89] C. O. Dib *et al.*, Phys. Rev. D **101**, 093003 (2020), 1908.09719.

[90] BaBar, B. Aubert *et al.*, Nucl. Instrum. Meth. A **479**, 1 (2002), hep-ex/0105044.

[91] Belle, A. Abashian *et al.*, Nucl. Instrum. Meth. A **479**, 117 (2002).

[92] J. Orloff, A. N. Rozanov, and C. Santoni, Phys. Lett. B **550**, 8 (2002), hep-ph/0208075.

[93] O. Ruchayskiy and A. Ivashko, JHEP **06**, 100 (2012), 1112.3319.

[94] I. Boiarska, A. Boyarsky, O. Mikulenko, and M. Ovchynnikov, Phys. Rev. D **104**, 095019 (2021), 2107.14685.

[95] CHARM, F. Bergsma *et al.*, Phys. Lett. B **166**, 473 (1986).

[96] DELPHI, P. Abreu *et al.*, Z. Phys. C **74**, 57 (1997), [Erratum: Z.Phys.C 75, 580 (1997)].

[97] S. Sarkar, Rept. Prog. Phys. **59**, 1493 (1996), hep-ph/9602260.

[98] N. Sabti, A. Magalich, and A. Filimonova, JCAP **11**, 056 (2020), 2006.07387.

[99] A. Boyarsky, M. Ovchynnikov, O. Ruchayskiy, and V. Syvolap, Phys. Rev. D **104**, 023517 (2021), 2008.00749.

[100] A. M. Cooper-Sarkar *et al.*, Physics Letters B **160**, 207 (1985).

[101] E769, G. A. Alves *et al.*, Phys. Rev. Lett. **77**, 2392 (1996).

[102] DsTau, S. Aoki *et al.*, JHEP **01**, 033 (2020), 1906.03487.

[103] M. Adamovich *et al.*, Nucl. Phys. B Proc. Suppl. **27**, 212 (1992).

[104] Fermilab E653, K. Kodama *et al.*, Phys. Lett. B **263**, 573 (1991).

[105] R. Ammar *et al.*, Phys. Rev. Lett. **61**, 2185 (1988).

[106] S. Frixione, M. L. Mangano, P. Nason, and G. Ridolfi, Nucl. Phys. B **431**, 453 (1994).

[107] R. E. Shrock, Phys. Rev. D **24**, 1232 (1981).

[108] L. Michel, Proc. Phys. Soc. A **63**, 514 (1950).

[109] C. Bouchiat and L. Michel, Phys. Rev. **106**, 170 (1957).

[110] A. B. Arbuzov, Phys. Lett. B **524**, 99 (2002), hep-ph/0110047, [Erratum: Phys.Lett.B 535, 378–378 (2002)].

[111] K. Bondarenko, A. Boyarsky, D. Gorbunov, and O. Ruchayskiy, JHEP **11**, 032 (2018), 1805.08567.

[112] L. M. Johnson, D. W. McKay, and T. Bolton, Phys. Rev. D **56**, 2970 (1997), hep-ph/9703333.

[113] J. A. Formaggio, J. M. Conrad, M. Shaevitz, A. Vaitaitis, and R. Drucker, Phys. Rev. D **57**, 7037 (1998).

[114] F. Deppisch, S. Kulkarni, and W. Liu, Phys. Rev. D **100**, 035005 (2019), 1905.11889.

[115] C. A. Argüelles, N. Foppiani, and M. Hostert, Phys. Rev. D **105**, 095006 (2022), 2109.03831.

[116] WA59, P. Marage *et al.*, Phys. Lett. B **140**, 137 (1984).

[117] S. G. Gorishnii, A. L. Kataev, and S. A. Larin, Phys. Lett. B **259**, 144 (1991).

[118] B. Holdom, Physics Letters B **166**, 196 (1986).

[119] J. Jaeckel and A. Ringwald, Annual Review of Nuclear and Particle Science **60**, 405 (2010), 1002.0329.

[120] E. R. Williams, J. E. Faller, and H. A. Hill, Phys. Rev. Lett. **26**, 721 (1971).

[121] D. F. Bartlett and S. Lögl, Physical Review Letters **61**, 2285 (1988).

[122] D. J. Fixsen *et al.*, The Astrophysical Journal **473**, 576–587 (1996).

[123] A. Caputo, H. Liu, S. Mishra-Sharma, and J. T. Ruderman, Physical Review Letters **125** (2020).

[124] A. A. García, K. Bondarenko, S. Ploeckinger, J. Pradler, and A. Sokolenko, Journal of Cosmology and Astroparticle Physics **2020**, 011–011 (2020).

[125] P. Pani, V. Cardoso, L. Gualtieri, E. Berti, and A. Ishibashi, Phys. Rev. Lett. **109**, 131102 (2012), 1209.0465.

[126] P. Pani, V. Cardoso, L. Gualtieri, E. Berti, and A. Ishibashi, Phys. Rev. D **86**, 104017 (2012), 1209.0773.

[127] A. Caputo, S. J. Witte, D. Blas, and P. Pani, Phys. Rev. D **104**, 043006 (2021), 2102.11280.

[128] A. S. GOLDHABER and M. M. NIETO, Reviews of Modern Physics **43**, 277 (1971).

[129] E. Fischbach, H. Kloor, R. A. Langel, A. T. Y. Liu, and M. Peredo, Phys. Rev. Lett. **73**, 514 (1994).

[130] H. Kloor, E. Fischbach, C. Talmadge, and G. L. Greene, Physical Review D **49**, 2098 (1994).

[131] E. J. Smith *et al.*, Science **183**, 305 (1974), https://science.sciencemag.org/content/183/4122/305.full.pdf.

[132] L. Davis, A. S. Goldhaber, and M. M. Nieto, Physical Review Letters **35**, 1402 (1975).

[133] S. J. Bolton *et al.*, Space Science Reviews **213**, 5 (2017).

[134] D. D. Ryutov, Plasma Physics and Controlled Fusion **49**, B429 (2007).

[135] N. Ness and L. Burlaga, Journal of Geophysical Research **106**, 15803 (2001).

[136] L. F. Burlaga, N. F. Ness, Y. Wang, and N. R. Sheeley, AIP Conference Proceedings **679**, 39 (2003), https://aip.scitation.org/doi/pdf/10.1063/1.1618536.

[137] A. S. Goldhaber and M. M. Nieto, Phys. Rev. Lett. **21**, 567 (1968).

[138] E. Schrödinger, Proceedings of the Royal Irish Academy. Section A: Mathematical and Physical Sciences **49**, 135 (1943).

[139] J. E. P. Connerney, S. Timmins, M. Herceg, and J. L. Joergensen, Journal of Geophysical Research: Space Physics **125**, e2020JA028138 (2020).

[140] E. Smith *et al.*, Journal of Geophysical Research **79**, 3501 (1974).

[141] M. A. Acuna and N. F. Ness, Space Science Instrumentation **1**, 177 (1975).

[142] M. Acuna and N. Ness, Journal of Geophysical Research **81**, 2917 (1976).

[143] J. E. P. Connerney *et al.*, Geophysical Research Letters **45**, 2590 (2018), https://agupubs.onlinelibrary.wiley.com/doi/pdf/10.1002/2018GL077312.

[144] N. F. NESS *et al.*, Science **204**, 982 (1979).

[145] H. S. BRIDGE *et al.*, Science **204**, 987 (1979), https://science.sciencemag.org/content/204/4396/987.full.pdf.

[146] S. M. KRIMIGIS *et al.*, Science **204**, 998 (1979), https://science.sciencemag.org/content/204/4396/998.full.pdf.

[147] J. W. WARWICK *et al.*, Science **204**, 995 (1979), https://science.sciencemag.org/content/204/4396/995.full.pdf.

[148] N. F. NESS *et al.*, Science **206**, 966 (1979), https://science.sciencemag.org/content/206/4421/966.full.pdf.

[149] H. S. BRIDGE *et al.*, Science **206**, 972 (1979), https://science.sciencemag.org/content/206/4421/972.full.pdf.

[150] S. M. KRIMIGIS *et al.*, Science **206**, 977 (1979), https://science.sciencemag.org/content/206/4421/977.full.pdf.

[151] J. B. PEARCE *et al.*, Science **206**, 991 (1979), https://science.sciencemag.org/content/206/4421/991.full.pdf.

[152] J. E. P. Connerney, M. H. Acuña, and N. F. Ness, Journal of Geophysical Research: Space Physics **86**, 8370 (1981).

[153] J. E. P. Connerney *et al.*, Space Science Reviews **213**, 39 (2017).

[154] N. Divine and H. B. Garrett, Journal of Geophysical Research: Space Physics **88**, 6889 (1983).

[155] D. D. Ryutov, Plasma Physics and Controlled Fusion **39**, A73 (1997).

[156] E. N. Parker, The Astrophysical Journal **128**, 664 (1958).

[157] D. Pines, *Elementary excitations in solids* (W.A. Benjamin, 1963).

[158] A. L. Fitzpatrick, W. Haxton, E. Katz, N. Lubbers, and Y. Xu, Journal of Cosmology and Astroparticle Physics **2013**, 004 (2013).

[159] T. Trickle, Z. Zhang, and K. M. Zurek, arXiv:2009.13534 [astro-ph, physics:hep-ph] (2020), 2009.13534.

[160] T. Trickle, Z. Zhang, and K. M. Zurek, Physical Review Letters **124**, 201801 (2020).

[161] Y. Hochberg, Y. Kahn, M. Lisanti, C. G. Tully, and K. M. Zurek, Phys. Lett. B **772**, 239 (2017), 1606.08849.

[162] Y. Hochberg *et al.*, Physical Review Letters **127**, 151802 (2021).

[163] S. Knapen, J. Kozaczuk, and T. Lin, Physical Review D **104**, 015031 (2021).

[164] P. Nozières and D. Pines, Phys. Rev. **113**, 1254 (1959).

[165] I. Zaliznyak and S.-H. Lee, *Magnetic Neutron Scattering* (, 2005), pp. 3–64.

[166] S. Shamoto, M. Sato, J. M. Tranquada, B. J. Sternlieb, and G. Shirane, Phys. Rev. B **48**, 13817 (1993).

[167] A. T. Boothroyd, *Principles of Neutron Scattering from Condensed Matter* (Oxford University Press USA - OSO, Oxford, 2020).

[168] K. Hirakawa, H. Yoshizawa, J. D. Axe, and G. Shirane, Journal of the Physical Society of Japan **52**, 4220 (1983).

[169] Solid State Communications **18**, 433 (1976).

[170] I. Yamada, Journal of the Physical Society of Japan **33**, 979 (1972).

[171] A. Coskuner, A. Mitridate, A. Olivares, and K. M. Zurek, Phys. Rev. D **103**, 016006 (2021), 1909.09170.

[172] C. Blanco, Y. Kahn, B. Lillard, and S. D. McDermott, Physical Review D **104**, 036011 (2021), 2103.08601.

[173] J. Lorenzana, G. Seibold, and R. Coldea, Physical Review B **72**, 224511 (2005).

[174] R. E. Miles, Biometrika **52**, 636 (1965).

[175] S. Lovesey, *Theory of neutron scattering from condensed matter, Vol 2* (OUP, 1984).

[176] D. Lachance-Quirion *et al.*, Science Advances **3**, e1603150 (2017), https://www.science.org/doi/pdf/10.1126/sciadv.1603150.

[177] D. Lachance-Quirion, Y. Tabuchi, A. Gloppe, K. Usami, and Y. Nakamura, Applied Physics Express **12**, 070101 (2019).

[178] D. Alesini *et al.*, Phys. Rev. D **103**, 102004 (2021), 2012.09498.

[179] R. Lasenby and A. Prabhu, (2021), 2110.01587.

[180] T. Holstein and H. Primakoff, Phys. Rev. **58**, 1098 (1940).

[181] FASER, H. Abreu *et al.*, (2020), 2001.03073.

[182] B. Batell *et al.*, Dark Sector Studies with Neutrino Beams, in *2022 Snowmass Summer Study*, 2022, 2207.06898.

[183] DONUT, K. Kodama *et al.*, Phys. Lett. B **504**, 218 (2001), hep-ex/0012035.

[184] OPERA Collaboration, N. Agafonova *et al.*, Phys. Rev. Lett. **115**, 121802 (2015).

[185] N. Fox *et al.*, Space Science Reviews **204**, 7 (2016).

[186] S. Bale *et al.*, Space science reviews **204**, 49 (2016).

[187] A. W. Case *et al.*, The Astrophysical Journal Supplement Series **246**, 43 (2020).